FIRST-PRINCIPLES INFORMED ANALYSIS OF THERMOELECTRIC MATERIALS FOR APPLICATIONS
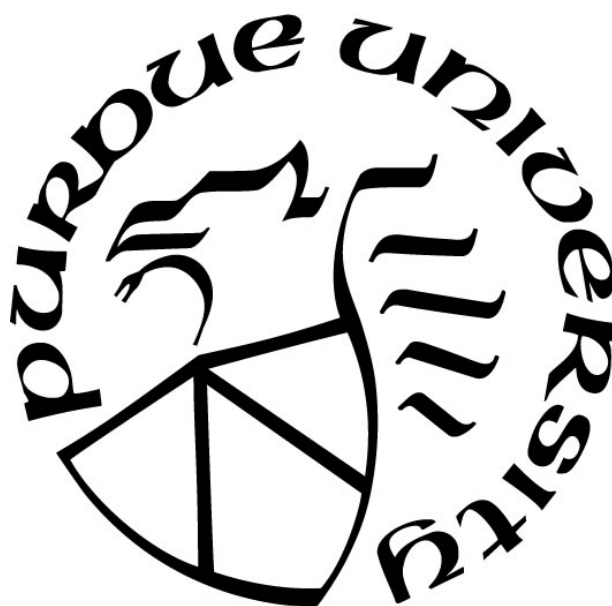
by

Evan Witkoske

A Dissertation

Submitted to the Faculty of Purdue University

In Partial Fulfillment of the Requirements for the degree of

Doctor of Philosophy

School of Electrical and Computer Engineering

West Lafayette, Indiana

December 2019

THE PURDUE UNIVERSITY GRADUATE SCHOOL
STATEMENT OF COMMITTEE APPROVAL

Dr. Mark Lundstrom, Co-Chair

School of Electrical and Computer Engineering

Dr. Na (Luna) Lu, Co-Chair

Schools of Civil and Materials Engineering

Dr. Ali Shakouri

School of Electrical and Computer Engineering

Dr. Supriyo Datta

School of Electrical and Computer Engineering

Dr. Ashraf Alam

School of Electrical and Computer Engineering

Approved by:

Dr. Dimitrios Peroulis

To my parents…

TABLE OF CONTENTS

LIST OF TABLES

LIST OF FIGURES

ABSTRACT

Thermoelectric (TE) devices are useful in niche applications that require reliability and durability, including energy harvesters for sensors, cooling electronics, and power generation at high temperatures. Assessing, optimizing, and implementing materials into practical TE devices and systems have been difficult theoretical and engineering problems. The goal of this research is to develop a first-principles informed approach to analyze thermoelectric materials for potential practical applications.

TE materials and devices are traditionally quantified using a material figure of merit (FOM), zT, and device FOM, ZT. Using full numerical descriptions of band structures and solutions to the Boltzmann transport equation (BTE) in the relaxation time approximation (RTA), we examine how band convergence may or may not increase zT depending on the relative strength of intra- and inter-band scattering. We compute zT vs. a generalized TE quality factor (b-factor) and examine a dozen complex TE materials showing none exceeds the performance of a simple, parabolic energy band. In fact, a plot of zT vs. b-factor appears to be universal. We test this conclusion based on RTA solutions to the BTE using a simple treatment of scattering against more rigorous first-principles approaches.

In addition, we theoretically assess a low-cost TE oxide ($2H\text{-}CuAlO_2$), which has durability at high temperatures and is earth abundant, making it attractive for applications. Finally, with an eye towards minimizing the \$cost/kW-hr of thermoelectric energy generation, we discuss our approach to a few specific high temperature environments and discuss their viability as practical system level applications.

1   INTRODUCTION

1.1 Motivation

Thermoelectric (TE) devices are solid-state devices with applications in energy generation and cooling, however to date, as robust and reliable as these devices are, they have been limited by low conversion efficiencies [1]–[5]. The past three decades have witnessed the thermoelectric material figure of merit, zT, being raised from under a value of one to over two [5]. These gains have been primarily driven by a reduction in the lattice thermal conductivity of materials through the use of nano-structuring [6]–[12], and novel materials that have an inherently low thermal conductivity due to large discrepancies in the masses of their constituent elements or also so called "rattler" materials. These advances, however, have not translated into working devices [13], due to a variety of practical issues that include but are not limited to; electrical contacts, doping feasibility, maintaining thermal gradients, material quality, packaging of the device, thermal contacts, and material costs just to name a few. As we approach the lower limit of the lattice thermal conductivity for common and even complex TE materials at room temperature and above, the variety of avenues forward for the field of thermoelectrics is being narrowed.

Despite recent advances in TE materials research, there have been limited, if any, demonstrations of materials or devices with figure of merit values greater than one for commercial use. The best opportunity for TE materials lies in specific niche applications by co-development of new devices and systems. In this work, we theoretically assess the TE potential of a low-cost metal oxide (2H-CuAlO$_2$), which has durability at high temperatures and is earth abundant, making it attractive for applications. Finally, with an eye towards minimizing the $cost/kW-hr of thermoelectric energy generation, we discuss our approach to a few specific high temperature environments and discuss their viability as practical system level applications.

1.2 Status of Thermoelectrics

Because of their low conversion efficiency of at best around ~10% for TE devices, thermoelectrics have not found wide spread applications. In instances where the reliability rather than the cost is a major consideration, such as in NASA spacecraft [14], or applications where the overall power generation needed is small, such as using waste heat to power low power

sensors and wireless electronics [15], thermoelectrics have found somewhat of a home. The development of new thermoelectric materials with high efficiency is paramount to expanding the use of TEs beyond certain niche applications. Progress in thermoelectrics had all but halted until new ideas for nano-structuring of materials to lower the lattice thermal conductivity were introduced in the 1990's, the effect of which can be seen in Figure 1.1 [13], [16] .
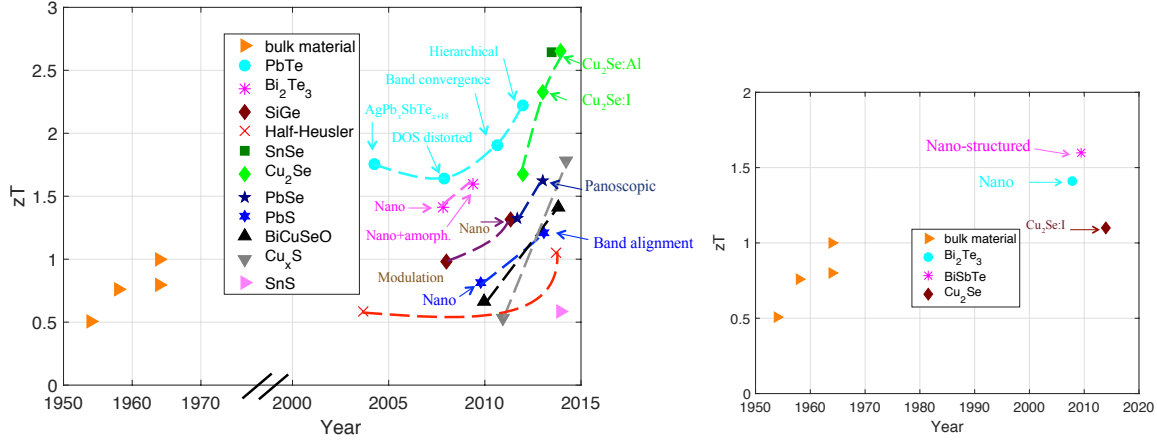
Figure 1.1. (a)General overview of the efficiency of thermoelectric materials and structures over time. (b) zT versus time for best near room temperature thermoelectric materials.

With the use of nano-structuring, substantial progress in increasing an important efficiency figure of merit, zT, has been achieved [10], [17], [18], however many of the data points in figure 1.1 have been viewed with considerable skepticism for a variety of reasons. zT values of above 1.5 have been demonstrated with some degree of reproducibility, however there have been questions about some of the recently reported results above a zT of 2 [19]. Much of this can be attributed to the difficulty in achieving accurate experimental thermal and electrical characterization techniques, with many papers skirting some of the unresolved issues. SnSe has been a popular and successful material in reaching high zT values, however even with its success, some of the data points are still in question. Some of the recently introduced cuprate materials have achieved "high" zTs in both high and low temperature ranges with some degree of reproducibility, but measurement and the theoretical conclusions from these high measurement values remains an issue. Current trends in thermoelectrics are directed more towards room temperature applications, however as can be seen in Fig 1.1(b), little progress has been made in increasing the device zT above a value of one. The materials that have gained recent interest in the room temperature range continue to be Bismuth based materials utilizing

13

nanostructuring with a variety of doping elements and methodologies, with novel materials different from Bi/Sb/Te in this temperature range remaining elusive.

The approach of increasing zT by nano-structuring is reaching its limits over the last 20-30 years, and still higher zT's are needed to expand the use of thermoelectrics to a more prominent role in mainstream applications. The focus is now shifting from reducing the lattice thermal conductivity to the exploration of ways to improve the electronic and device performance of thermoelectric systems. Many ideas to improve the electronic performance have been introduced over the past 60 years, but there has been little progress. The number of papers on this topic continues to increase, but progress has been elusive. A large amount of effort has been made into researching and developing novel materials with high efficiency and subsequently high zT values at a variety of temperatures [6], [7], [20]–[26]. However, the translation of high efficiency materials into working devices has been elusive. If material gains cannot be translated into actual devices, much of the research into high zT materials will be for naught.

1.2.1 Devices and Applications

Thermoelectric materials and devices can be used as both solid-state coolers and electric power generators. As shown in Fig. 1.2, these devices consist of n and p type semiconductors (with a two "legs" shown in fig. 1.2a as one unit) with multiple units that are electrically connected in series to form typical TE modules in fig 1.2b. With this setup, the device is thermally connected in parallel. By applying a current to the device, the top contact (or bottom contact depending on the direction of current applied) cools below the ambient temperature of the device. Conversely by applying heat on one side and a heat sink to the other contact, electric power is generated. Even with relatively low conversion efficiencies of ~10% for TE devices when used as electric power generators, these devices do offer advantages for some applications. They have no moving parts, are reliable and robust at a variety of temperatures (depending on the material), and have long operating life times. To design devices for optimum efficiency and space requirements, a TE leg length, and a Fill Factor (FF) (i.e. the ratio of the module surface area to the total surface) are generally used to take into account electrical and thermal properties and device geometries of both the n and p legs to design the device, with performance and cost optimization as manufacturing constraints [3], [27]–[32] being considerations as well.

$\Delta T = 100 \text{ K}$

Ground

$I_{SC} \approx 5 \ \mu\text{A}$

$V_{OC} \approx 3.3 \text{ V}$

$P \approx 6 \ \mu\text{W}/cm^2$

a)

TE cooler

T_C

cool

I_Q — N-type — P-type — I_Q

$I \rightarrow$ — $I \rightarrow$

hot — hot

T_H

TE generator

T_H

hot

I — N-type — P-type — I

cool (ambient)

I — T_C — I

b)
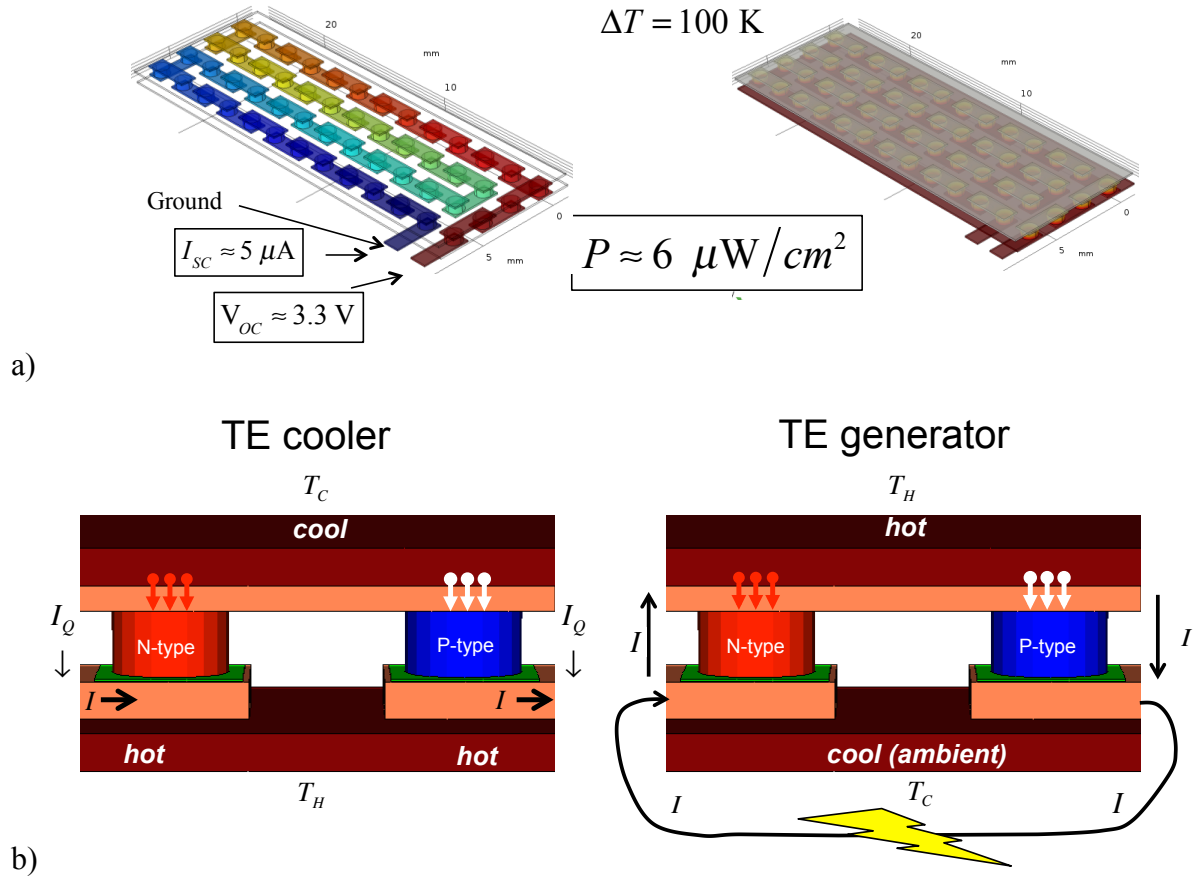
Figure 1.2. Fig. 1.2a is the general layout of a thermoelectric cooler and generator designed in Sentaurus. Fig. 1.2b on the left is a TEG module design done in Comsol with a 100 K temperature difference. The left graphic shows the V_{OC} distribution in color, while the graphic on the bottom right shows the same module with colors representing temperature distribution.

Figure 1.2a is general schematic for TE modules in *Synopsys® Sentaurus Device* with module level device performance simulated using packages such as *Comsol Multiphysics®* [33] in Fig. 1.2b. An interesting byproduct of these simulations is that simple, back of the envelope calculations can be relatively accurate estimations of the overall power output of a TEG (especially when considering an "infinite" heat sink and heat source temperatures). For example, using basic TE equations with simplified and reasonable input material parameters for the above structures one can estimate an overall power density of $6 \ \mu\text{W}/\text{cm}^2$, while the value from simulation is found to be $10 \ \mu\text{W}/\text{cm}^2$. However, the reality of the tightly coupled material parameters, shown next in section 1.3, in tandem with device considerations (i.e. fill factor, operating temperature, temperature differences, etc) makes maximizing the efficiency and cost a difficult challenge indeed.

1.3 Thermoelectric Basics

1.3.1 Thermoelectricity

In 1820, Thomas Johann Seebeck was the first to recognize the thermoelectric effect using a loop of two different metals with the two junctions being kept at different temperatures [34]. When he brought a compass close to the loop, the needle would deflect depending on the orientation and direction of the loop and compass. Seebeck incorrectly deduced that temperature differences produced a constant magnetic field [35] within the loop, when in reality, the temperature difference generated a current, with the current producing a voltage in the loop, the effect appropriately named the "Seebeck effect". The current in the loop produced the magnetic field that Seebeck detected. Just as in a gas or liquid, when a temperature gradient is maintained between the ends or junctions of a material, the carriers on the hot side will want to diffuse to the cold side.   When two different materials are used, or a single material is in open circuit conditions, a Seebeck voltage will be produced [19]. The ratio of the open-circuit voltage to the applied temperature gradient is called the Seebeck coefficient (S),

$$\Delta V_{oc} = -S\Delta T \ .$$

(1.1)

The negative sign in front of the Seebeck coefficient produces a positive voltage on the higher temperature side when the carriers are negatively charged, as in the case for electrons, whereas for positive holes, the Seebeck coefficient is positive, and the overall voltage is negative.

In 1834 the "dual" effect was discovered when Jean Charles Athanase Peltier found a temperature difference was created when a current was forced through two different metals. The heat carried by an electron or hole was emitted or absorbed at the junction due to the difference in energy levels of carriers for the two different metals [36]. When the current direction was reversed, the junction went from either heating to cooling, or vice versa. This rate of cooling or heating is directly proportional to the current flowing through the junction, which is given by,

$$Q = \left(\pi_A - \pi_B\right)I = I\Delta\pi \ .$$

(1.2)

The difference in the Peltier coefficients, defined as ($\Delta\pi$), can be thought of as the difference in the amount of energy carried per unit charge for two particular materials.

In 1851 William Thomson found what is referred to as the Thomson effect [37]. Sometimes considered a separate effect, in fact this effect is simply due to the temperature dependence of the Seebeck coefficient. Thomson showed that the ratio of the Peltier and Seebeck coefficients is equal to the temperature as,

$$\pi = TS .$$ (1.3)

There are additional effects to those described above that take place within a thermoelectric material or device that can be important as well. Two of these are Joule heating and heat conduction, which can be described by Fourier's law [37] and is due to heat being carried by phonons diffusing from the hot to cold side. Fourier's law relates the heat current density $\vec{q}$ to the temperature gradient by the thermal conductivity κ as,

$$\vec{q} = -\kappa \vec{\nabla} T .$$ (1.4)

By forcing a current $J_x = \dfrac{1}{A} I_x$, with J_x being the current density, through a thermoelectric material with a temperature gradient, a voltage difference can be produced which can be related to the electric field as,

$$J_x = \sigma E_x - \sigma S \nabla T .$$ (1.5)

The total amount of heat that is transported through a material is carried by, electrons, holes, and phonons and is called the heat current density. By combing the above equations eqns. (1.3-1.6) with the total thermal conductivity, κ, given by the sum of the lattice thermal conductivity, κ_L, and the electronic thermal conductivity κ_e, yields the total heat current density,

$$q_x = \pi J_x - \left(\kappa_L + \kappa_e\right) \nabla T = \pi J_x - \kappa \nabla T .$$ (1.6)

Eqn. (1.6) can be used to show the correspondence between how the application of a temperature gradient can produce a voltage difference through the Seebeck effect, or how an applied current can produce a temperature gradient through the Peltier effect. Due to the Onsager reciprocity [38], all the above thermoelectric equations are reversible. However, once Joule heating is

included, the symmetry of the thermoelectric equations is broken, and the overall heat transported is no longer conserved in the above equations.

1.3.2   *zT* and Power Factor (PF)

We will see next how these parameters intertwine when trying to optimize the efficiency and overall power generation or cooling capability of a thermoelectric material or device. Since each of these electronic parameters is inexorably linked, trying to optimize one will lead to a reduction or increase in another. A further difficulty involves the lattice thermal conductivity κ_L of a material, normally assumed to be independent of the electrical parameters, can in fact be dependent on the same quantities as the electronic components as well. This makes sorting out the best strategy for optimizing a material or device challenging. We now look to quantify an actual thermoelectric device's performance, focusing on optimizing the efficiency for a thermoelectric generator (TEG) of a single material (i.e. only n or p type), with similar results extending to a thermoelectric cooler, albeit with a different form of the same general result [35]. In a TEG the amount of heat flowing into and out of a device using equations (1.1-1.6) can be written as (including Joule heating),

$$
q_{in} = ST_1 I + \kappa\left(T_1 - T_2\right) - \frac{1}{2}RI^2
$$
$$
q_{out} = ST_2 I + \kappa\left(T_1 - T_2\right) + \frac{1}{2}RI^2
$$
$$
\text{(1.7)}
$$

with T_1 and T_2 being the temperatures of the two contacts, and R the resistance of the material in between.

The overall electrical power generated can be written as,

$$
P_{gen,el} = q_{in} - q_{out} = SI\left(T_1 - T_2\right) - RI^2 .
$$
$$
\text{(1.8)}
$$

For a TEG to power a load, a load resistance must be including in the analysis, with basic voltage division giving the output power as,

$$P_{gen} = \frac{\Delta V_{oc}^2}{R} \frac{R_{load}/R}{\left(R_{load}/R + 1\right)^2}, \tag{1.9}$$

with the open circuit voltage given by (1.1). The overall efficiency of the device is now given by,

$$\eta = \frac{P_{gen}}{q_{in}} = \frac{\Delta T}{T_1} \frac{M}{\left(M + 1 + \frac{(M+1)^2}{(S^2/R\kappa)T_1} - \frac{1}{2}\frac{\Delta T}{T_1}\right)}. \tag{1.10}$$

with $M = R_{load}/R$ being the load ratio and $T_1 - T_2 = \Delta T$, and S coming from eq. (1.1). We now optimize these equations in two ways; first we maximize the efficiency, eq. 1.10, with respect to the load ratio M, and secondly we optimize eq. (1.8) with respect to current. These correspond to 1) maximizing the efficiency of a material given a particular heat flux, and 2) optimizing the total output current.

Solving eqn. (1.10) for the maximum efficiency gives a load ratio of $M = R_{load}/R = \sqrt{1 + z(T_1 + T_2)/2} = \sqrt{1 + zT}$. The performance of a TE device is related to a "material" figure of merit, zT, which can be written as [1], [2], [39], [40],

$$zT = \frac{S^2 T}{R(\kappa)} = \frac{S^2 T}{R(\kappa_e + \kappa_L)} = \frac{S^2 \sigma T}{(\kappa_e + \kappa_L)}, \tag{1.11}$$

where S, σ, κ_e, and κ_L are the Seebeck coefficient, electrical conductivity, electronic thermal conductivity, the lattice thermal conductivity, and T the absolute or average temperature. This equation can be derived in a similar fashion from the definitions of the Onsager reciprocity relations in open circuit and closed circuit conditions for heat transport [35]. However, the concept is simple, and relates to our further studies in chapters 2 and 3 regarding what we will define later as the "b-factor". We see from (1.10) that maximizing efficiency is tantamount to maximizing zT, hence why most TE materials research is focused on maximizing zT. We can understand this from eq. 1.11, for the most efficient n-type TEG we want all of the heat to be carried by electrons, but with each electron carrying a small amount of heat.

However, when we optimize eq. (1.8) for current we find the usual result from circuit theory that $M = R_{load}/R = 1$. This gives a maximum power generated equal to $P_{gen}^{MAX} = \dfrac{S^2 \Delta T^2}{4R}$. This quantity is closely related to the power factor (PF) defined as,

$$PF = \frac{S^2}{R} = S^2\sigma .$$ (1.12)

Therefore, to maximize the power generated (P_{gen}), the power factor should be maximized [41]. This can be explained physically as follows; for a given heat flux, the most efficient device design is one with the highest zT. However, when a device can sustain a large temperature gradient and the device design is fixed, more heat flux yields more electrical power out, i.e. the PF should be optimized. Therefore, when an "infinite" heat sink and heat source are available, only the power factor (PF) matters for how much total power can be produced.

1.3.3   Landauer approach to Thermoelectrics

In this section, we will briefly outline the Landauer approach to thermoelectric transport theory [42], [43]. This approach can be applied to electrons, holes, phonons, or energy transport in general from the ballistic to diffusive limits, and can be shown to be equivalent to Boltzmann transport theory in semi-classical transport and can be related to the non-equilibrium Greens function (NEGF) concept in the quantum regime [43]. The contacts each have an energy given by the Fermi function,

$$f_0\left(E - E_F\right) = \frac{1}{1 + e^{\frac{E - E_F}{k_B T}}} ,$$ (1.13)

with T being temperature, k_B Boltzmann's constant, and E_F is the Fermi level. The electrons in each contact quickly thermalize so that each contact stays very close to equilibrium. The contacts are considered to be perfect, without any back-reflection from carrier or boundary scattering. To understand the basics of transport in the Landauer form, consider eqn. (1.14) below that describes the current through a material with two contacts just described,

$$I = \frac{2q}{h} \int \bar{T}(E) M(E) (f_1 - f_2) dE , \tag{1.14}$$

where the symbol $\bar{T}(E)$ is the transmission, $M(E)$ is the distribution of modes, and $f_1 - f_2$ is the difference in the Fermi function for contact 1 and contact 2. The transmission is a number from 0 to 1 that describes the probability that an electron entering the material or device from one contact leaves through the other. See [42] for a more detailed discussion about transmission from the diffusive to ballistic limits. Since the Fermi function describes the occupation probability of electrons, a positive difference between $f_1 - f_2$ provides a net positive probability for electrons to move from one contact to the other. When the difference in Fermi functions is due to a small applied voltage with the temperature remaining constant, $f_1 - f_2$ can be approximated as,

$$f_1 - f_2 \approx -\frac{\partial f_0}{\partial E} qV . \tag{1.15}$$

For our purposes in thermoelectrics we are also concerned with temperature differences, thus $f_1 - f_2$ for small temperature differences can be written as,

$$f_1 - f_2 \approx \left(\frac{\partial f_0}{\partial E} \right) \frac{E - E_F}{T} \Delta T . \tag{1.16}$$

In both approximations the "Fermi window" $\left(\frac{\partial f_0}{\partial E} \right)$ replaces $f_1 - f_2$. The Fermi window acts as a weighting function, allowing only carriers within a small range of energies to contribute to current flow.

The distribution of modes $M(E)$ is given by,

$$M(E) = \frac{h}{4} \langle v_x^+(E) \rangle D(E) \tag{1.17}$$

with *D(E)* the density of states and $\left\langle v_x^+(E) \right\rangle$ is the average forward directed velocity in the x-direction. All that is needed to describe the distribution of modes is the electronic dispersion or *E(k)* diagram for the device or material in question. This quantity as we will see later is of paramount importance when trying to understand the parameters that dictate what makes a good thermoelectric, especially when the scattering in a material can be described by a constant mean free path. As described in [43], the distribution of modes can be thought of as a distribution of lanes on a highway, with a velocity and location in energy space. The more modes or "lanes" there are around the Fermi window, the more carriers can travel through them.

Using the Landauer formalism as discussed, the thermoelectric transport parameters can be written compactly using a simple definition of "energy moments" given by the integral *H* with moment or order *j* [44],

$$H_j = \int \left(\frac{E - E_F}{kT} \right)^j \overline{T}(E) M(E) \left(-\frac{\partial f_0}{\partial E} \right) dE \, . \tag{1.18}$$

We can now understand the basic thermoelectric elements as combinations of the zeroth order (conductance (*G*)), first order (Seebeck coefficient (*S*)), and variance (electronic thermal conductivity (κ_e)). The conductivity is,

$$\sigma = \int_{-\infty}^{+\infty} \sigma'(E) dE = \frac{2q^2}{h} H_0 \, , \tag{1.19}$$

$$\text{with } \sigma'(E) = \frac{2q^2}{h} T(E) M(E) \left(-\frac{\partial f_0}{\partial E} \right). \tag{1.20}$$

The differential conductivity can be written as,

$$\sigma'(E) = q^2 \Xi(E) \left(-\frac{\partial f_0}{\partial E} \right), \tag{1.21}$$

with $\Xi(E)$ the well known parameter, termed the transport distribution [30].

The Seebeck coefficient and electrical thermal conductivity are,

$$S = -\frac{k}{q}\frac{H_1}{H_0},$$

(1.22)

and

$$\kappa_e = \frac{2k^2 T}{h}\left(H_2 - \frac{H_1^2}{H_0}\right),$$

(1.23)

respectively. Eqns. (1.19, and 1.22-1.23) are identical to the quantities given in section 1.2. Using these equations in the open source tool, LanTrap 2.0 [32] with an assumption for scattering contained in the transmission function, with input from a DFT-generated electronic band structure, all the relevant quantities can be computed directly.

1.4 Thesis Objectives and Outline

The focus of this work is on examining the thermoelectric potential of transparent conducting oxides (TCOs). We specifically focus on p-type and n-type 2H-CuAlO$_2$. A few studies have examined the effect of strain, chemical composition, and doping concentration on this material's band structures [45]–[47], but the actual effects on TE parameters such as PF and lattice thermal conductivity hasn't, to our knowledge, been addressed. TCOs' high Seebeck coefficient (for large band gaps), high thermal stability, and earth abundance make them suitable for thermoelectric power generation, particularly in high-temperature regimes with the potential for low costs [48]–[51].

In this work I will deploy first principles informed analyses using Quantum Espresso [52] to generate electron and phonon band structures from the DFT (density functional theory). These outputs will be coupled with the open source tools LanTrap 2.0 [53] and the D3Q-Thermal2 package interfaced to QE [54], [55], to compute TE transport properties, as well as compact models using simple parabolic bands designed in Matlab for TE optimization. The thesis is organized as follows:

Chapters 2 and 3 set the stage by addressing the question: What makes a good thermoelectric material from an electronic perspective?

- In Chapter 2, we study complex electronic band structures, with multiple valleys or bands at the same or similar energies. In this chapter, we demonstrate how first-principles band structures coupled with recently developed techniques for rigorous simulation of electron-phonon scattering provide the capabilities to realistically assess the benefits and trade-offs associated with these multi-band materials; in contrast to common wisdom in TEs, we show that multiple bands or valleys have a small effect on zT.

- In Chapter 3, we use full, numerical band structures and solve the Boltzmann equation in the relaxation time approximation using energy-dependent scattering times informed by first principles simulations to compute the thermoelectric figure of merit, zT vs. a generalized thermoelectric quality factor. A key finding was that no matter how complex the band structure, all TE materials examined display a universal behavior, i.e. they all have an optimum zT vs. generalized quality factor that is identical to that of a parabolic band.

Having set the stage, chapters 4 and 5 examine the thermoelectric potential of 2H-CuAlO$_2$.

- In Chapter 4, using first principles calculations, the use of strain to adjust electronic transport and the resultant thermoelectric (TE) properties of 2H phase CuAlO$_2$ is discussed. The results are explained in the terms of the thermoelectric transport distribution and the Landauer distribution of modes. The two key findings were that under certain strain conditions, both p and n type transport can be realized, and secondly, that when a constant mean-free-path is assumed, the distribution of modes dictates the performance of the material.

- In Chapter 5, using first principles calculations, the use of strain and grain boundaries to adjust the phonon transport properties and the resultant lattice thermal conductivity of 2H-CuAlO$_2$ is discussed. The average crystalline lattice thermal conductivity is found to be around 32 W/(K-m) at room temperature and falls to between 5-15 W/(K-m) for typical experimental grain sizes from 3nm to 30nm at room temperature. A second observation of this study shows that when grains of 3nm or less are assumed,

the thermal conductivity is generally independent of temperature for unstrained, compressive, or expansive strained structures. A positive +3% hydrostatic strain in crystalline 2H-CuAlO$_2$ has a similar reduction of thermal conductivity compared to a sample with 3nm grain boundaries. However, due to uncertainties in the fabrication process, grain boundaries appear to be the best method to reduce the lattice thermal conductivity in this material.

- In Chapter 6, we summarize the thesis and provide suggestions for applications of the current work and discuss the potential of future work in this area.

1.5 List of Associated Publications

- **E. Witkoske**, X. Wang, M. Lundstrom, V. Askarpour, and J. Maassen, "Thermoelectric band engineering: The role of carrier scattering," *J. Appl. Phys.*, vol. 122, no. 175102, 2017.

- **E. Witkoske**, X. Wang, J. Maassen, and M. Lundstrom, "Universal behavior of the thermoelectric figure of merit, zT vs. quality factor," *Mater. Today Phys.*, vol. 8, pp. 43–48, 2019.

- **E. Witkoske**, D. Guzman, Y. Feng, A. Strachan, M. Lundstrom, and N. Lu, "The use of strain to tailor electronic thermoelectric transport properties : A first principles study of 2H-phase CuAlO2," *J. Appl. Phys.*, vol. 125, no. 082531, 2019.

- **E. Witkoske**, Z. Tong, Y. Feng, X. Ruan, M. Lundstrom, and N. Lu, "The use of strain and grain boundaries to tailor phonon transport properties: A first principles study of 2H-phase CuAlO$_2$ (Part II)," (to be submitted (JAP)).

- X. Wang, **E. Witkoske**, J. Maassen, and M. Lundstrom, "LanTraP: A code for calculating thermoelectric transport properties with Landauer formalism," *arxiv: 1806.08888v1*, 2018.

- Y. Feng, **E. Witkoske**, E. S. Bell, Y. Wang, A. Tzempelikos, I. Ferguson, and Na Lu, "Advanced Metal Oxides and Nitrides Thermoelectric Materials for Energy Harvesting," *Engineering Science (ES) Materials Manufacturing*, vol. 1, pp. 13–20, 2018.

- E. Ghafari, **E. Witkoske**, Y. Liu, C. Zhang, X. Jiang, A. Bukowski, B. Kucukgok, I. Ferguson, N. Lu, "Chapter 2: Waste Heat Harvesting using III-Nitride Materials", *in* III-

Nitrides Materials, Devices, and Nano-structures, ed. ZC. Feng, World Scientific Publishing, ISBN: 978-1-78634-318-5, pp. 37-75, 2017.

- **E. Witkoske**, X. Wang, J. Maassen, and M. Lundstrom, "A Quality Factor limit to zT," in International Conference on Thermoelectrics (ICT), Caen France, Summer-P.54, 2018.

- **E. Witkoske**, Y. Feng, X. Wang, M. Lundstrom, and Na Lu, "Maximizing zT of 2H phase p-type $CuAlO_2$ through doping optimization: An integrated Experimental and Theoretical Approach," in MRS Spring Meeting-2018.

2   ON THE USE OF BAND CONVERGENCE TO IMPROVE THERMOELECTRIC PERFORMANCE

2.1 Preface

The contents of this chapter have been extracted from the following publications with permission: E. Witkoske, X. Wang, M. Lundstrom, V. Askarpour, and J. Maassen, "Thermoelectric band engineering: The role of carrier scattering," *J. Appl. Phys.*, vol. 122, no. 175102, 2017.

2.2 Introduction

The performance of a thermoelectric device is controlled by the material figure of merit [1], [2], [39], [40],

$$zT = \frac{S^2 \sigma T}{\kappa_e + \kappa_L},$$

(2.1)

where S is the Seebeck coefficient, σ the electrical conductivity, T the absolute temperature, κ_e the electronic thermal conductivity, and κ_L the lattice thermal conductivity. How various material parameters affect zT is well understood (e.g. [1], [2], [39], [40],), but parabolic energy band analyses suggest that the prospects for improving the electronic contribution to zT are limited [56]. Indeed, much of the recent progress in increasing zT has been achieved by lowering the lattice thermal conductivity (e.g. [4], [11], [12], [57]–[59]). There is, however, currently considerable interest in examining complex thermoelectric materials, which may provide improved electrical performance not possible with simple parabolic energy bands (e.g. [56], [57], [60]–[65]). First-principles calculations of thermoelectric transport parameters are routinely performed to assess complex thermoelectric materials [66], [67], but the treatment of electron scattering greatly complicates the analysis leading to the widespread use of rigorous band structures coupled with a highly simplified treatment of scattering – the constant relaxation time approximation (CRTA). The recent development of techniques to rigorously compute scattering rates [68]–[72] presents an opportunity to include detailed band structure and scattering physics in the analysis of complex thermoelectric materials. Our goal is to illustrate

the importance of going beyond the CRTA by presenting calculations for n-type silicon, which has an anisotropic, multi-valley conduction band, as a model material.

Equation (2.1) can be re-expressed as

$$zT = \frac{S'^2}{L' + 1/b} \ ,$$
(2.2)

where $S' = S/(k_B/q)$ is the dimensionless Seebeck coefficient, $L' = L/(k_B/q)^2$ the dimensionless Lorenz number, and

$$b \equiv \frac{\sigma T}{\kappa_L (k_B/q)^2} \ .$$
(2.3)

Assuming unipolar conduction, the conductivity can be written as $\sigma = nq\mu_n$, where n is the carrier density and μ_n the mobility. If we further assume parabolic energy bands, then we can write

$$b = B\mathcal{F}_{1/2}(\eta_F)$$
(2.4)

where

$$B \equiv \frac{N_V}{4} \left(\frac{2m_V^* k_B T}{\pi \hbar^2} \right)^{3/2} \frac{q\mu_n T}{\kappa_L} \left(\frac{k_B}{q} \right)^2 .$$
(2.5)

In (2.5)

$$\eta_F = (E_F - E_C)/k_B T \ ,$$
(2.6)

is the dimensionless Fermi energy (chemical potential), $\mathcal{F}_{1/2}(\eta_F)$ is the Fermi-Dirac integral of order $j = 1/2$ as written in the Blakemore form [73]

$$\mathcal{F}_j\left(\eta_F\right) = \frac{1}{\Gamma(j+1)} \int_0^\infty \frac{\eta^j d\eta}{1+e^{\eta-\eta_F}} \quad , \tag{2.7}$$

and m_v^* is the DOS effective mass of a single valley, and N_V is the valley degeneracy. Note that the b-factor in (2.3) can be evaluated for any band structure while the B-factor in (2.5) assumes parabolic energy bands.

The quantity, B, is the "material factor" β introduced by Chasmar and Stratton [74]. It was discussed extensively by Mahan, who called it the "B-factor" [40]. The important role it plays in thermoelectric material design has been recently discussed by Wang et al. [61], who call B the quality factor. The B-factor is, however, not the whole story. For example, recent work has focused on identifying complex thermoelectric materials with increased Seebeck coefficient (e.g. [60]) or reduced Lorenz number (e.g. [75]). While there are many trade-offs involved in thermoelectric material design, our focus in this chapter is on how multiple valleys affect the b-factor. We do so using rigorous treatments of band structure and electron-phonon scattering.

Equation (2.5) suggests that materials with many degenerate valleys will be good thermoelectrics. Mahan points out that good thermoelectric materials are all multi-valley semiconductors [40] (but n-GaAs, a single valley material, also shows promise [76].) Recent work on thermoelectric band engineering has focused on engineering materials to achieve a large number of valleys and/or bands near the Fermi level (e.g. [62], [63]). As written, however, (2.5) does not highlight the trade-off involved in increasing the valley/band degeneracy. More valleys and bands provide more states to which carriers can scatter. Increasing N_V should decrease the scattering time and lower the mobility. These considerations have been discussed by Wang et al. [61], who argue that intra-valley scattering typically tends to dominate, so increasing N_V should increase B. A recent study using analytical descriptions of energy bands and scattering processes concluded that multiple valleys may or may not be beneficial depending on the material-dependent specifics of inter-valley scattering [77]. First-principles calculations of thermoelectric transport parameters allow complex band structures to be treated without approximation, but since they commonly make the constant relaxation time approximation, such simulations cannot answer how much increasing the number of valleys improves the b-factor. Rigorous calculations

of electron-phonon scattering rates are, however, now possible. In this chapter, we show that the capabilities now exist to more thoroughly address the question of how multiple valleys affect thermoelectric performance.

This chapter is organized as follows. The equations for the thermoelectric transport coefficients are summarized in Sec. 2.3; the goal of the chapter is to solve these equations and assess the impact of intervalley scattering on the b-factor as given by (2.3). In Sec. 2.4, we solve the thermoelectric equations for parabolic band semiconductors and use the solutions to illustrate issues that are examined with a full numerical band structure and first principles scattering rates in Sec. 2.5. To illustrate the rigorous treatment of an anisotropic, multi-valley semiconductor, we consider n-type Si, which has six conduction band valleys. We use a DFT-generated band structure along with electron-phonon scattering rates informed by rigorous simulations to compare six-valley silicon to corresponding single spherical band structures. The results will show that for Si the benefits of the six multiple valleys are largely offset by intervalley scattering, but the anisotropic band structure does provide benefits over a simple, isotropic band structure. To understand the results presented in Sec. 2.5, we must separate the effects of intra- and inter-valley scattering from those due to the anisotropy of the band structure. In Sec. 2.6, we examine two simple metrics that can be used to assess the thermoelectric potential of complex band structures. The chapter concludes with a Summary in Sec. 2.7.

2.3 Approach

The expressions for the thermoelectric transport coefficients that result from a relaxation time approximation solution to the Boltzmann Transport Equation (BTE) are:

$$\sigma = \int_{-\infty}^{+\infty} \sigma'(E) dE \tag{2.8a}$$

$$S = -\frac{1}{qT} \frac{\int_{-\infty}^{+\infty} (E - E_F) \sigma'(E) dE}{\int_{-\infty}^{+\infty} \sigma'(E) dE} \tag{2.8b}$$

$$\kappa_0 = \frac{1}{q^2 T} \int\limits_{-\infty}^{+\infty} \left(E - E_F\right)^2 \sigma'\left(E\right) dE \tag{2.8c}$$

$$\kappa_e = \kappa_0 - T\sigma S^2, \tag{2.8d}$$

where the differential conductivity is

$$\sigma'\left(E\right) = q^2 \Xi\left(E\right)\left(-\frac{\partial f_0}{\partial E}\right), \tag{2.8e}$$

and the transport distribution is [78]

$$\Xi_{ij}\left(E\right) \equiv \frac{1}{\Omega} \sum_{\vec{k}} \left(v_i \tau_{jk} v_j\right) \delta\left(E - E_k\right), \tag{2.8f}$$

where Ω is a normalization volume. Equations (8) are identical to eqns. (1.13-1.15) from chapter 1. However, written in this form, the connection to the transport distribution becomes explicit. Next, we assume a diagonal transport distribution tensor and write the transport distribution in Landauer form as [44]

$$\Xi\left(E\right) = \frac{2}{h}\left(M\left(E\right)/A\right)\lambda\left(E\right), \tag{2.8g}$$

where $M\left(E\right)/A$ is the number of channels for conduction per unit cross-sectional area vs. energy. (See the APPENDIX A for a derivation of (2.8g).) We compute $M\left(E\right)/A$ from a DFT-generated band structure using the open source tool, LanTrap 2.0 [79]. The energy-dependent mean-free-path for backscattering is also needed; it is defined as [44]

$$\lambda\left(E\right) \equiv 2 \frac{\left\langle v_x^2 \right\rangle}{\left\langle |v_x| \right\rangle} \tau_m\left(E\right), \tag{2.9}$$

where $\left\langle v_x^2 \right\rangle / \left\langle |v_x| \right\rangle$ is an energy dependent angle-averaged velocity and is computed from the DFT-generated band structure. For acoustic deformation potential (ADP) scattering in the elastic

limit, the scattering rate is isotropic, equal to the momentum relaxation rate, and proportional to the DOS:

$$\frac{1}{\tau(E)} = \frac{1}{\tau_m(E)} \propto K_{el-ph} DOS(E), \tag{2.10}$$

which can be computed directly from the numerical band structure. The electron-phonon coupling parameter, K_{el-ph}, is proportional to the deformation potential squared. The electron-phonon scattering rates in non-polar semiconductors generally follow the DOS [80]. The rigorously computed electron-phonon scattering rates presented in Sec. 2.5 confirm that for silicon, the scattering rate follows the DOS, so for the numerical calculations presented in Sec. 2.5, we take K_{el-ph} from the rigorously computed scattering rate. We will refer to scattering described by (2.10) as "DOS scattering." As discussed next, for parabolic energy bands and simple scattering processes, equations (2.8) simplify and can be solved analytically.

2.4 Results

2.4.1   Parabolic Bands

To illustrate how multiple, anisotropic valleys with and without intervalley scattering affects the b-factor, we present some calculations for parabolic energy bands. For parabolic bands [42], [44],

$$M(E)/A = \frac{m_\sigma^*}{2\pi\hbar^2}(E - E_C), \qquad (E - E_C) > 0 \tag{2.11}$$

where m_σ^* is the "distribution of modes" effective mass [44] (for more details on the "distribution of modes effective mass," please see APPENDIX B). It is analogous, but not equal to, the conductivity effective mass in the traditional formulation. For spherical energy bands, $m_\sigma^* = N_V m^*$, where N_V is the number of valleys and m^* is the effective mass of each valley. For the ellipsoidal conduction band of Si [44]

$$m_\sigma^* = 2m_t + 4\sqrt{m_t m_\ell} \ . \tag{2.12}$$

For spherical energy bands, the MFP for backscattering is [42]

$$\lambda(E) = \frac{4}{3} \upsilon(E) \tau_m(E), \tag{2.13}$$

which, can be written in power law form as

$$\lambda(E) = \lambda_0 \left((E - E_C)/k_B T \right)^r, \qquad (E - E_C) > 0 \tag{2.14}$$

where r is a characteristic exponent. For DOS scattering, $r = 0$, and the MFP is independent of energy. For a constant scattering time (CRTA), $r = 1/2$. By using (2.11) and (2.14) in (2.8), we find [42]

$$\sigma = \frac{2q^2}{h} \lambda \left(\frac{m_\sigma^* k_B T}{2\pi\hbar^2} \right) \Gamma(r+2) \mathcal{F}_r(\eta_F) \tag{2.15a}$$

$$S = -\left(\frac{k_B}{q} \right) \left(\frac{(r+2)\mathcal{F}_{r+1}(\eta_F)}{\mathcal{F}_r(\eta_F)} - \eta_F \right) \tag{2.15b}$$

$$\kappa_0 = T \left(\frac{k_B}{q} \right)^2 \frac{2q^2}{h} \lambda_0 \left(\frac{m_\sigma^* k_B T}{2\pi\hbar^2} \right) \times$$
$$\left[\Gamma(r+4)\mathcal{F}_{r+2}(\eta_F) - 2\eta_F \Gamma(r+3)\mathcal{F}_{r+1}(\eta_F) + \eta_F^2 \Gamma(r+2)\mathcal{F}_r(\eta_F) \right] \tag{2.15c}$$

from which the b-factor can be computed if we assume a lattice thermal conductivity, κ_L, and scattering parameters, λ_0 and r. We assume a lattice thermal conductivity of $\kappa_L = 1\,\text{W/m-K}$. All calculations are done at 300 K.

2.4.2 Spherical, parabolic bands and multiple valleys

We begin with spherical bands and consider two cases; the first assumes only intra-valley scattering and the second assumes equally strong intra- and inter-valley scattering. We assume $m_\sigma^* = N_V m_0$ and vary the valley degeneracy from $1 \leq N_V \leq 10$. When only intra-valley scattering is assumed, a MFP of $\lambda = \lambda_0 = 10$ nm independent of N_V. The second case assumes equally strong intra- and inter-valley scattering, so the MFP goes as $\lambda = \lambda_0 / N_V$. For every value of N_V the maximum zT is found by sweeping the Fermi level to find $\hat{\eta}_F$ at the maximum zT. Equation (2.11a) then gives $\sigma(\hat{\eta}_F)$ and from (2.3), $b(\hat{\eta}_F)$ is computed. Using (2.4), we can then deduce $B = b(\hat{\eta}_F) / \mathcal{F}_{1/2}(\hat{\eta}_F)$.

The results are shown in Fig. 2.1. To understand these results, note that according to (2.15a) $\sigma \propto m_\sigma^* \lambda$. When there is only intra-valley scattering, $\sigma \propto (N_V m_0) \lambda_0$, so the conductivity, and therefore the B-factor increases linearly with the number of valleys. The increase of the b-factor with N_V is, however, sub-linear. This behavior is due to the fact that the Fermi level that maximizes zT moves down as N_V increases, causing the conductivity to increase sub-linearly with N_V. The result is that the b-factor rolls over despite the fact that the Seebeck coefficient increases with N_V. Although neglecting inter-valley scattering may seem artificial, it does have some relevance to nanostructured thermoelectric materials in the "small nanostructure size" (SNS) limit [58], [59]. In this limit, the MFP is determined by grain size and independent of N_V or m^*. Under these conditions, a large N_V (or equivalently a large effective mass in a single valley) is beneficial.

When the intra and inter-valley scattering rates are equal, Fig. 2.1 shows that the B- and b-factors are independent of N_V. This follows directly from the fact that $\sigma \propto m_\sigma^* \lambda = (N_V m_0)(\lambda_0 / N_V)$ is independent of the number of valleys when inter-valley scattering is strong. Figure 2.1 illustrates the importance of accurately quantifying the relative strengths of intra- and inter-valley scattering. Figure 2.1 also shows the difference between the b- and B-

factors. Since the B-factor is well defined only for parabolic energy bands while the b-factor can be computed for arbitrary band structures, the b-factor may be more relevant for treating complex thermoelectric materials. It is also more directly related to measured quantities.
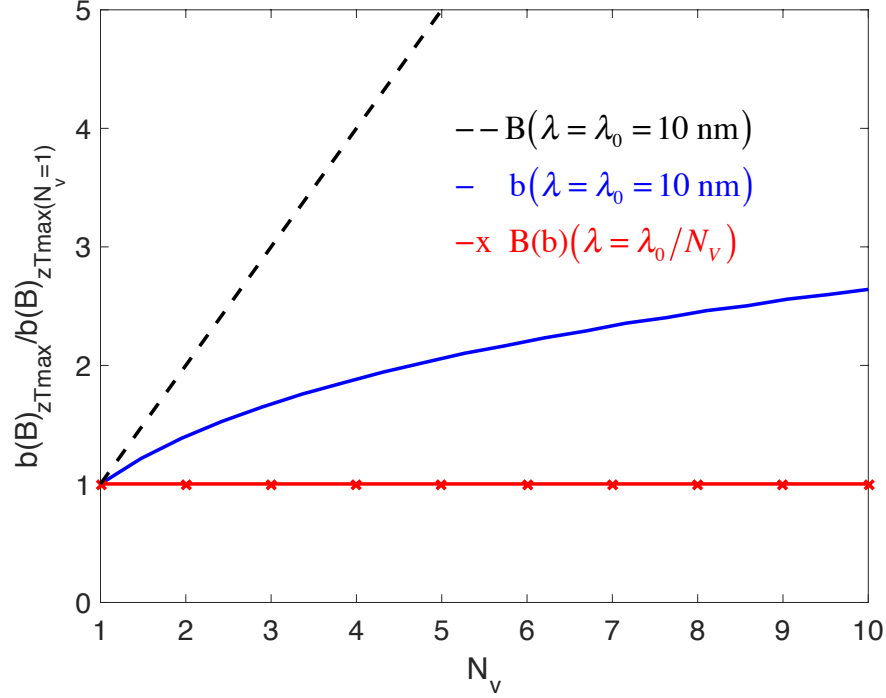
Figure 2.1. The b- and B-factors versus the number of degenerate valleys. The solid line is the b-factor assuming intra-valley scattering only (i.e. a constant MFP). The dashed line is the B-factor assuming a constant MFP. The solid line with x's is the result for both the b- and B-factors assuming equally strong intra- and inter-valley scattering. In all cases, the results are normalized to one when the number of valleys is one.

2.4.3 Silicon-like Anisotropic Valleys

Complex thermoelectric materials often have anisotropic band structures that can boost thermoelectric performance [65]. Both scattering and anisotropy affect the performance of a thermoelectric material. In this section, we use a silicon-like conduction band with six equivalent ellipsoidal bands to examine how anisotropy affects the b-factor. Three cases are considered: i) a constant MFP, ii) a constant scattering time, iii) a scattering time inversely proportional to the total DOS of all valleys. The first two cases are considered because they are commonly used assumptions. Case iii) corresponds to equally strong intra- and inter-valley scattering. The results illustrate the connection between band anisotropy and scattering.

To treat this problem, we must extend (2.13) and (2.14). Details can be found in APPENDIX B; the results are:

Case i) Constant MFP independent of energy and effective mass, $r = 0$:

$$\lambda = \lambda_0 = 10nm \tag{2.16a}$$

Case ii) Constant scattering time, $r = 1/2$,

$$\lambda(E - E_c) \propto \sqrt{(E - E_c)} \left(\frac{1/m_\ell + 2/m_t}{1/\sqrt{m_\ell} + 2/\sqrt{m_t}} \right) \tau_0 \tag{2.16b}$$

Case iii) Equally strong intra- and inter-valley DOS scattering,

$$\lambda \propto \frac{\lambda_0}{6} \left(\frac{m_t + 2m_\ell}{m_t^2 m_\ell + 2(m_t m_\ell)^{3/2}} \right). \tag{2.16c}$$

In case ii), the constant scattering time τ_0 is set using $\mu = q\tau_0/m_c^*$ with the mobility and conductivity effective mass from silicon of 1360 cm^2/Vs and 0.26 m_0 ([81] (pg.166)] respectively. In case iii), the MFP is scaled so that, $\lambda(m_\ell = 0.93m_0, m_t = 0.19m_0) = 10nm$. In each case, the transverse effective mass m_t/m_0 is varied with m_ℓ/m_0 held constant at $m_\ell/m_0 = 0.93$. For every m_t/m_0 value, the Fermi level is swept to find $\hat{\eta}_F$ at the maximum zT. Equation (2.15a) then gives $\sigma(\hat{\eta}_F)$ and from (2.3), $b(\hat{\eta}_F)$ is computed. Using (2.5), we then compute $B = b(\hat{\eta}_F)/\mathcal{F}_{1/2}(\hat{\eta}_F)$. Only the b-factor will be shown, because the B-factor displays the same trends.

The results are shown in Fig. 2.2. For the constant MFP case, the b-factor continues to **increase** with increasing m_t (decreasing anisotropy). This behavior is similar to the constant MFP case shown in Fig. 2.1 and occurs because $\sigma \propto m_\sigma^*$ when the MFP is constant, and according to (2.12), m_σ^* increases as m_t increases. For a constant scattering time, Fig. 2.2 shows

36

that the b-factor increases more slowly with increasing m_t. This occurs because an increasing m_t increases m_σ^*, but it decreases the velocity so the MFP decreases with increasing m_t according to (2.16b). In case iii), however, the trend is opposite to that of cases i) and ii). Even though m_σ^* increases as m_t increases, the MFP decreases rapidly and continues to do so with increasing m_t according to (2.16c). This occurs because the increasing m_t lowers the velocity and increases the DOS, which lowers the scattering time. Because the MFP is the product of velocity and scattering time, it decreases rapidly within increasing m_t/m_0. In the end, cases i) and ii) benefit from a larger transverse effective mass, while case iii) is maximum for a transverse effective mass approaching zero. The large differences in Fig. 2.2 at $m_t/m_0 = 0.19$ (the Si value) illustrate the importance of a proper treatment of scattering.

The fact that different types of scattering and anisotropies affect thermoelectric performance is well understood (e.g. [11], [39], [57], [60]), but the interplay of scattering, anisotropy, and valley degeneracy is not well understood [77]. In the next section, we examine scattering in anisotropic, multi-valley semiconductors by using a DFT-generated silicon band structure and rigorously computed electron-phonon scattering rates.
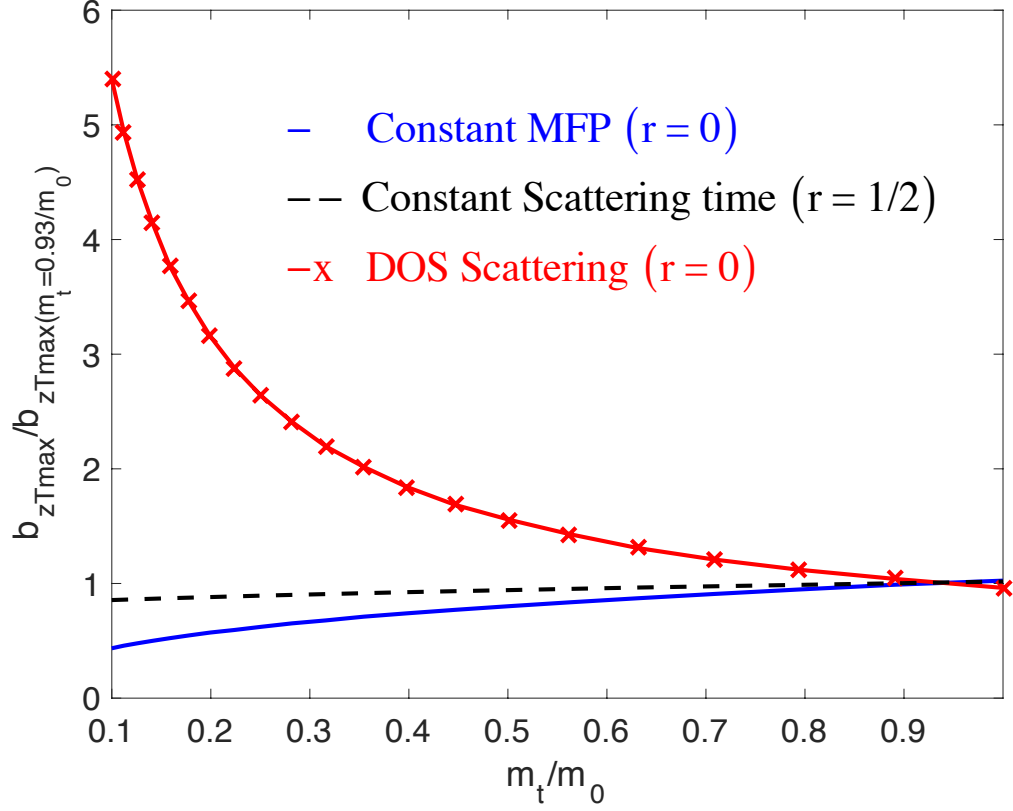
Figure 2.2. Normalized b-factor vs. increasing m_t^*/m_0 (decreasing anisotropy). The solid line assumes a constant MFP, case i). The dashed line assumes a constant scattering time, case ii), and the solid line with x's, assumes a scattering rate proportional to the total DOS, case iii). In all cases the b-factors are normalized to one when the valleys are spherical with $m_t = m_\ell$.

2.5 Numerical bands and scattering rates

Thermoelectric materials generally have complex band structures that can only be described numerically. As illustrated here for the relatively simple case of silicon, an assessment of the performance potential of a material cannot be done without a careful consideration of how band structure affects electron scattering. The main challenge in doing such calculations is the specification of $\lambda(E)$. As discussed below, rigorous, first-principles calculations of the electron scattering time [68]–[72], [82] can be used to determine $\lambda(E)$.

2.5.1 Numerical calculation of scattering rates

The numerical calculations were done as follows. The structural relaxation, self-consistent ground state, and DFPT calculations were performed with the Quantum Espresso package [52], using Perdew-Zunger LDA exchange-correlation, norm-conserving pseudo-potential, a 48 Ry plane wave energy cutoff, and a 16×16×16 Monkhorst-Pack k-mesh. The converged lattice constant is 5.38 Å in agreement with similar DFT studies [72]. The scattering rate calculations were performed with the EPW package [68], [69] to extract both the relaxation time and the momentum relaxation time at 300 K [70]. Electronic energies, phonon energies, and the electron-phonon matrix elements were initially calculated for zone-centered 6×6×6 coarse k- and q-grids. Eight maximally localized Wannier functions [82] of sp^3 symmetry were generated and serve as the basis to transform the electronic Hamiltonian, phonon dynamical matrix, and el-ph coupling Hamiltonian. From the Wannier representation, the electron and phonon energies and el-ph coupling matrix elements are interpolated onto dense k- and q-grids of 60×60×60 and used to calculate the scattering rate. A Gaussian smearing parameter of 30 meV was used for energy conservation. To reduce computation time, only those k-points in the irreducible wedge of the Brillouin zone were included in the analysis. The carrier concentration, determined from the Wannier representation density-of-states (DOS) [82], was chosen as 10^{15} cm^{-3}. To distinguish intra-valley and inter-valley scattering processes, inter-valley transitions were identified when the change in the electron wave vector was $|q| > 0.505$ Å^{-1} (0.25 in reduced coordinates) or when there was a change in band number when going from initial to final band. All other transitions were categorized as intra-valley scattering.

Figure 2.3 shows the computed scattering rate vs. energy for electrons in the conduction band of silicon. Each value plotted represents a distinct point in k-space. Figure 2.3 shows that both the scattering rate (points) and momentum relaxation rate (+) follow the DOS (line). The fact that the momentum relaxation rate and scattering rate are basically equal indicates that electron-phonon scattering is isotropic in silicon, as expected [81]. These numerical calculations confirm that for n-Si, $1/\tau_m(E) \propto DOS(E)$, as expected from simpler, phenomenological treatments [80], [81].
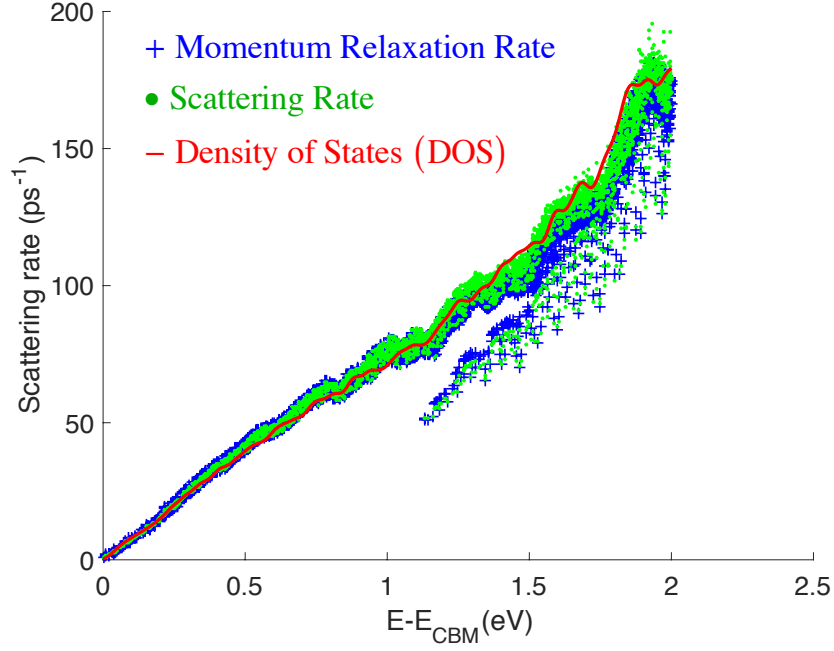
Figure 2.3. Scattering rate vs. energy for electrons in the conduction band of silicon. Each point represents a point in k-space. The results show that the scattering rate (points) depends primarily on the energy of the state and not its location in k-space. The + symbols are the momentum relaxation rate, which is essentially the same as the scattering rate in silicon. Both the scattering rate and momentum relaxation rate follow the density-of-states (line), especially around the energy most relevant for transport, $E - E_C \ll 1\,\text{eV}$.

The next question concerns the relative importance of intra- vs. inter-valley scattering. As discussed earlier, the benefits of multiple valleys are reduced if inter-valley scattering dominates. A phenomenological treatment indicated that both intra- and inter-valley scattering are important in n-Si [83]. Figure 2.4, which compares numerically calculated intra-valley and inter-valley scattering rates for electrons in the conduction band of silicon, shows that inter-valley scattering dominates in this material. Near the band edge, which is what matters for the thermoelectric coefficients, the inter-valley scattering rate per valley is comparable to that of intra-valley, i.e. there is equal probability to scatter to any valley. The numerical calculations also provide the room temperature, phonon-limited mobility in bulk Si as $\mu_n = 1480$ cm^2/V-s, which is within 10% of the experimental value of 1360 cm^2/V-s [83] and suggests that the calculations are reliable. Finally, the calculations also provide a rigorous solution to the BTE, which shows that the RTA, which is assumed in eqns. (2.8), is accurate to within a few percent.
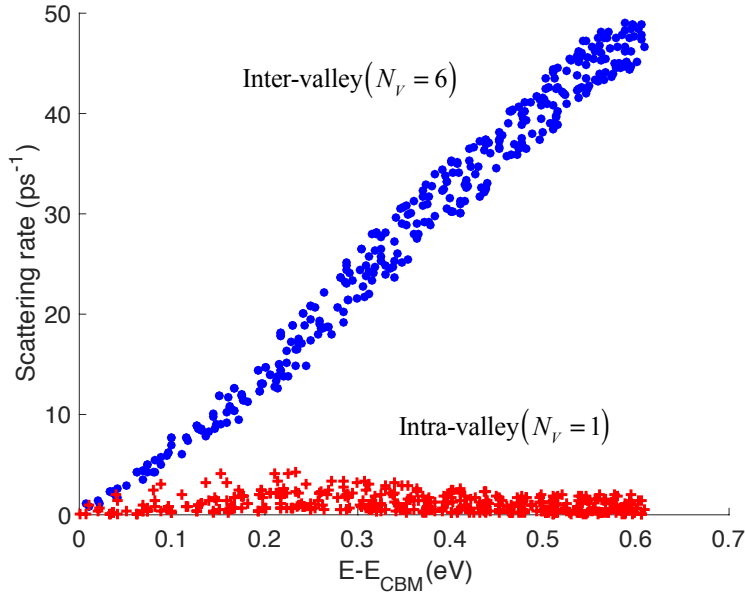
Figure 2.4. Scattering rate vs. energy for electrons in the conduction band of silicon. In the plot, the + symbols show the intra-valley scattering rate and the points show the inter-valley scattering rate. Near the band edge, i.e. $E < 0.1\,\text{eV}$ there is roughly the same probability to scatter within a valley as to scatter to a different valley.

2.5.2   Calculation of the b-factor

When discussing the benefits of multiple, anisotropic valleys, the point of comparison is a corresponding (in some appropriate sense) spherical valley semiconductor. The calculations presented next will compare the performance of the n-Si using a rigorous band structure with corresponding spherical models. From the rigorous calculations shown in Fig. 2.3, we extract the electron-phonon coupling parameter, K_{el-ph} needed in (2.10). Equations (2.8) can then be solved using (2.9) and (2.10) to specify the energy-dependent MFP. The distribution of channels, $M(E)$, is extracted directly from the band structure using LanTrap 2.0 [79], and the angle-averaged velocity, $\langle v_x^2 \rangle / \langle |v_x| \rangle$, which is needed for $\lambda(E)$, is also computed directly from the band structure. With this information, (2.8) can be solved repeatedly as the Fermi level is swept to find $\hat{\eta}_F$ at the maximum zT. As in the parabolic band case, for these model calculations, we assume $\kappa_L = 1\,\text{W/m-K}$ rather the actual value for Si. This procedure provides $\sigma(\hat{\eta}_F)$, the conductivity at peak zT, and from (2.3), $b(\hat{\eta}_F)$ is computed. Since the b-factor is well-defined

for general band structures, but the B-factor only applies to parabolic band semiconductors, we will focus on the b-factor.

Table 2.1 shows the computed b-factors for several different cases. Case A1 uses the full, numerical Si conduction band and assumes equally strong intra- and inter-valley scattering. Case A2 assumes only intra-valley scattering with K_{el-ph} being replaced by $K_{el-ph}/6$. This example enjoys the benefits of six valleys without suffering from increased scattering between valleys, therefore the b-factor should be larger. Table 2.1 shows that the b-factor is significantly larger when inter-valley scattering is ignored (case A1 vs. A2).
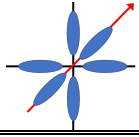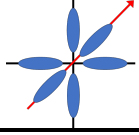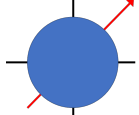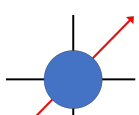
When complex band structures are anisotropic in the right way, they can boost zT even when scattering between valleys occurs. Case B1 in Table 2.1 displays the b-factor for a corresponding spherical band. The effective mass of this spherical band is chosen to give the same $M(E)$ as the full, numerical band. Because the Si conduction band is nearly parabolic, the numerically extracted $M(E)$ closely follows the analytical expression for parabolic bands, (2.11). From the numerical $M(E)$, we extract m_σ^* and then set the effective mass of the corresponding spherical band to $m^* = m_\sigma^*$. This procedure would give the same conductivity in Cases A1 and B1, if the MFP's in the two cases were the same.

The procedure described above produces, however, a different MFP, $\lambda(E)$, from case A1 for two reasons. The first reason is that this process produces different DOS's for the two cases, and therefore, different scattering times according to (2.10). The second reason is that the velocity ratio, $\langle v_x^2 \rangle / \langle |v_x| \rangle$ in the MFP expression, (2.9), is smaller for the corresponding spherical band because the benefits of anisotropy are absent. Since we are interested in ascertaining the benefits of anisotropy in Case B1, we assume the same scattering times as in Case A1, but instead of using the numerically calculated $\langle v_x^2 \rangle / \langle |v_x| \rangle$, we use the smaller value for a spherical band, $\langle v_x^2 \rangle / \langle |v_x| \rangle = 2\sqrt{2(E - E_C)/m^*}/3$. Comparing the b-factor in Case B1 of Table 2.1 to Case A1, we see that anisotropy increases the b-factor by a factor of 1.24 for the case of n-Si.

Finally, case B2 assumes a spherical, parabolic energy band with an effective mass chosen to give one-sixth of the $M(E)$ as the full, numerical band. While case B1 represents all six conduction band valleys with a single spherical energy band, case B2 represents only a single conduction band valley with a spherical energy band. In this case, we assume a scattering time that is six times longer than for case A1, to account for the fact that there is no inter-valley scattering in case B2. In comparison to case B2, case A1 benefits from six times as many valleys and from valley anisotropy, but it suffers from six times as much scattering. Comparing the b-factor in case B2 of Table 1 to case A1, we see that the case A1 b-factor is 2.6 times that of case B2. The benefit of the six valleys is offset by six times more scattering, and the improvement is due to valley anisotropy.

In summary, for n-Si, the advantages of the six conduction band valleys are offset by the increased scattering of electrons between the valleys. The anisotropy of the valleys, however, provides a light effective mass in the direction of transport, which increases the b-factor in comparison to a corresponding spherical valley. To assess the potential of a thermoelectric material, the beneficial effects of valley anisotropy and valley degeneracy must be weighed against the detrimental effects of inter-valley/band scattering.

Table 2.1. Comparison of the b-factors as computed from a numerical solution with inter-valley scattering (A1) and without (A2) to corresponding spherical bands with (B1) and without (B2) inter-valley scattering. The extracted effective masses from the silicon band structure are $m_t = 0.22$ and $m_l = 0.93$ for transverse and longitudinal directions respectively, which gives $m_\sigma^* = 2.24 m_o$.

Case	Band structure	Scattering	$b(\hat{\eta}_F)$	$\hat{\eta}_F$
A1	Silicon full band m_σ^*	Intra- **and** inter-valley	0.51	-2.3
A2	Silicon full band m_σ^*	Intra-valley **only**	0.79	-3.5
B1	Single spherical valley $m^* = m_\sigma^*$	Intra- **and** inter-valley	0.41	-1.5
B2	Single spherical valley with $m^* = m_\sigma^*/6$	Intra-valley **only**	0.20	0

2.6 Discussion

Several authors have developed measures of Fermi surface complexity. For example, Mecholsky, et al. developed measures for the warped valences bands of Si [84], and Toberer discusses a shape factor [75]. Recently, Gibbs, et al. introduced a simple, numerical metric they call a Fermi Surface Complexity Factor (FSCF) [85],

$$FSCF = \left(\frac{m_s^*}{m_c^*} \right)^{3/2} = N_V^* K^*,$$ (2.17)

where m_S^* is the so-called Seebeck effective mass (which is the density-of-states effective mass determined from the Seebeck coefficient) and m_c^* is the conventional conductivity effective mass [81], [86]. Metrics like this are useful in identifying promising thermoelectric materials in high-throughput searches of material databases [58], [87]–[92]. In (2.17), K^* is an anisotropy factor that provides a measure of the benefits of Fermi surface anisotropy.

Equation (2.17) is an attempt to provide a simple numerical measure of how much better a complex band structure is as compared to a corresponding spherical, parabolic band. For a single valley with an effective mass of m^*, (2.17) gives $FSCF = 1$. For N_V spherical valleys with an effective mass of m^*, (2.17) gives $FSCF = N_V$ (because $m_S^* \propto N_V^{2/3}$). Inserting numbers relevant for the conduction band of Si $\left(N_V = 6, m_t = 0.19 m_0, m_\ell = 0.93 m_0 \right)$, we find $FSCF \approx 8.35$, which reflects both the benefits of a valley degeneracy of 6 and the valley anisotropy, which produces a light effective mass in the direction of transport (in this case, $K^* = 8.35/6 = 1.39$). Comparing case B2 to case A1 in Table 2.1, we see that in the presence of strong inter-valley scattering, $FSCF$ is an overly optimistic measure of the benefits of the anisotropic, multi-valley conduction band of Si. The anisotropy factor itself is a better indicator in this case, because the benefits of the additional valleys are offset by additional intervalley scattering.

The benefits of anisotropy in the presence of strong inter-valley scattering can be assessed by assuming that electron-phonon scattering follows the total DOS as given by (2.10). In this case, it is easy to show from (2.8f) to (2.8g) that the transport distribution simplifies to

$$\Xi(E) = \frac{\left\langle v_x^2(E) \right\rangle}{K_{el-ph}}.$$ (2.18)

Recall that the brackets indicate an average over angles at the energy, E. The fact that $v_x^2(E)$ plays an important role in thermoelectric performance has been noted before (e.g. in [56]). By

energy-averaging the angle-averaged velocity squared, $\langle v_x^2(E) \rangle$, over the Fermi window, a metric sensitive to anisotropy and not to the number of valleys would result. Thus, $\langle v_x^2(E) \rangle$ could be a good measure of potential anisotropic enhancement.

2.7 Summary

Assessing the performance potential of a complex thermoelectric material involves a careful consideration of the number of valleys and bands that participate in transport, the role of scattering between these valleys and bands, and the effects of anisotropy. We illustrated how these issues can be examined by using n-type Si dominated by electron-phonon scattering as a model material. The calculations presented illustrate how rigorous treatments of electron scattering can inform calculations done by solving the Boltzmann Transport Equation in the Relaxation Time Approximation (RTA) as given by eqns. (2.8). For complex materials, these calculations can be computationally demanding, but they can address important questions such as the validity of the RTA, the use of energy-dependent rather than k-dependent scattering times, the relative strengths of intra- vs. inter-valley/band scattering, the energy dependence of the scattering time, etc.

The calculations presented here show that the degree to which multiple anisotropic valleys improve *zT* depends sensitively on the relative strengths of intra- vs. inter-valley electron scattering processes. This fact is well known; the contribution of this chapter is to show how this question can be quantitatively addressed. Anisotropy also plays an important role, and by assuming equally strong scattering within and between valleys, its effect can be assessed by a metric based on $\langle v_x^2(E) \rangle$. Widely used approximations, such as the constant relaxation time approximation (CRTA) and the constant mean-free-path approximation are not suitable for understanding the performance potential of a complex thermoelectric material with multiple valleys and bands. As illustrated in this chapter, a combination of rigorous scattering calculations and standard RTA based solutions of the BTE may provide a more realistic way to assess the potential of complex materials.

3 ON THE UNIVERSAL BEHAVIOR OF THE THERMOELECTRIC FIGURE OF MERIT

3.1 Preface

The contents of this chapter have been extracted from the following publications with permission: E. Witkoske, X. Wang, J. Maassen, and M. Lundstrom, "Universal behavior of the thermoelectric figure of merit, zT, vs. quality factor," *Mater. Today Phys.*, vol. 8, pp. 43–48, 2019.

3.2 Introduction

The performance of a thermoelectric material is directly related to its material figure of merit,

$$zT = \frac{S^2 \sigma T}{\kappa_L + \kappa_e} ,$$

(3.1)

where S is the Seebeck coefficient, σ the electrical conductivity, κ_L and κ_e the lattice and electronic thermal conductivities, and T is the temperature. One way to improve zT is to reduce the lattice thermal conductivity without significantly degrading the electronic properties [93]. Over the past two decades, this strategy has been quite successful [6], [7], [11], [12]; κ_L is approaching the practical lower limit of $\kappa_L = 0.2 \, \text{W/m-K}$ identified in [93]. The material figure of merit was $zT \approx 1$ when [93] was written; since then, there have been several reports of $zT > 2$ (e.g. [11], [22], [94]). Device and manufacturing issues must be addressed to turn recent advances in material performance into improved device performance [13], but additional improvements in material performance are also needed. It seems likely that progress in reducing κ_L will slow; so further advances in zT will have to come by improving the electronic performance. Several ideas to enhance the electronic performance of thermoelectric materials have been proposed, but success has been elusive.

The relation of S, σ, and κ_e to TE properties is well understood within the context of a simple, parabolic band model [2], [40] for which the only thing that matters is the magnitude of

the TE quality factor (B-factor), which is proportional to the ratio of the electrical conductivity to the lattice thermal conductivity [61], [74], [95]. Such analyses suggest that a high zT will not be possible in a simple semiconductor – implying that high performance, if possible at all, will only occur in materials with unusual or complex electronic features [56]. Here we define a "complex" band structure as any band structure other than a simple parabolic band. Because so many factors are involved and because the electronic transport coefficients are so tightly coupled, identifying a complex material with the promise of significantly out-performing a simple parabolic band is hard to do in a clear and convincing way. Over the past two decades, many proposals to enhance the electronic performance of thermoelectrics have been presented [21], [77], [96]–[101]. There is a need for a clear way to compare complex TE materials and engineered structures on a common basis to determine whether there is any electronic structure that can significantly out-perform a simple parabolic energy band.

In this chapter, we present simulations that suggest a plot of the peak zT (i.e. the zT at the optimum Fermi level, $\hat{E}_F$) vs. a generalized quality factor at the peak zT is a universal characteristic. We present results for more than a dozen widely different electronic structures and show that none exceeds the performance of a simple, parabolic band material with acoustic deformation potential scattering. A simple argument explains the results and suggests that no complex thermoelectric material will out-perform a material with simple, parabolic energy bands. The result, however, is not fundamental, if materials that substantially exceed the parabolic band limit can be found, they will provide new routes to increasing zT .

3.3 Approach

A brief description of the computational techniques employed follows; a more extensive discussion can be found in the supplementary information.

Equation (3.1) can be re-expressed as

$$zT = \frac{S'^2}{L' + 1/b_L} ,$$

(3.2)

where $S' = S/(k_B/q)$ is the dimensionless Seebeck coefficient, $L' = L/(k_B/q)^2$ the dimensionless Lorenz number, and

$$b_L(E_F) \equiv \frac{\sigma(E_F)T}{\kappa_L}(k_B/q)^2 \qquad (3.3)$$

is a generalized b-factor; it is closely related (see [102]) to the B-factor discussed by Mahan [40], [95], which is also the "material factor" β introduced by Chasmar and Stratton [74]. The important role that the B-factor (also called the quality factor) plays in thermoelectric materials has been discussed by Wang et al. [61]. As noted by Mahan, in the absence of bipolar effects, zT is a function of B (or b_L) alone and does not depend independently on the parameters, S, σ or κ_L [40].

The relation between B and $b_L(E_F)$ is simple and is given by eqn. (3.9) in Sec. 3.6. The key difference is that $b_L(E_F)$ depends on Fermi level and B does not. The second key difference is that $b_L(E_F)$ is defined for any band structure while B is only defined for parabolic energy bands. Because our focus is on complex band structures, we will work with $b_L(E_F)$ in this chapter. To calibrate readers, note that for parabolic bands with B = 0.4, we find $b_L(E_F \approx E_C) = 0.18$. For more discussion, see the supplementary information.

The material figure of merit increases without limit as the b-factor increases, but the magnitude of the b-factor is, however, not the whole story. In this chapter, we ask the question: "Are there materials or engineered structures that provide *at the same b-factor* a higher zT than a material with a simple parabolic band?" Large b-factors will always be necessary, but if the answer to this question is yes, new options for increasing zT will open up.

By solving the Boltzmann Transport Equation in the Relaxation Time Approximation, we find the thermoelectric transport parameters as

$$\sigma = \int_{-\infty}^{+\infty} \sigma'(E)\, dE \tag{3.4a}$$

$$S = -\frac{1}{qT} \int_{-\infty}^{+\infty} (E - E_F)\sigma'(E)\, dE \left/ \int_{-\infty}^{+\infty} \sigma'(E)\, dE \right. \tag{3.4b}$$

$$\kappa_0 = \frac{1}{q^2 T} \int_{-\infty}^{+\infty} (E - E_F)^2 \sigma'(E)\, dE = \kappa_e + T\sigma S^2 \tag{3.4c}$$

where the differential conductivity, $\sigma'(E)$, is

$$\sigma'(E) = q^2 \Xi(E)(-\partial f_0 / \partial E), \tag{3.4d}$$

and the transport distribution in the diffusive limit [44],

$$\Xi(E) = \frac{2}{h}\big(M(E)/A\big)\lambda(E), \tag{3.4e}$$

is written in Landauer form with $M(E)/A$ being the number of channels per cross-sectional area for conduction and $\lambda(E)$ the mean-free-path (MFP) for backscattering. In (3.4c), κ_0 is the electronic thermal conductivity measured under short circuit conditions, and κ_e is the same quantity measured under open circuit conditions. See the appendix in [23] for a short derivation of (3.4e) and [24] for a longer discussion.

In (3.4e), the mean-free-path for backscattering is defined as [24]

$$\lambda(E) \equiv 2v_x^2(E)\tau_m(E) / v_x^+(E), \tag{3.5a}$$

where $v_x^2(E)$ is an average over angle of the quantity $v_x^2(\vec{k})$ at energy, E. The velocity, $v_x^+(E)$, is the angle-averaged velocity in the +x direction (see [24] for the definitions of these averages). The number of channels at energy, E, is [24], [25]

$$M(E)/A = h\upsilon_x^+(E)D(E)/4 ,$$ (3.5b)

where $D(E)$ is the density-of-states per unit volume including a factor of two for spin.

The treatment of electron scattering is an important consideration in any TE calculation. The use of an energy-independent momentum relaxation time, τ_m can lead to errors [23], [26]. A better assumption when isotropic electron-phonon scattering dominates is that the scattering rate follows the density-of-states [93],

$$\frac{1}{\tau(E)} = \frac{1}{\tau_m(E)} \propto K_{el-ph}D(E),$$ (3.5c)

where K_{el-ph} describes the electron-phonon coupling, τ is the scattering time, and τ_m is the momentum relaxation time. The density of states in equation (3.5c) relates to the states within each individually band, and commonly describes phonon scattering in non-polar semiconductors [23], [27]. As discussed [26], it also seems to describe some TE materials and appears to be a much better approximation than the assumption of a constant scattering time. Rigorous treatments of electron scattering are available to provide material-specific scattering times [28]–[32]. Finally, we note that when plotting zT vs. b_L, K_{el-ph} is not needed because S' and L' only depend on the energy dependence of the scattering rate – not on its magnitude.

3.4 Results

3.4.1 Parabolic Energy Bands

Equations (3.4) and (3.5) can be solved numerically given a full, numerical description of the energy band (see the supplementary material of [23], [26]). Equations (3.2) and (3.3) can also be solved analytically for simple parabolic band structures (the results are presented in the appendix of [25]). For parabolic energy bands with power law scattering,

$$\lambda(E) = \lambda_0\left[(E - E_C)/k_BT\right]^r,$$ (3.6)

51

where r is a characteristic exponent. For acoustic deformation potential (ADP) scattering in 3D parabolic bands, $r = 0$; the MFP is independent of energy. For ionized impurity (II) scattering, $r = 2$. By assuming a temperature, effective mass, MFP (λ_0), characteristic exponent, r, and lattice thermal conductivity, κ_L, one can sweep the Fermi level and produce a plot of $zT(E_F)$ vs. $b_L(E_F)$. Results are shown in Fig. 1 for several different values of κ_L.
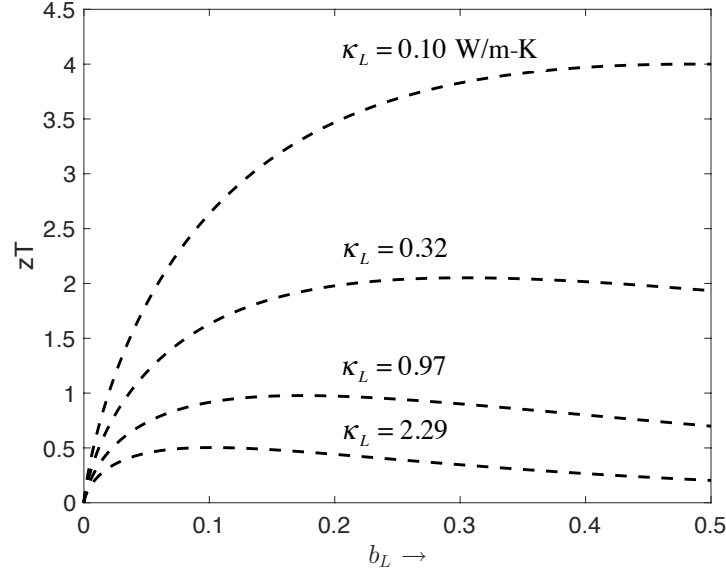
Figure 3.1. Material figure of merit, zT vs. b_L for $\kappa_L = 0.10$, 0.32, 0.97, and 2.29 W/m-K, which were selected to produce peak zT's of 4, 2, 1, and 0.5 using a n-type Bi₂Te₃ parabolic conduction band with $m^* = 1.56 m_0$ and an energy-independent ($r = 0$) MFP of $\lambda_0 = 25$ nm. As the Fermi level increases, b_L increases because $\sigma(E_F)$ increases.

For each κ_L in Fig. 3.1, there is a maximum in zT as the Fermi level is swept. By plotting zT vs. b_L at the peak zT where $E_F = \hat{E}_F$, the results in Fig. 3.2 are obtained. Each point on the $zT(\hat{E}_F)$ vs. $b_L(\hat{E}_F)$ characteristic is the value of zT and b_L at the Fermi level that maximizes zT. The $zT(\hat{E}_F)$ vs. $b_L(\hat{E}_F)$ characteristic is independent of how b_L is varied (i.e. by varying κ_L as in Fig. 3.1, the MFP parameter λ_0, or the effective mass). The characteristic is also independent of temperature. (We should note, however, that these calculations do not include bipolar conduction; when they are considered, the characteristic is temperature dependent and

52

sensitive to the ratio of mean-free-paths and effective masses.) Figure 3.2 compares the $zT(\hat{E}_F)$

vs. $b_L(\hat{E}_F)$ characteristic for 3D, parabolic bands with ADP scattering ($r = 0$) to that for II

scattering ($r = 2$). Also shown is the single energy channel case [93].
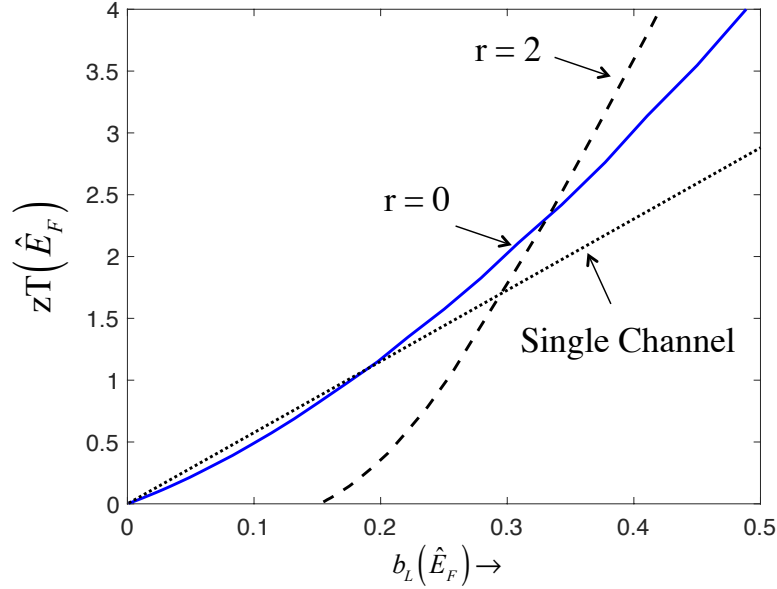
Figure 3.2. Peak material figures of merit, $zT(\hat{E}_F)$ vs. $b_L(\hat{E}_F)$, the value of b_L at the Fermi level
that maximizes zT. Solid line: Parabolic bands with $r = 0$ in eqn. (6b). Dashed line: Parabolic
bands with $r = 2$. Dotted line: Single energy channel.

Finally, the distinction between $b_L(E_F)$ and $b_L(\hat{E}_F)$ should be kept in mind. Figure 3.1 is a

plot of $zT(E_F)$ vs. $b_L(E_F)$. The Fermi level that maximizes zT is $E_F = \hat{E}_F$, Figure 3.2 is a plot

of $zT(\hat{E}_F)$ vs. $b_L(\hat{E}_F)$. For ADP scattering ($r = 0$) $\left|S'(\hat{E}_F)\right|$ increases with $b_L(\hat{E}_F)$ because as

b_L increases, the Fermi level at peak zT drops below the band edge (see Figs. 1a and 4 of

[102]). The Lorenz number is close to its non-degenerate limit of two and saturates at two for

large $b_L(\hat{E}_F)$. For II scattering ($r = 2$), the peak Fermi level for small b-factors lies deep in the

conduction band where $|S|$ and therefore zT approach zero [104]. For $b_L > 0.35$, the Fermi level

at the peak zT moves below the band edge, and II scattering produces a high Lorenz number

approaching four, which is detrimental because L' is in the denominator of (2). For large b-factors however, the very large S'^2 for II scattering causes this case to out-perform the ADP scattering case, as shown in Fig. 3.2. The II scattering case shows that it is possible to exceed the parabolic band/ADP scattering limit with the right type of energy-dependent scattering. In practice, II scattering often occurs in addition to electron-phonon scattering, which lowers the overall MFP and reduces zT. The point here is that with the right energy dependence to the transport function (which is proportional to the product of the number of channels and the MFP, eqn. (3.4e)), then the parabolic band / ADP limit can be exceeded.

Figure 3.2 also compares the peak $zT\left(\hat{E}_F\right)$ vs. $b_L\left(\hat{E}_F\right)$ characteristics for parabolic bands to the single energy channel case,

$$M\left(E\right)\big/A = M_0\delta\left(E - E_C\right), \tag{3.7}$$

where E_C is the energy of the channel. The single energy channel case displays n-type conduction when $E_F < E_C$. In contrast to the parabolic band case, the Fermi level at the peak zT is independent of b_L, i.e. $\left(E_F - E_C\right)\big/k_BT = -2.4 = S'$. For a single energy channel, $L' = 0$ [93], so equation (3.2) gives $zT = \left(S'\right)^2 b_L = 5.75b_L$. As shown in Fig. 3.2, a single energy channel provides little benefit over a parabolic band when $zT < 1$ and under-performs a parabolic band when $zT > 1$. These results support the conclusion of [105], [106] that a delta-function transport distribution is not the best for thermoelectric performance, but the magnitude of the b-factor must be considered as well.

Analytical results provide reference points for comparison to the full, numerical solutions of the thermoelectric equations that are considered next. As we examine the influence of complex band structures on the $zT\left(\hat{E}_F\right)$ vs. $b_L\left(\hat{E}_F\right)$ characteristic, the parabolic band with ADP scattering case will serve as our reference because ADP scattering is thought to dominate in many TE materials [2]. Note that for ADP scattering in parabolic bands ($r = 0$ in eqn. (3.6)), the scattering rate follows the parabolic band density-of-states.

3.4.2 Complex Energy Bands

Thermoelectric materials typically have complex band structures with multiple, anisotropic bands or pockets. In this chapter, we will refer to any band structure that is more complicated than a single, parabolic band as "complex." Recent work shows, for example, that the Lorenz number can be significantly different from the value computed for a parabolic band [26]. Higher $zT's$ might be possible with materials that offer a higher Seebeck coefficient or a lower Lorenz number (e.g. [12], [21], [75], [96]–[99], [101]). To examine this possibility, we present full, numerical simulations analogous to the analytical calculations discussed above. The numerical methods used are described in the supplementary information of [102] and [103]. The key input is a band structure from density functional theory (DFT) simulations.

Figure 3 compares the computed $zT\left(\hat{E}_F\right)$ vs. $b_L\left(\hat{E}_F\right)$ characteristics using density of states (DOS) scattering as described by eqn. (3.5c) for nine complex band structures, p-Bi_2Te_3, n-Bi_2Te_3, p-SnSe, n-SnSe, p-Sb_2Te_3, n-$Bi_{0.85}Sb_{0.15}$, p- $Bi_{0.85}Sb_{0.15}$, an n-Bi_2Te_3 quintuple layer, a p-Bi_2Te_3 quintuple layer, p-Mg_3Sb_2, and p-GeTe, to that of a simple, parabolic energy band with ADP scattering (r = 0). The $zT\left(\hat{E}_F\right)$ vs. $b_L\left(\hat{E}_F\right)$ characteristics shown in Fig. 3.3 are insensitive to how the b-factor is varied. The b-factor can be changed by varying κ_L in equation (3.1), which was done in Fig. 3.3, or by varying the electron-phonon coupling parameter in (3.5c), which varies σ in equation (3.1), but just as we found for the analytical calculations, the same $zT\left(\hat{E}_F\right)$ vs. $b_L\left(\hat{E}_F\right)$ characteristic is obtained. The numerical calculations also show that the characteristic is relatively insensitive to temperature. (We remind the reader, however, that bipolar effects are not considered.)

The cases shown in Fig. 3.3 explore a broad (though not exhaustive) range of complex band structures. What stands out in Fig. 3.3 is the fact that the results of numerical calculations for a variety of materials with complex band structures are remarkably similar to the analytical calculations assuming a parabolic band with ADP scattering. The p-Bi_2Te_3 quintuple layer is a 2D material with a band structure that is thought to be advantageous for thermoelectrics [37], but its performance is no better than that of a material with a simple parabolic energy band. These results suggest that only the magnitude of the b-factor matters. For a given b-factor, all

thermoelectric materials seem to provide nearly the same peak zT. As discussed next, however, these results assume a particular treatment of scattering.
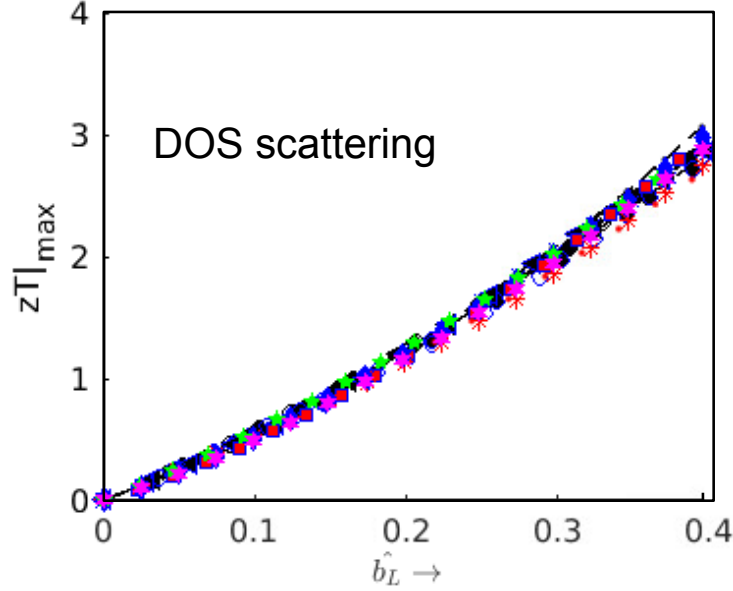
Figure 3.3. Material figure of merit, peak zT vs. $\hat{b}_L$ at 300K, for several different complex thermoelectric materials assuming a scattering rate proportional to the density of states. Open circles are for p-Bi_2Te_3 and filled circles for n-Bi_2Te_3. Open squares are for p-SnSe and filled squares for n-SnSe. Filled triangles are for p-Sb_2Te_3. Asterisks are for n-$Bi_{0.85}Sb_{0.15}$ and x-marks are for p-$Bi_{0.85}Sb_{0.15}$. Stars are for an n-Bi_2Te_3 quintuple layer, and diamonds are for p-Bi_2Te_3 quintuple layer. Pentagons are p-Mg_3Sb_2 and red dots are p-GeTe. The dashed line is the parabolic band reference assuming $r = 0$.

3.5 Discussion

Two key factors in the calculations presented in Fig. 3.3 are the band structure and electron scattering. The band structures were computed by DFT simulation. The results presented in Fig. 3.3 assumed that the electron-phonon scattering rate follows the total density-of-states according to (3.5c) with the assumption that the intra-valley/band coupling strength is equal to the inter-valley/band coupling strength. Rigorous treatments of electron-phonon scattering suggest that it is a good assumption for Si [23] and for SnSe [26]. If we were to suppress inter-valley/band scattering, a possibility when multiple bands of the same energy are separated in k-space with a lack phonon q-vectors available to scatter carriers from one point in k-space to another, the $zT\left(\hat{E}_F\right)$ vs. $b_L\left(\hat{E}_F\right)$ characteristic would not change. What would change is that for a given

electron-phonon coupling strength, the conductivity with less inter-valley scattering would be higher than the conductivity with inter-valley scattering. The b-factor, and therefore, zT, would increase respectively.

To examine the sensitivity of the results to the treatment of carrier scattering, we repeated the calculations with the assumption of a constant mean-free-path. The results are shown in Fig. 3.4. Although the constant mean-free-path assumption produces more spread about the parabolic band reference, the results shown in Figs. 3.3 and 3.4 show that the $zT\left(\hat{E}_F\right)$ vs. $b_L\left(\hat{E}_F\right)$ characteristic is relatively insensitive to the details of band structure and carrier scattering.
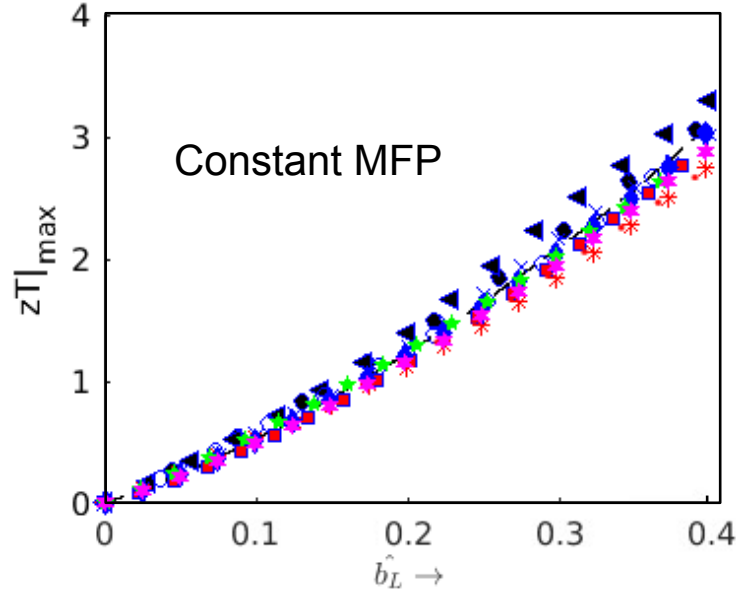
Figure 3.4. Material figure of merit, peak zT vs. $\hat{b}_L$ at 300K, for several different complex thermoelectric materials assuming a constant MFP for scattering. Open circles are for p-Bi$_2$Te$_3$ and filled circles for n-Bi$_2$Te$_3$. Open squares are for p-SnSe and filled squares for n-SnSe. Filled triangles are for p-Sb$_2$Te$_3$. Asterisks are for n-Bi$_{0.85}$Sb$_{0.15}$ and x-marks are for p-Bi$_{0.85}$Sb$_{0.15}$. Stars are for an n-Bi$_2$Te$_3$ quintuple layer, and diamonds are for p-Bi$_2$Te$_3$ quintuple layer. Pentagons are p-Mg$_3$Sb$_2$ and red dots are p-GeTe. The dashed line is the parabolic band reference assuming $r = 0$.

Equation (3.1) provides a qualitative explanation for the insensitivity of the $zT\left(\hat{E}_F\right)$ vs. $b_L\left(\hat{E}_F\right)$ characteristic to band structure and scattering physics. A transport function that

57

increases S also increases L, which limits the benefit to zT. Conversely, a transport function that reduces L also reduces S, again limiting the benefit to zT. This conjecture is confirmed by Fig. 3.5, which is a plot of $S(\hat{E}_F)$ and $L'(\hat{E}_F)$ vs. $b_L(\hat{E}_F)$ for p-Bi$_2$Te$_3$, p-SnSe, and p-Sb$_2$Te$_3$ (DOS scattering was assumed for these calculations). Figure 3.5 shows that $S(\hat{E}_F)$ and $L'(\hat{E}_F)$ depend on band structure and can be quite different than for a parabolic band. In the range of interest, ($zT(\hat{E}_F) > 2 \Rightarrow b_L(\hat{E}_F) > 0.25$), the three materials shown all display Lorenz numbers that are well below that of the parabolic band reference [26], but this advantage is offset by the fact that they all display lower Seebeck coefficients as well. The trade-off between S' and L' makes it difficult to enhance zT in comparison to a simple, parabolic band.
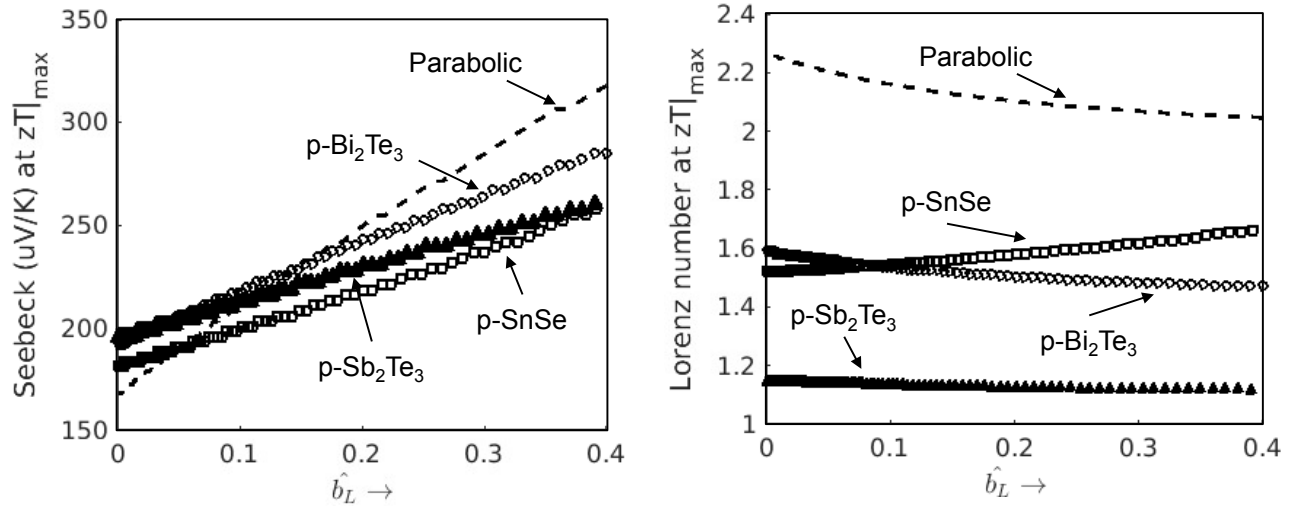
Figure 3.5. Seebeck coefficient and Lorenz number at peak zT vs. $\hat{b}_L$ at 300 K for several different complex thermoelectric materials assuming a scattering rate proportional to the density of states. Open circles are for p-Bi$_2$Te$_3$. Open squares are for p-SnSe and closed triangles are for p-Sb$_2$Te$_3$. The dashed line is the parabolic band reference assuming $r = 0$.

The results of this chapter suggest a different, possibly simpler way to assess the performance of a thermoelectric material. First, one should check to see how it compares at a given b-factor to a parabolic band with ADP scattering. Second, one should assess its potential to achieve a large b-factor. This involves assessing the lattice thermal conductivity and assessing the electrical conductivity, which can be done as follows.

From eqns. (3.4a), (3.4d), and (3.4e), we find

$$\sigma = \frac{2q^2}{h} \int \left[M(E)/A \right] \left[\lambda(E) \right] \left(-\partial f_0 / \partial E \right) dE = q^2 \int \frac{v_x^2(E)\left(-\partial f_0 / \partial E \right)}{K_{el-ph}} dE$$

$$\approx \frac{q^2}{K_{el-ph}} \int v_x^2(E)\left(-\partial f_0 / \partial E \right) dE = \frac{q^2 \left\langle v_x^2(E) \right\rangle}{K_{el-ph}} \qquad\qquad (3.8)$$

where we have assumed that K_{el-ph} varies slowly with energy across the Fermi window. For electrical conductivity, eqn. (3.8) shows only two things matter; that the material has a low electron-phonon coupling parameter and a high velocity squared in the direction of transport. It does not matter whether the high velocity comes from a single valley with a light effective mass, from an anisotropic valley with a light effective mass in the direction of transport, or from multiple valleys with light effective masses in the direction of transport. Of course, all this assumes that the scattering rate follows the density-of-states. Detailed calculations suggest that this is the case, but this question should be examined in more detail. In this approach, assessing the electrical potential of a material is simplified because one only needs to estimate the electron-phonon coupling parameter, K_{el-ph}, and calculate $\left\langle v_x^2(E) \right\rangle$ directly from the band structure. This approach should find use in assessing the potential of a given material, and it might also find application in high throughput computational searches [7], [38-41].

Finally, there has been some interest in defining a general quality factor that is independent of band structure [108]. The generalized b-factor given by (3.3) applies to any band structure, but it includes a dependence on the Fermi level, which is not included in the traditional definition [40], [61], [74], [95]. For parabolic bands,

$$b_L(E_F) \equiv \frac{\sigma(E_F) T}{\kappa_L} \left(k_B / q \right)^2 = B \mathcal{F}_{1/2} \left[\left(E_F - E_C \right) / k_B T \right], \qquad\qquad (3.9)$$

where B is the traditional quality factor [40], [61], [74], [95], and $\mathcal{F}_{1/2}[\eta]$ is the Fermi-Dirac integral as defined by Blakemore [73]. A general quality factor could be defined as [108]

$$b_L'(E_F) \equiv \frac{\sigma(E_F) T \left(k_B / q \right)^2}{\kappa_L \mathcal{F}_{1/2} \left[\left(E_F - E_C \right) / k_B T \right]}. \qquad\qquad (3.10)$$

The general quality factor can be evaluated for any band structure and is expected to be relatively insensitive to the location of the Fermi level. For parabolic energy bands, b'_L reduces to the Fermi level independent *B*-factor.

3.6 Summary

A variety of electronic structures and complex thermoelectric materials were examined in this chapter, and all were shown to produce nearly the same $zT(\hat{E}_F)$ vs. $b_L(\hat{E}_F)$ characteristic as that given by a simple, parabolic band model. The material figure of merit, *zT*, increases without limit as the quality factor increases, but the results of this study suggest that at a given b-factor, there is an upper limit to *zT*. The inherent trade-offs between thermoelectric material parameters explain the apparent universal behavior that was found, but this result is not fundamental. Just as the Wiedemann-Franz Law is not a law of nature, but rather, a rule of thumb that is only rarely violated [109], the same may be true of the universal behavior discovered here. Searches for materials/structures that exceed the parabolic band limit should be conducted, so that new pathways to higher thermoelectric performance can be identified. If no such materials are found, then searches need only focus on materials with large generalized b-factors, i.e. with high electrical conductivity and low lattice thermal conductivity.

Data Availability – The raw and processed data required to reproduce these findings are available free online to download from [https://nanohub.org/groups/needs/lantrap].

4 THE USE OF STRAIN TO TAILOR ELECTRONIC THERMOELECTRIC TRANSPORT PROPERTIES : A FIRST PRINCIPLES STUDY OF 2H-PHASE CuAlO$_2$

4.1 Preface

The contents of this chapter have been extracted from the following publications with permission: E. Witkoske, D. Guzman, Y. Feng, A. Strachan, M. Lundstrom, and N. Lu, "The use of strain to tailor electronic thermoelectric transport properties : A first principles study of 2H-phase CuAlO2," *J. Appl. Phys.*, vol. 125, no. 082531, 2019.

4.2 Introduction

Thermoelectric (TE) devices and materials hold great promise for broad use in solid-state energy generation and solid-state cooling. However, as robust and reliable as these devices are, they have been limited by low conversion efficiencies since their inception [1]–[5]. The past three decades have witnessed the thermoelectric material figure of merit, zT, improved from under one to over two [5]. These gains have been primarily driven by a reduction in the lattice thermal conductivity of materials and devices through the use of nano-structuring [6]–[12] and the development of novel materials that have an inherently low thermal conductivity due to large discrepancies in the masses of their constituent elements. These advances, however, have not translated into working devices [13]. As we approach the lower limit of the lattice thermal conductivity for common and even complex TE materials at room temperature and above, the variety of avenues capable of moving the field of thermoelectrics forward are being narrowed, therefore ideas that have the potential to advance the field need to be explored carefully.

In this chapter we look at an alternate route forward, given materials with relative ease of fabrication, low cost, and non-toxicity, the ability to tailor them to specific temperature ranges, power needs, and size requirements through the use of strain opens an interesting avenue. Even though the overall zT efficiencies of these materials may not be able to beat state of the art TE materials, if the appropriate direction and magnitude of strain could be applied to increase their TE properties, the overall $cost/kW-hr of energy generation quite possibly could.

Because of their potential use in high temperature applications, due to a large band gap, high thermal stability, oxidation resistance, and low material costs, transparent conducting oxides (TCOs) have garnered interest for a variety of TE applications [48]–[51], [110]–[117]. In this work 2H-phase $CuAlO_2$, which has gained interest as a promising candidate for high temperature p-type thermoelectric applications [49], [50], [118], [119] due to the scarcity of p-type TCOs [120], under a variety of uniaxial, biaxial, and hydrostatic strains will be discussed. Limited theoretical and experimental studies have been done on the thermoelectric properties of the 2H phase of this material [49], [120]–[122], and none to our knowledge have been conducted on the effect of strain on its thermoelectric properties. It will be shown that strain can have a significant effect on the band gap and electronic transport properties, in some cases detrimental and in others beneficial for thermoelectrics. This allows for the possibility of tuning the band gap as well as the electronic transport properties of TCOs to tailor them to specific thermoelectric applications [45]–[47].

There are five sections in this chapter; 4.2) introduction, 4.3) atomic structure and methodology, 4.4) electronic structure with and without strain, 4.5) thermoelectric transport properties of strained and unstrained structures, and finally, 4.6) conclusions. We find that strain can offer both opportunities as well as challenges for thermoelectric device design with both the former and the latter being unique to the material and device required for specific applications.

4.3 Atomic structure and methodology

$CuAlO_2$ crystallizes in two distinct phases, 3R and 2H, both having a delafossite structure with the rhombohedral (3R) and hexagonal (2H) phases occurring at atmospheric pressures [123]. In Fig. 4.1(a) the 2H phase structure, with a space group of $P6_3/mmc$ (no. 194), is shown with the crystallographic directions "a, b, and c" which are referred to as the [100], [010], and [001] directions throughout this chapter. Figure 4.1(b) shows the high symmetry k-points of the first Brillouin zone, which are used for plotting the band structures.

All calculations were done using density function theory (DFT) as implemented in the open source package Quantum Espresso [52] to predict the atomic and electronic structure of $CuAlO_2$ under various strain conditions. The ab initio band structures (Kohn-Sham eigenvalues) were

subsequently used to calculate general thermoelectric transport properties by utilizing the open source tool LanTrap 2.0 [79], which solves the Boltzmann Transport equation in the relaxation time approximation using the Landauer formalism [44]. The electron-ion interactions are accounted for using PAW, norm conserving pseudo-potentials; Al.pbe-n-kjpaw_psl.0.1.UPF and Cu.pbe-dn-kjpaw_psl.0.2.UPF, along with the Ultrasoft, norm conserving pseudo-potential O.pbe-n-kjpaw_psl.0.1.UPF from the Quantum ESPRESSO pseudo-potential database. The electron exchange-correlation potential was calculated using the generalized gradient approximation (GGA)[124] within the Perdew-Burke-Ernzerhof (PBE) scheme. The kinetic energy cutoff for the expansion of the plane waves was set to 544.2 eV and all self-consistent calculations were terminated when a tolerance of 1.36×10^{-5} eV in the total energy was reached. The structural relaxations were performed using a conjugate gradient (CG) algorithm and a 10x10x4 k-mesh. All structural relaxations were terminated when the force on all atoms are less than 2.57 meV/angstrom for the unstrained and hydrostatic (equal strain applied in all directions) cases, and 25.7 meV/angstrom for the uniaxial and biaxial strains. The electronic properties were computed on a finer 20x20x12 k-mesh.

a)   b)
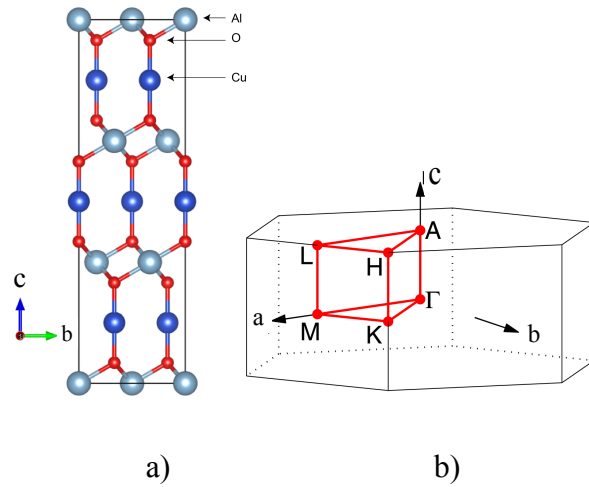
Figure 4.1. Fig. 4.1(a) is the relaxed conventional super cell of 2H-phase $CuAlO_2$. Fig. 4.1(b) is the first Brillouin zone with the high symmetry points used for the dispersion paths shown in Figs. 2-5.

4.4 Electronic structure with and without strain

4.4.1 Relaxed band structure

The lattice constants in the relaxed structure were found to be a = b = 2.855 $\mathring{A}$ and c = 11.394 $\mathring{A}$ which agree well with experimental [125] and theoretical [121], [125] results. Band gap calculations using DFT, a ground state method, generally do not produce reliable results due to the excited-state nature of the band gap, as well as derivative discontinuities in the exchange-correlation energy functional [126], [127] arising when the number of electrons increases by an integer step at the transition between the highest occupied and lowest unoccupied single electron level in an N-electron system [128]. Notably however, the theoretical band gap prediction in the current work as well as from other groups shows remarkable accuracy to experimental results. Our calculations give an unadjusted indirect band gap of 1.85 eV, which is similar to the experimental results of 1.8 eV by Yanagi [129] and 1.65 eV by Benko [130], as well as theoretical values of 1.85 eV by Jayalakshmi [121], 1.82 eV by Liu [131], and 1.7 eV by Yanagi [129]. The detailed explanation for this theoretical accuracy won't be discussed.

Figure 4.2(a) shows the conduction band minimum occurs at the Γ point while the valence band maximums are located at M, K, L, and H, all with similar energies. The valence band of 2H $CuAlO_2$ is built from the hybridization between the oxygen 2p and the aluminum 3s and 3p states in addition to the copper 3d states, which contribute the majority of states at the valence band edge. Copper 4s, aluminum 3s, and aluminum 3p states mainly form the conduction band. The interesting valence band structure at all four valence band maximum points should be noted and will be discussed in Sec. 4.5.

a)   b)
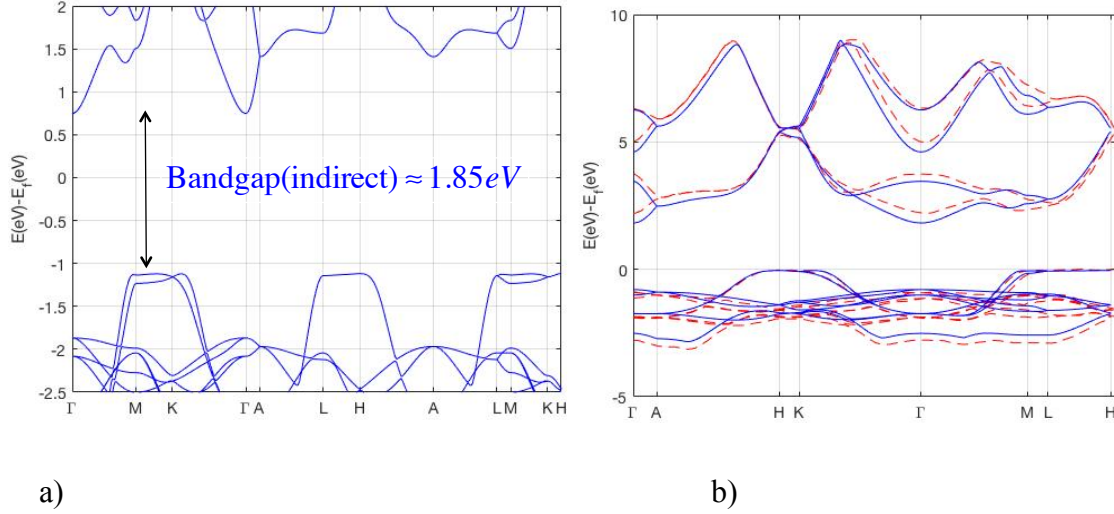
Figure 4.2. Fig. 4.2(a) is the calculated band structure of the 2H phase of CuAlO₂. Fig. 4.2(b) is a comparison of our electronic band structure (solid blue lines) to that of reference [122] (dashed red lines), (note figures 4.2(a) and 4.2(b) use different k-paths). For all band structures in this chapter, the Fermi energy is normalized to zero when calculating band alignment, to allow visual comparisons with a variety of strained and relaxed band structures.

4.4.2   Band structures with hydrostatic strain

DFT calculations are done at 0K, so for materials that are useful at higher temperatures, such as CuAlO₂, once the unstrained structures' band gap is confirmed, adding negative hydrostatic stress can be a useful guide to help find trends in the band gap at these elevated temperatures due to the effects of thermal strain. Imparting confidence in this methodology, the lattice parameters under hydrostatic strain for this study are found to be consistent with theory and experimental values [132], [133].

To simulate hydrostatic strain (equal strains in all directions), we took the relaxed structure and applied isotropic strain to the cell parameters by plus/minus 1,2, and 3%. The atomic positions were then allowed to relax keeping the volume of the cell constant. In all the strained cases shown in Fig. 4.3, most of the difference is a small band gap and electron affinity adjustment. An outlier is the -3% strained case, in which we see a drastic electron affinity adjustment. Most of the shape of the unstrained band structure remains when strain is applied in all six cases studied. The conduction band minimums and valence band maximums remain at the same high symmetry k-points as for the unstrained case. There are some variations in the curvature of the band structure much higher in the conduction band for the 3% compressive and

65

tensile cases. It should be noted that there is very little, if at all, change in the structure of the valence band near the band edge, which is the most relevant area to p-type TE transport properties. A summary of the changes in band gaps can be found in Table 4.1.

a)

b)

c)
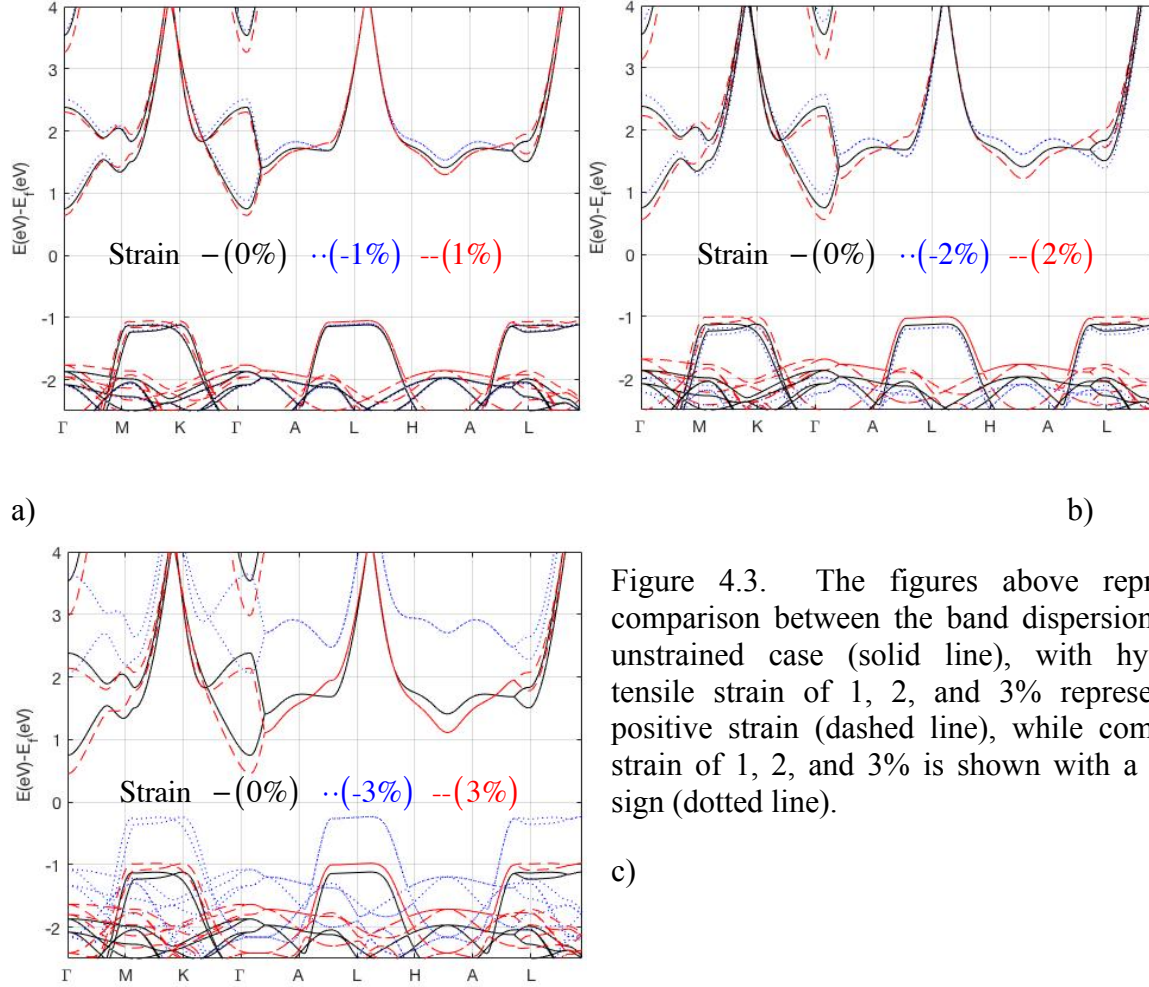
Figure 4.3. The figures above represent a comparison between the band dispersions of the unstrained case (solid line), with hydrostatic tensile strain of 1, 2, and 3% represented by positive strain (dashed line), while compressive strain of 1, 2, and 3% is shown with a negative sign (dotted line).

4.4.3 Uniaxial strain

We applied strain of ± 1% in the [100], [010], or [001] crystallographic direction and allowed the other transverse directions to relax. There are two main observations from the band dispersions in Fig. 4.4. As compared to the unstrained case in Fig. 4.2, the valence and conduction bands have changed substantially in all the structures simulated in Fig. 4.4. The strained structures have lost the flat valence band and have been replaced by a more parabolic band dispersion in four of the six cases (-1% [100], ± 1% [010], and -1% [001]). This will have

66

an effect on electron transport that will be quantified in Sec. 4.5. The second immediate observation is the changes in band gap and band gap minimum locations in the above structures. The band gap has disappeared for the -1% [100] and [001] strains as well as both ±1% [010] cases, and reduced for the 1% [100] and [001] cases. The significant reduction in band gap will hurt thermoelectric performance at high temperatures due to bipolar effects. The conduction band minimum remains around the Γ point, however a second indirect band gap minimum has been reduced in energy and lies at a different high symmetry point for many of the cases in Fig. 4.4.
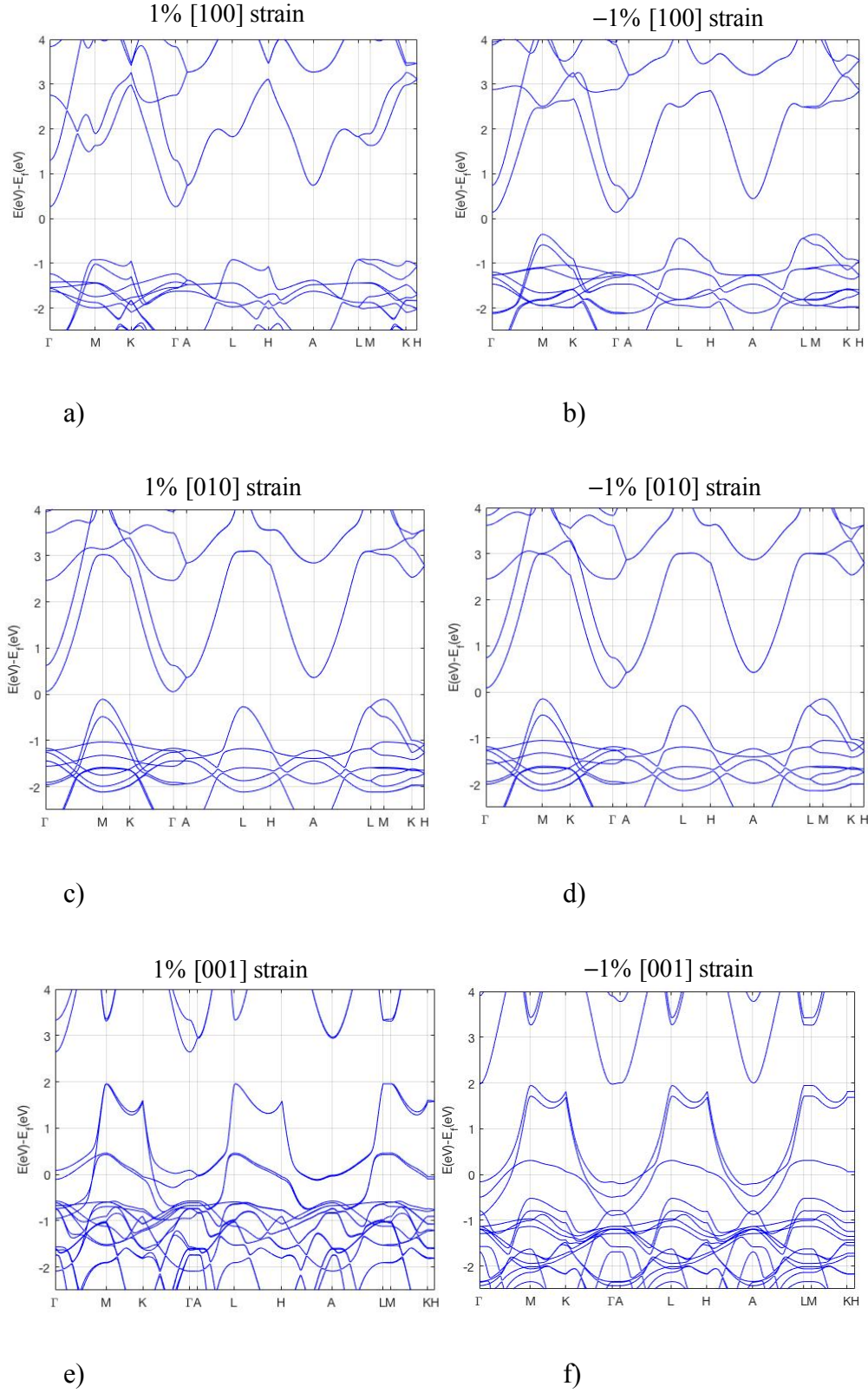
Figure 4.4. The band dispersion relation of 2H-CuAlO$_2$ with ±1% uniaxial strain applied to the [100], [010], and [001] directions respectively, with the other two directions allowed to relax.

4.4.4   Biaxial strain

For biaxial strain the same procedure was used as section C), except we apply $\pm 1\%$ strain to two of the three directions and allowed the third direction to relax. Figure 5 is the band dispersion relation for $\pm 1\%$ strain applied to the [110] direction, as well as the +1% [101] strain case.   For the other structures computed, (i.e. $\pm 1\%$ [011] and -1% [101]), the band gaps disappear entirely and the material becomes metallic for the energy range of interest. With no band gap, the Fermi level lies within the bands, most of the heat is carried by electrons and holes, therefore the overall Seebeck coefficient will be close to zero, due to their combined, offsetting effects. We looked only at structures that retain their semiconducting properties.

1% [110] strain

−1% [110] strain

a)

b)
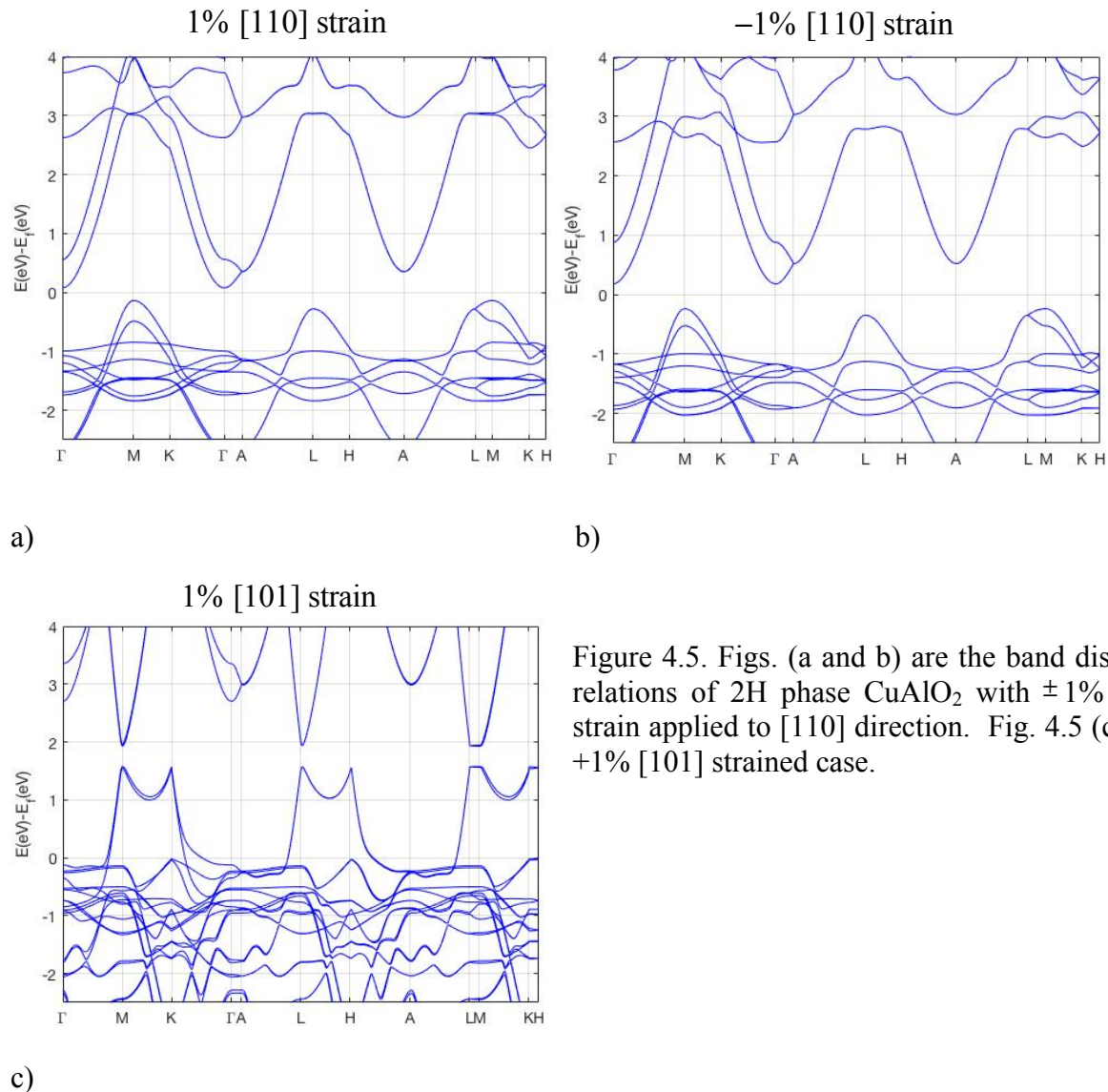
1% [101] strain

Figure 4.5. Figs. (a and b) are the band dispersion relations of 2H phase CuAlO$_2$ with $\pm 1\%$ biaxial strain applied to [110] direction. Fig. 4.5 (c) is the +1% [101] strained case.

c)

The main observations from the band dispersion in Fig. 4.5 are similar to those from the uniaxial strain case in Fig. 4.4. The valence band has changed substantially in structure compared to Figure 4.2(a). The interesting structure of unstrained $CuAlO_2$, having a very flat valence band, has disappeared and been replaced by a more traditional band dispersion in the [110] strain cases. The second immediate observation is that much of the band gap has disappeared for all three cases in Figure 4.5. The +1% [101] strain case has changed from an indirect band gap to direct, while retaining a secondary indirect band gap of similar energy. The valence and conduction bands have become very sharp (i.e. small effective mass) in the +1% [101] strain case. All cases are summarized in Table 4.1 below.

Table 4.1. Summary of the corresponding strain dimension and % applied is followed by the band gap energy. The (I) (indirect) and (D) (direct) is followed by the corresponding symmetry point(s) where the gap minimums in energy occur.

Strain Type		E_{gap} (eV)			2nd E_{gap} (within 0.5 eV of primary E_{gap})		
Unstrained		(I)	1.85	$\Gamma \to M$ & $\Gamma \to L$	None		
Hydrostatic	-3%	(I)	2.33	$\Gamma \to M$ & $\Gamma \to L$	None		
	-2%	(I)	2.16	$\Gamma \to M$ & $\Gamma \to L$			
	-1%	(I)	2.00	$\Gamma \to M$ & $\Gamma \to L$			
	+1%	(I)	1.72	$\Gamma \to M$ & $\Gamma \to L$	None		
	+2%	(I)	1.57	$\Gamma \to M$ & $\Gamma \to L$			
	+1%	(I)	1.44	$\Gamma \to M$ & $\Gamma \to L$			
[110]	-1%	(I)	0.41	$\Gamma \to M$	(I)	0.52	$\Gamma \to L$
	+1%	(I)	0.20	$\Gamma \to M$	(I)	0.34	$\Gamma \to L$
[101]	+1%	(D)	0.35	$M \to L$	(I)	0.38	$M \to K$ & $L \to H$
[100]	-1%	(I)	0.51	$\Gamma \to M$	(I)	0.57	$\Gamma \to L$
	+1%	(I)	1.18	$\Gamma \to M$ & $\Gamma \to K$	(I) 1.65	$A \to L$, $A \to M$, $A \to K$	
[010]	-1%	(I)	0.24	$\Gamma \to M$	(I)	0.39	$\Gamma \to L$
	+1%	(I)	0.16	$\Gamma \to M$	(I)	0.33	$\Gamma \to L$
[001]	-1%	(I)	0.02	$\Gamma \to M$ & $\Gamma \to L$	(I)	0.05	$A \to L$
	+1%	(I)	0.69	$\Gamma \to M$	(I) 1.05 $\Gamma \to K$ (I) 0.97 $L \to M$		

4.5 Thermoelectric Transport

4.5.1 Landauer transport method

The performance of a thermoelectric material is directly related to its material figure of merit,

$$zT = \frac{S^2 \sigma T}{\kappa_L + \kappa_e},$$ (4.1)

where S is the Seebeck coefficient, σ the electrical conductivity, κ_L and κ_e the lattice and electronic thermal conductivities, and T is the temperature. The thermoelectric transport parameters

$$\sigma = \int_{-\infty}^{+\infty} \sigma'(E) dE$$ (4.2a)

$$S = -\frac{1}{qT} \int_{-\infty}^{+\infty} (E - E_F) \sigma'(E) dE \bigg/ \int_{-\infty}^{+\infty} \sigma'(E) dE$$ (4.2b)

$$\kappa_0 = \frac{1}{q^2 T} \int_{-\infty}^{+\infty} (E - E_F)^2 \sigma'(E) dE = \kappa_e + T\sigma S^2$$ (4.2c)

with the differential conductivity, $\sigma'(E)$, given by

$$\sigma'(E) = q^2 \Xi(E) (-\partial f_0 / \partial E),$$ (4.2d)

and the transport distribution in the diffusive limit written in the Landauer form [93],

$$\Xi(E) = \frac{2}{h} (M(E)/A) \lambda(E),$$ (4.2e)

with $M(E)/A$ being the number of channels per cross-sectional area for conduction and $\lambda(E)$ being the mean-free-path (MFP) for backscattering (See the appendix in [102] for a short derivation of (4.2e) and [44] for a longer discussion).

In (4.2e), the mean-free-path for backscattering is defined as [44]

$$\lambda(E) \equiv 2\upsilon_x^2(E)\tau_m(E)/\upsilon_x^+(E), \tag{4.3a}$$

where $\upsilon_x^2(E)$ is an average over angle of the quantity $\upsilon_x^2(\vec{k})$ at energy, E. The velocity, $\upsilon_x^+(E)$, is the angle-averaged velocity in the +x direction (See [44] for the definitions of these averages). The number of channels at energy, E, is [42], [44]

$$M(E)/A = h\upsilon_x^+(E)D(E)/4, \tag{4.3b}$$

where $D(E)$ is the density-of-states per unit volume including a factor of two for spin.

The numerical methods used to calculate eqns. (4.1) and (4.2) in LanTrap [79], using a band structure from density functional theory (DFT) simulations as input, are described in the supplementary information of [102], [103]. In this section we do not consider the variability of the lattice thermal conductivity, κ_L, with strain [47], [132]–[134]. Therefore, if we assume a constant lattice thermal conductivity and a small electronic thermal conductivity, κ_e, due to a relatively low electrical conductivity for oxides, for our purposes in this section, we will focus on the power factor given by

$$PF = S^2\sigma, \tag{4.4}$$

which is comprised of the Seebeck coefficient and the electrical conductivity.

4.5.2   Scattering

When calculating eqns. (4.1), (4.2), and (4.4), a constant mean free path (MFP) of 3 nm for both holes and electrons was used. This is consistent with the small nano-scale size limit (SNS) [58], [59] due to grain boundary scattering [135] of nano-structured TE materials, which has been used to reduce the overall lattice thermal conductivity. Depending on the different strain magnitudes and directions applied, the value of the MFP could vary in magnitude, anisotropy, or both, depending highly on the structure and material growth at the grain boundaries. This was not taken into account in the different strain cases, with a constant MFP of 3 nm always used. In

general, to get a more complete understanding of the scattering mechanisms involved in a particular material or device, experimental mobility should be measured for the structure of interest, or first principles guided simulations performed [102], to help elucidate the type of scattering mechanisms and their coupling strength.

Having assumed a constant mean-free-path of 3 nm, the transport distribution of eq. (4.2e) now depends only on the distribution of modes eqn. (4.3b). This greatly simplifies comparing different band structures to ascertain which will provide the largest PF or zT, the only quantity needed in this case is $M(E)$, which varies proportionally with the density of states. Therefore, in the case of a constant MFP, an increase in the density of states right around the valence band edge will increase the distribution of modes, thereby increasing the power factor. In this case, a large density of states at the valence band edge is very beneficial [75], however if the scattering rate were taken to be acoustic deformation potential (ADP) scattering, which goes inversely with density of states, the benefits aren't always clear [102].

4.5.3   Discussion

Figure 4.6 is a comparison of the transport properties in the [100], [010], and [001] directions of transport for the unstrained case assuming a MFP of 3 nm at 300 K. In all plots the x-axis is the Fermi level with the valence band located at 0 eV and the conduction band located at 1.85 eV. The largest power factor, Fig. 4.6(a), is obtained with transport in the [001] direction in the unstrained structure, this is also true for all strain cases considered next.

Fig. 4.6(b) is a plot of the conductivity vs. Fermi level for the three different transport directions considered. The values of the conductivity show in Fig. 4.6(b) and Table 4.2 at the valence band edge are similar to those reported theoretically using a constant scattering time [122]. However, these conductivity values are approximately 1-2 orders of magnitude larger than what have been reported experimentally [122], [136], [137]. This is attributed to the 1-2 orders of magnitude lower carrier concentrations in experiment, i.e. $\sim 1 \times 10^{18}$ to 1×10^{19} cm^{-3} compared to theoretical carrier concentrations at the power factor maximizing Fermi level around the valence band edge, i.e. $\sim 1 \times 10^{20}$ to 1×10^{21} cm^{-3}.

Fig. 4.6(c) is a plot of the Seebeck coefficient vs. Fermi level. A materials' maximum Seebeck coefficient is not dependent on the overall effective mass directly, but only on band gap and weakly on the scattering mechanism (i.e. Ionized Impurity, Acoustic Deformation Potential Scattering (ADP), constant MFP, etc.). The overall Seebeck vs. Fermi level curve will be unchanged for the three different transport directions considered. The values shown are consistent with other theoretical studies [122] which comes as no surprise since Seebeck values are directly related to the band gap.

Figure 4.6(e) is a plot of the distribution of modes for the three transport directions. The band structure with the largest $M(E)$ at the band edge will also have the largest power factor, which can be seen in Fig. 4.6(a). We notice in Fig. 4.6(e) the dramatically different distribution of modes around the valence and conduction band edges. For parabolic band semiconductors in three dimensions, $M(E)$ varies linearly with energy around the conduction and valence band edges as $M(E) \sim \left| \left(E_{C,V} - E \right) \right|$ [42], [44]. Focusing on the [001] direction, the distribution of modes at the conduction band edge goes linearly with energy as expected. The distribution of modes at the valence band however has a strikingly non-linear shape, leading to the larger power factor values obtain for p-type as compared to n-type carriers in the unstrained case.

We have summarized the power factor, Seebeck coefficient, and electrical conductivity at the Fermi level that maximizes the power factor for all of the strained and unstrained cases in Table 4.2. In all strained and unstrained cases, transport in the [001] direction yields the highest power factor. The Fermi level that maximizes the power factor can vary depending on band structure and scattering, however in all cases discussed in this work, the Fermi level that maximizes the power factor lies very close to the valence band edge, as can be seen from Fig. 4.6(a).
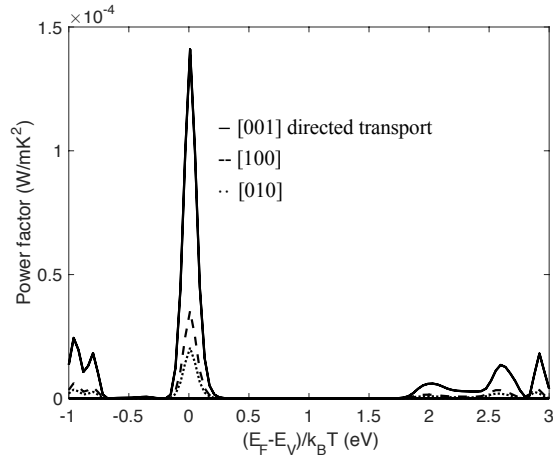
a)
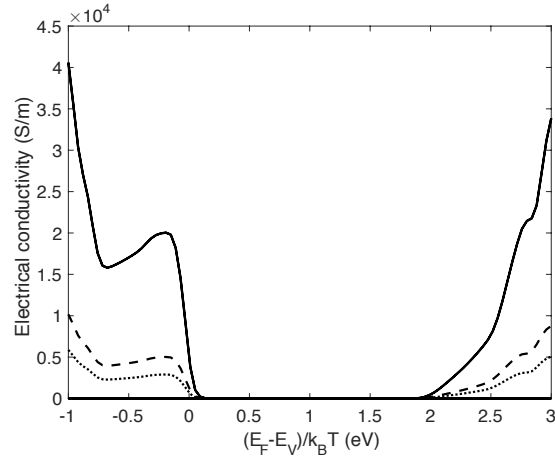
b)
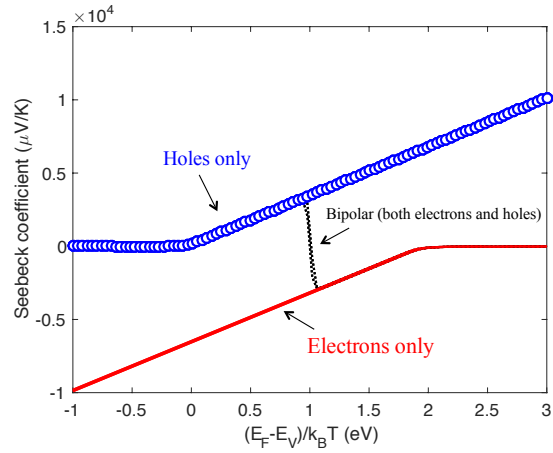
c)
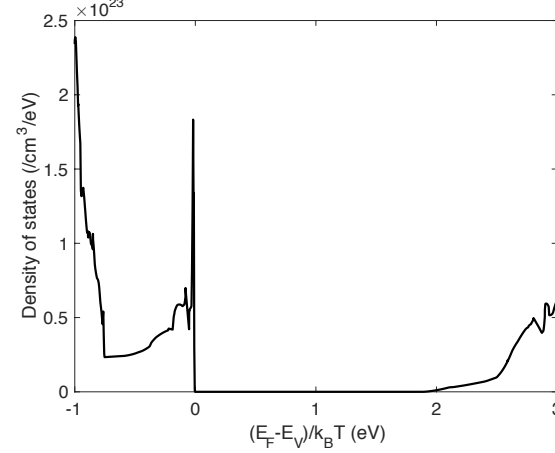
d)
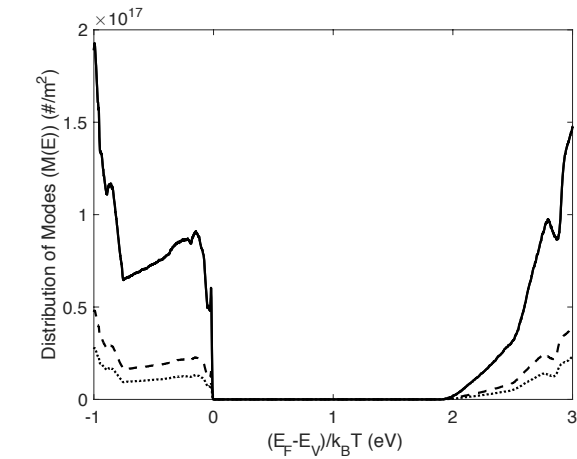
e)

Figure 4.6. The transport properties of the unstrained 2-H phase $CuAlO_2$ in three different transport directions [100](dashed lines), [010](dotted lines), and [001](solid line) assuming a MFP of 3 nm. In all plots the x-axis is the Fermi level with the valence band located at 0 eV and the conduction band located at 1.85 eV. Fig. 4.6(a) is the power factor, fig. 4.6(b) is the electrical conductivity, fig. 4.6(c) is the Seebeck coefficient for electrons, holes, and a combination of the two (same for all transport directions), fig. 4.6(d) is the DOS (same for all transport directions), fig. 4.6(e) is the distribution of modes.

In Table 4.2, the hydrostatic strain cases' power factors closely resemble the unstrained case, which should be expected. When the band gap is adjusted due to hydrostatic pressure, the Seebeck coefficient value at a given energy and k point changes. The Fermi level is adjusted to maximize the power factor, changing the value of the Seebeck coefficient and conductivity at this new Fermi level [102]. Due to these adjustments, the power factors end up being about the same as the unstrained case.

The two cases that raise interest in Table 2 due to their higher power factors are the +1% [101] and the +1% [001] strains. Both have a higher conductivity at the valence band edge than any other cases. The +1% [001] strain yields a p-type power factor of 1.95×10^{-4} (W/mK^2), the highest p-type value of the strains considered. The shape of the valence band for the +1% [101] and +1% [001] strained cases are very similar, with the effective masses becoming very small due to the large curvature of the valence band at the gamma point as can be seen from Figs. 4.4 and 4.5(c). These small effective masses, along with the addition of a second indirect peak at the K and H high symmetry k-points, facilitate a higher distribution of modes, due to the increase of the density of states with the addition of a second band, and a higher positive directed velocity (smaller effective mass), both of which contribute to an increase in $M(E)$. In both of these high power factor cases, n-type conduction has an even higher power factor than p-type. This is due to the same effects described for the increase in p-type conduction. Note the -1% [001] case also has very high conductivity values, however with a negligible band gap, both holes and electrons contribute to the conductivity, making the overall power factor low. Due to the band gaps of 0.35 eV for +1% [101] and 0.69 eV for +1% [001], the power factors for both n and p-types remain high.
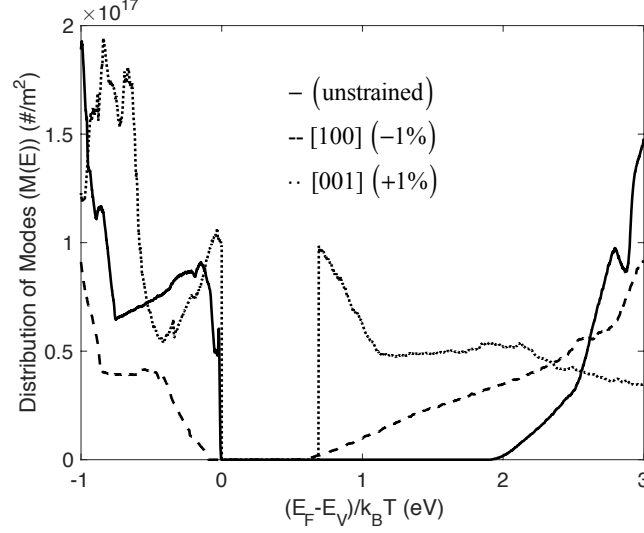
Figure 4.7. Distribution of modes for three cases; the unstrained case (solid line), the -1% [100](dashed line) and the +1% [001](dotted line) strained cases. Because of the constant MFP assumption, $M(E)$ is also the transport distribution, $\Xi(E)$.

Figure 4.7 is a plot of the distribution of modes for three different strained cases; unstrained, -1% [100], and +1% [001], which correspond to our unstrained reference, the lowest, and the highest power factor cases for comparison. As was mentioned before, when the same constant MFP is assumed for all cases, eqns. (4.2d-4.2e) show that only the Fermi window and distribution of modes determine the conductivity. Therefore, the structure with the largest distribution of modes will also have the largest power factor. In Fig. 4.7, the valence band edges of all three cases are shown at 0 eV on the x-axis, but due the strain applied, the conduction band edges lie at 1.85, 0.51, and 0.69 eV respectively. The abrupt n-type distribution of modes for +1% [001] at the conduction band can also be seen in Fig. 4.7. This illustrates the direct correlation between the maximum power factor and the maximum distribution of modes at the band edge.

Table 4.2. Summary of the electrical conductivity, Seebeck coefficient, and power factor at the Fermi level that maximizes the power factor. All calculations were done in LanTrap 2.0 [79] with a MFP of 3 nm with bipolar effects included.

Strain Type		p(n) Electrical conductivity x 10^3 (S/m)(@E_F=$E_{PF(max)}$)	Seebeck Coefficient (μV/K) (@E_F=$E_{PF(max)}$)	Max Power Factor x10^{-4} (W/mK^2) (Optimum transport direction)
Unstrained		3.82	192	1.41
Hydrostatic	-3%	3.36	207	1.44
	-2%	3.55	201	1.43
	-1%	3.73	196	1.43
	+1%	3.90	191	1.42
	+2%	3.94	190	1.42
	+3%	3.92	190	1.41
[110]	-1%	0.75	197	0.29
	+1%	0.95	169	0.27
[101]	+1%	(p) 7.70 (n) 6.81	(p) 145 (n) 161	(p) 1.63 (n) 1.77
[100]	-1%	0.79	142	0.16
	+1%	0.78	168	0.22
[010]	-1%	0.62	213	0.28
	+1%	0.66	210	0.29
[001]	-1%	(p) 10.2 (n) 10.3	(p) 17.1 (n) 13.9	(p) 0.03 (n) 0.02
	+1%	(p) 2.89 (n) 4.75	(p) 260 (n) 206	(p) 1.95 (n) 2.02

4.6 Conclusion

Due to the lack of p-type thermoelectric materials for high temperatures, materials that offer interesting band structure warrant careful consideration. In this work, we used first principles calculations to analyze a promising p-type thermoelectric material that is earth abundant, robust at high temperatures, and oxidation resistant. The drastic change in structure produced when strain is applied creates a type of band dispersion that needs careful analysis to ascertain the benefits and detriments for high temperature (and possibly low temperature) thermoelectrics. All TE transport parameters are determined by the transport function. In the SNS scattering limit assumed in this study (i.e. a constant MFP), the transport function is proportional to the number of channels, $M(E)$. Therefore, the effect of strain on TE transport is best understood by

examining the $M(E)$ extracted from the bandstructure. A large number of channels near the band edge lead to a high electrical conductivity.

The main conclusions of this study are: 1) strain can be beneficial or detrimental to TE performance depending on whether it increases or decreases $M(E)$ near the band edge, and 2) under certain cases of strain, n-type conduction produced higher power factors than their p-type counterparts, thus opening an interesting avenue for strain engineering to produce both n and p type legs from the same material. The enhanced n-type performance occurs because the right type of strain dramatically increases $M(E)$ near the conduction band edge. These results suggest great care must be undergone in the fabrication of this material to prevent detrimental strains, which can lead to degradation of thermoelectric performance. Conversely however, there are also benefits if care is undertaken in fabrication to produce thermoelectric materials that outperform their unstrained cases.

Many researchers feel that thermoelectrics could potentially provide a robust source of energy for a rapidly growing and energy consuming population. Transparent conductive oxide (TCO) materials are attractive because they offer relative ease of fabrication, low cost of materials, and non-toxicity. The ability to tailor TCO materials to specific temperature ranges, power needs, and size requirements, through the use of strain would open up interesting new avenues. Although the overall zT efficiencies of TCO materials may not exceed state of the art TE materials, if the appropriate direction and magnitude of strain could be applied to increase their TE properties, the overall $cost/kW-hr of TCO's quite possibly could.

Data Availability – Access to scripts and the computational tool LanTrap used in this work are be available for free online at nanohub.org/groups/needs/lantrap. The pseudo-potentials used in the DFT calculations can be found at http://www.quantum-espresso.org/pseudopotentials.

5 THE USE OF STRAIN AND GRAIND BOUNDARIES TO TAILOR PHONON TRANSPORT PROPERTIES: A FIRST PRINCIPLES STUDY OF 2H-PHASE CuAlO$_2$ (PART II)

5.1 Preface

The contents of this chapter have been extracted from the following publications with permission: Z. Tong, Y. Feng, X. Ruan, M. Lundstrom, and N. Lu, "The use of strain to tailor phonon transport properties (Part II): A first principles study of 2H-phase CuAlO2," (to be submitted).

Introduction

Thermoelectric (TE) devices and materials are appealing for use in solid-state energy generation and solid-state cooling. Regardless of their operating mode, a good thermoelectric material should have a high electrical conductivity (σ), Seebeck coefficient (S), and a low lattice thermal conductivity (κ$_L$) given in the figure of merit [57]

$$zT = \frac{\sigma S^2 T}{\kappa_L + \kappa_e}.$$

(5.1)

However robust and reliable as TE devices could potentially be, they have been limited by low conversion efficiencies since the beginning [1]–[5]. The gains to zT have been primarily driven by a reduction in the lattice thermal conductivity of materials and devices through the use of nano-structuring [6]–[12] and the development of novel thermoelectric materials with the ability to take advantage of a wide range of operating temperatures [75], [138]–[140] with inherently low thermal conductivity. These advances have not translated into working devices [13] however, due to many issues, one of which being material and fabrication cost. As we approach the lower limit of the lattice thermal conductivity for complex TE materials the applicability of thermoelectric devices remains in question due to their high cost and low efficiencies.

A previous work [141] looked at transparent conducting oxides (TCOs), and specifically 2H-phase $CuAlO_2$, which has gained interest as a promising candidate for high temperature p-type thermoelectric applications [49], [50], [118], [119] [120], because of its potential use in high temperature applications, due to a large band gap, high thermal stability, oxidation resistance, and low material costs [48]–[51], [110]–[117]. Some experimental and theoretical studies [49], [120]–[122], [141], [142], have been done on the thermoelectric (TE) properties of the 2H phase of this material, however none have looked at the thermal conductivity using rigorous first principles simulations. Under specific cases of strain, n-type conduction can produce higher power factors than their p-type counterparts providing an interesting avenue for strain engineering to produce both n and p type legs from the same material [141]. Strain engineering may be beneficial for the electronic component of zT, but its effect on the lattice thermal conductivity must also be ascertained. That is the objective of this work.

In practice, defects are introduced into the lattice itself as point defects or as grains in micro-structured thermoelectric materials to aid in suppressing thermal conductivities. The creation of grain boundaries through the use of nano-structuring is one of the most promising and widely used strategies to improve zT [143]. In this work, a variety of nanometer grains sizes will be simulated, that are consistent with the small nano-scale size limit (SNS) [58], [59], giving rise to grain boundary scattering [135] of nano-structured TE materials. We show in this work an ab initio assessment of lattice thermal conductivity in 2H $CuAlO_2$, including third-order anharmonic scattering, natural isotopic scattering, and Casimir finite-sized boundary scattering, which takes into account the spectral decomposition of phonon wave vectors at the grain boundary. We find that the low thermal conductivity seen experimentally [144], [145] is most likely due to micro and nano-structured effects due to grain boundary scattering of phonons. Casimir grain boundary scattering reduces the thermal conductivity by as much an order of magnitude, with crystalline anisotropy (due to the hexagonal structure) further reducing κ_L. Isotopic scattering has a limited effect (especially for small grain sizes) due to the constituent atoms being on the smaller end of the periodic table, (typically isotopic scattering plays a larger role when large mass atoms are involved or at low temperatures [146]).

In this work under a variety of strains are applied and their effects on the lattice thermal conductivity will be discussed, as well as the variations of the lattice thermal conductivity for a wide range of temperatures. There are five sections in this paper, I) introduction, II) methodology and simulation details, III) unstrained lattice thermal conductivity, IV) strained lattice thermal conductivity and finally, V) conclusions.

5.2 Methodology and Simulation details

5.2.1 Atomic structure

CuAlO$_2$ crystallizes in two distinct phases, 3R and 2H, both having a delafossite structure with the rhombohedral (3R) and hexagonal (2H) phases occurring at atmospheric pressures [123]. In Fig. 5.1(a), the 2H phase structure, with a space group of P6$_3$/mmc (no. 194), is shown with the crystallographic directions "x, y, and z". Figure 5.1(b) shows the high symmetry k-points of the first Brillouin zone, which are used for plotting the phonon band structures.

a)   b)
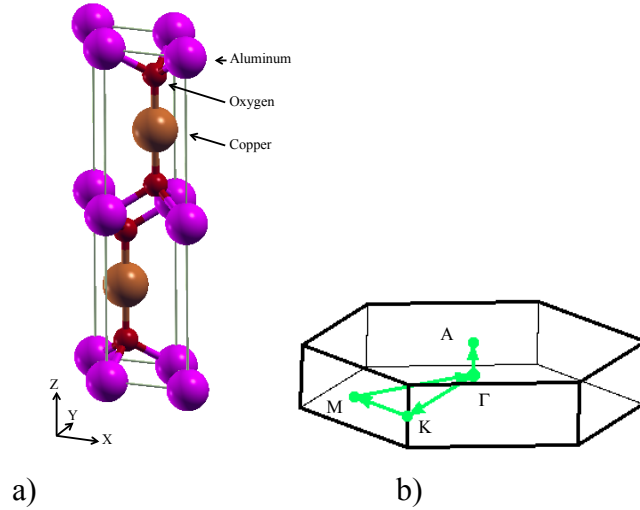
Figure 5.1 (a) Relaxed conventional supercell of 2H-phase CuAlO$_2$. (b) First Brillouin zone with the high symmetry points used for the dispersion paths shown in Fig. 5.2.

A phonon can be defined as a quantum of lattice vibrations, described by the quantum number $\lambda = (v, \mathbf{q})$, where v denotes the branch index and $\mathbf{q}$ denotes the wave vector of a particular phonon mode. A phonon can be scattered through interaction with other phonons, electrons, impurities, grains, etc. The overall scattering rate of a phonon mode can be estimated by

Matthiessen's rule [147] as $\Gamma_\lambda = \Gamma_\lambda^{pp} + \Gamma_\lambda^{pe} + \Gamma_\lambda^{gb} + \Gamma_\lambda^{im}...$ that includes phonon-phonon (p-p) scattering, phonon-electron (p-e) scattering, grain boundary (gb) scattering, phonon-impurity (isotopic) scattering, respectively. Due to the low electrical conductivity as noted in [51], [141], [144], the phonon-electron scattering term, Γ_λ^{pe}, is neglected here. Isotopic scattering was included in some simulations, however the results show that the effect is negligible, especially when grain sizes are small. Only Γ_λ^{pp}, and Γ_λ^{gb} will be calculated from first principles in this work.

The current calculation includes three-phonon scattering only, while four-phonon scattering was shown to be important for certain materials [148], [149]. Further studies of this material warrant the inclusion of four-phonon processes since present applications of $CuAlO_2$ are for high temperatures, where four-phonon scattering can be relevant [150]. The p-p scattering contribution from three-phonon processes to Γ_λ^{pp} is given by Fermi's golden rule as [151], [152] ,

$$
\begin{aligned}
\Gamma_\lambda^{pp} &= \frac{\hbar\pi}{4N} \sum_{\lambda_1\lambda_2}^{+} \frac{2(n_1 - n_2)}{\omega\omega_1\omega_2} \left|V_{\lambda\lambda_1\lambda_2}^{+}\right|^2 \delta(\omega + \omega_1 - \omega_2) \\
&+ \frac{\hbar\pi}{8N} \sum_{\lambda_1\lambda_2}^{+} \frac{(n_1 + n_2 + 1)}{\omega\omega_1\omega_2} \left|V_{\lambda\lambda_1\lambda_2}^{-}\right|^2 \delta(\omega - \omega_1 - \omega_2),
\end{aligned}
\tag{5.2}
$$

where the first term is the combination of two phonons with possibly different wave vectors to produce one phonon. The second term is for the opposite process of one phonon splitting into two, i.e. phonon emission, with $\hbar$ being Planck's constant, n_i is the Bose-Einstein distribution, and ω is the phonon frequency. The summation runs over all phonon modes and wave vectors and requires conservation of the quasi-momentum $q_2 = q \pm q_1 + Q$ in which Q is the reciprocal lattice vector with Q = 0 constituting a normal process and $Q \neq 0$ being an Umklapp processes. N is the number of discrete q-points of the Γ-centered q-grid for sampling, δ is the Dirac delta function, which is approximated by a Gaussian function in the computational package QUANTUM ESPRESSO (QE) [52], [55] (which is the computational package used in this work). The scattering matrix elements $V_{\lambda\lambda_1\lambda_2}^{\pm}$ [54], [55], [151] are given by,

$$V_{\lambda\lambda_1\lambda_2}^{\pm} = \sum_{l_1}^{N_B} \sum_{l_2,l_3}^{N,N} \sum_{\eta_1\eta_2\eta_3}^{3,3,3} \frac{\partial^3 E}{\partial r_{l_1}^{\eta_1} \partial r_{l_2}^{\eta_2} \partial r_{l_3}^{\eta_3}} \frac{e_\lambda^{\eta_1}(l_1) e_{j_1,\pm q_1}^{\eta_2}(l_2) e_{j_2,-q_2}^{\eta_3}(l_3)}{\sqrt{m_{l_1} m_{l_2} m_{l_3}}},$$ (5.3)

where m_{li} is the atomic mass and $e_{v,q}$ is a normalized eigenvector of the mode $\lambda = (v, \mathbf{q})$. In eq. (5.3) l_1, l_3, and l_3 run over all atomic indices (with l_3 only summing over the atoms in the center unit cell, which contains N_B basis atoms), and η_1, η_2, and η_3 represent Cartesian coordinates. The 3$^{\text{rd}}$ order anharmonic interatomic force constants (IFCs) are the third-order partial derivatives, which are obtained from the D3Q-Thermal2 package interfaced to QE [54], [55]. The energy E is the total energy of the entire system with $r_{l_1}^{\eta_1}$ designating the η_1 component of the displacement of a particular atom l_1. We also obtain the second order force constants by Fourier transforming dynamical matrices in the reciprocal momentum space gleaned from linear response theory implemented in QE [55].

The lattice thermal conductivity tensor can then be calculated as

$$\kappa_{L,\alpha\beta} = \sum_\lambda \frac{1}{k_B T^2} (\hbar\omega_\lambda)^2 n_\lambda (n_\lambda + 1) \upsilon_{\lambda,\alpha} \upsilon_{\lambda,\beta} \tau_\lambda,$$ (5.4)

$$\frac{1}{\tau_\lambda} = \frac{1}{\tau_{\lambda,pp}} + \frac{1}{\tau_{\lambda,gb}},$$ (5.5)

with Matthiessen's rule being applied to the scattering lifetimes of individual phonon modes separately [153].

5.2.2   Grain boundaries

The phase or polytype transition of this material from the trigonal 3R to the hexagonal 2H phase can happen at 15.4 Gpa [142], with the 3R phase being studied more due to its better structural stability. It has been shown elsewhere that treating grain boundaries as a secondary phase of a material can help explain much of the transport behavior observed in polycrystalline samples [154]. At grain/phase boundaries that are comparable to grain size, a significant amount of heat is transported through the interface by phonons [154], therefore studying the high

pressure 2H phase of $CuAlO_2$ can help elucidate phonon transport in nano-grained structures of the 3R phase as well.

The grain boundary scattering term is the only term that depends on the direction of the phonon group velocity explicitly, which can generally be expressed as the frequency independent equation [155],

$$\tau_{\lambda,gb} = \frac{L_\eta}{2|v_{\lambda,\eta}|},$$
(5.6)

where L_η is the distance between the two boundaries in one of three Cartesian directions. However due to the omnidirectional grains and the variety of temperature ranges used, a model from [156] is assumed in this study, which assumes a grain boundary acts as a diffraction grating, producing diffraction spectra of various orders. Multiple values of L_η are used in this work and are shown in Section III. In all calculations, including Casimir scattering, we assume the correction factor [55] [157], [158] to be F =1, which takes into account the shape and roughness of each grain boundary to be diffusive.

It has been shown in previous work the commonly used frequency-independent boundary scattering (grey model or the simple Casimir model, not to be confused with the Casimir model used in this work [156]) can better fit thermal conductivity experimental data if it is replaced by a frequency-dependent phonon scattering model due to dislocation strain in grain boundaries [159]. This difference manifests itself most notably at low temperatures with the frequency-independent boundary scattering going as the normal $\sim T^3$ Debye law, which deviates from experimental thermal conductivity of polycrystalline silicon which goes as $\sim T^2$ at low temperatures [160]. In this work however, the temperature range of interest is primarily > 300K, thus these discrepancies are not considered here, and will be left for future work on this material and its experimental low temperature thermal conductivity behavior.

5.2.3 Simulation details

The thermal conductivity, q–dependent linewidths, including Casimir and natural isotopic-disorder scattering, are calculated using the D3Q-Thermal2 codes [54], [55]. We use a generalized-gradient approximation (GGA) Perdew-Burke-Ernzerhof (PBE) scheme [124] for electron-electron interaction, and ONCV norm-conserving pseudopotentials [161] for the electron-ion interaction. GGA considers the gradient of the charge density at each position when the atom position is perturbed, and has been shown to work better for materials with abrupt charge density changes such as in semiconductors, whereas the Local Density Approximation (LDA) is more applicable to metallic systems [162].

The plane-wave energy cut-offs and force thresholds for the variety of strain and unstrained cases were varied based on finding well-relaxed structures with the absence of negative phonon frequencies and are provided in the supplementary material (SM). The hexagonal symmetry was enforced during the geometry optimization. Strained structures were relaxed after artificially changing the lattice constant in a particular direction of strain. The k–point grids used for structural relaxation and optimization were 16 x 16 x 16 while the q-point grids for phonon dynamical-matrix calculations were set to 4 x 4 x 4. For the third-order force constants a grid of 2 x 2 x 2 was used, and a 10 x 10 x 10 grid was used for the lattice thermal conductivity calculation. In calculating the lattice thermal conductivity, a Gaussian smearing of 5 cm^{-1} was used. This value, along with tests on k/q-grids, and energy cut-offs, have been checked w.r.t the phonon frequencies at the Γ point and suggest that the average lattice thermal conductivity value is stable to within ten percent.

5.2.4 Anisotropy and Convergence

In this work, due to the "mis"-orientation of grains in experimental samples [144], the uncertainty in the heat and electronic directed transport intended, the bulk nature of the intended material, and the "relative" isotropy in the lattice thermal conductivity tensor, the lattice thermal conductivity is assumed to be $\kappa_L = \sum_{i=1}^{3} \kappa_i / 3$, i.e. an average over the x, y, and z directions. For the lattice thermal conductivity calculation, the "exact" iterative conjugate-gradient solution (CGS) method of [55] which attempts to solve the linearized BTE exactly, was compared to the single mode relaxation time approximation (SMRTA) [55], [163]–[166]. The SMRTA is considered to

be inadequate to describe thermal conductivity at low temperature ranges, with increased sensitivity to isotopic scattering at these low temperatures[151], [167] i.e. T < 300 K. However for our purposes here, the temperature range of interest are generally greater than 300 K, even though results will be shown for temperatures less than this, the SMRTA gives results above 300 K for the average thermal conductivity "consistent" with the CGS, please see the supplementary material for a discussion of this. For structures with no grain scattering assumed, the lattice thermal conductivity for the x and y directions are consistent within 1-5% for the SMRTA compared to the CGS for all temperatures considered. However, the lattice thermal conductivity for the z direction shows a large deviation for T > 300 K for the SMRTA compared to the CGS, with the SMRTA model underestimating the z directed lattice thermal conductivity by around 40-50% for these temperatures. Even with this large deviation, the average lattice thermal conductivity found by averaging the x, y, and z directions deviates only around 10% from the SMRTA to the CGS for T > 300 K. Due to the considerations mentioned at the beginning of this section, and, as we will see later, that deviations are significantly reduced when small grain boundaries are introduced into the structures, the average thermal conductivity using the SMRTA is used throughout this work.

5.3 Unstrained Lattice Thermal conductivity

The lattice constants in the hexagonal relaxed structure were found to be a = b = $2.8798\,\mathring{A}$ and c = $11.4077\,\mathring{A}$, which agree well with experimental [125] and theoretical [121], [125] results.
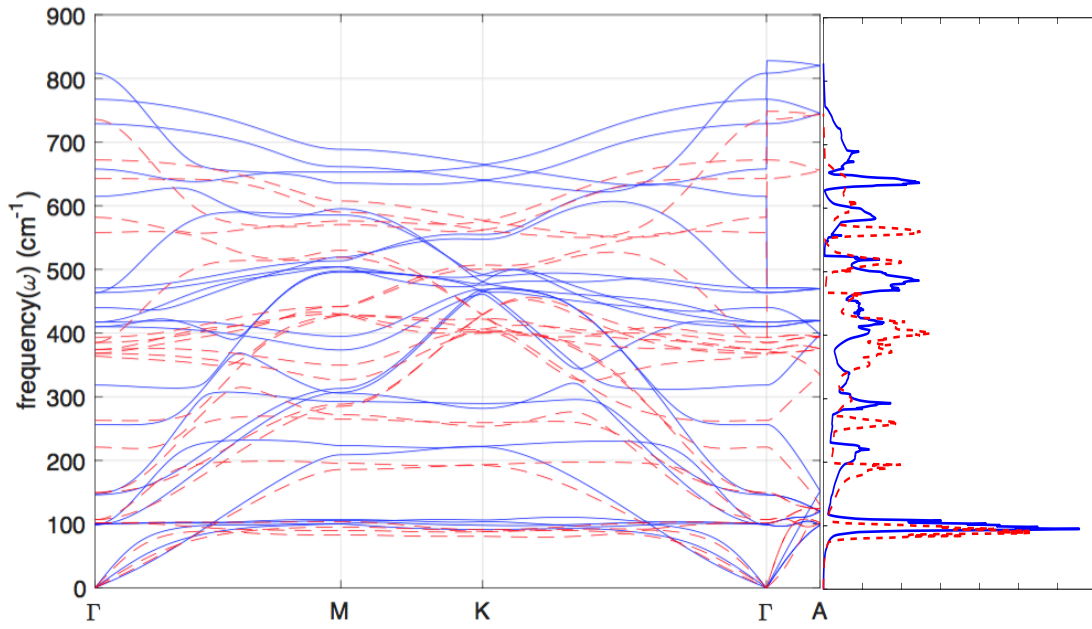
Figure 5.2 Calculated phonon dispersion relation and density of states of the 2H phase of CuAlO$_2$ for unstrained (solid blue) and +3% strain (dotted red).

Figure 5.2 shows the phonon band dispersion for 2H CuAlO$_2$ for the unstrained structure (and +3% strain for comparison) used throughout this section. With the hexagonal structure of this material, one notices the large amount of bands especially around the low frequency of 100 cm^{-1}. Boundary or grain scattering generally scatter low frequency phonons, as opposed to Umklapp and point defect mechanisms which scatter at all frequencies and high frequencies respectively [159]. We will see that these low frequency modes in 2H CuAlO$_2$ get effectively scattered when grain boundaries are introduced.
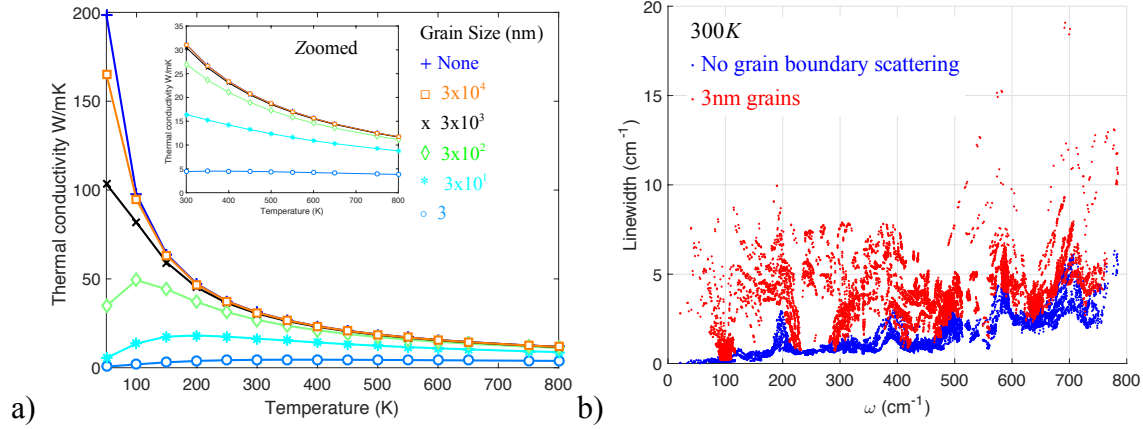
Figure 5.3 (a) Comparison between the thermal conductivity of the material without grains, along with grain sizes of 3nm, 30nm, 300nm, 3000nm, and 30000nm vs. temperature. (b) Scattering linewidth vs. frequency for the structure with no grains (blue dots) and the structure with grains of 3nm (red dots).

The structures in Fig. 5.3(a) show a $\sim T^{-1}$ behavior above the Debye temperature, consistent with the Dulong-Petit law, with the thermal conductivity being governed by the MFP in this region. With the finite size of the crystal being accounted for, κ_L becomes finite at zero K and decreases for grains larger than 3000nm as temperature increases. However, for structures with grains of 300nm and less, the lattice thermal conductivity begins to increase from 0K before then decreasing around the Debye temperature, and continuing to do so at higher temperatures. As was mentioned earlier, the difference between the $\sim T^3$ Debye law for low temperature phonons due to boundary scattering with the dislocation strain model, $\sim T^2$, won't be resolved in this work.

This can be interpreted as a dominating effect of the grain boundaries over intrinsic phonon scattering [168] (i.e. the intrinsic mean free path, $l_{mfp} = \bar{v}\tau_\lambda$ is very large at low temperatures and is limited by the crystal size). The same (albeit difficult to see) effect can be observed in Fig. 5.3(b) at 300 K. Even though the linewidths have greater values for some of the higher frequency modes, the lower frequency linewidths for the 3nm grain case are consistently larger in comparison to the no grain structure (blue dots) at these low frequencies compared to the discrepancy between the two structures for higher frequencies. These low frequency bands are generally affected more by Casimir scattering, with both anharmonic and Casimir scattering

89

being significant along the shearing transverse-acoustic mode around 100 cm^{-1}, as can be seen in Fig. 5.1 around the Γ point.

This same effect can be seen in the accumulation functions [165] in Fig. 5.4(a) (no grains) and Fig. 5.4(b) (3nm grains) as well with lower temperatures being governed by larger MFPs for both the structure without grains Fig. 5.4(a) and for 3nm grains Fig. 5.4(b).
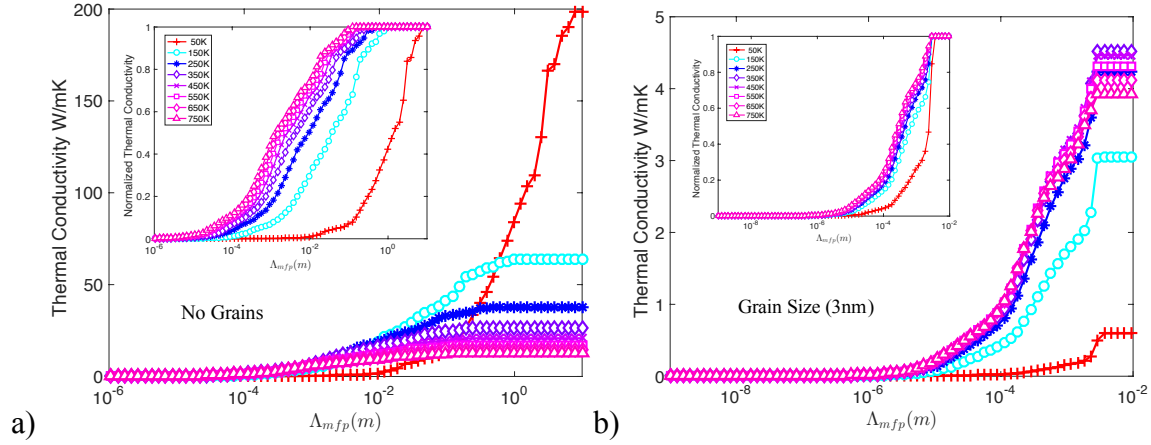
Figure 5.4 (a) The accumulation function of the thermal conductivity for a structure with no grains for a variety of temperatures. The inset is the thermal conductivity normalized to 1. (b)The same set of plots but for a structure that includes 3nm grains. Please note the different values on the x-axis.

In comparing with experiment at 300 K, values of the total thermal conductivity agree well with reported values for "micro" grained structures [145] of 20-30 W/mK, with our results 25-32 W/mK being reasonable. For "nano" structured samples in [145], around 2 W/mK was found compared to our results of 4.4 W/mK . If isotopic scattering is included with natural isotopes assumed, our thermal conductivity is only reduced to around 3.8 W/mK, making the isotopic scattering contribution negligible. Further results were obtained from [144] with thermal conductivities found to be around 2.5 W/mK at 300K. The grain size observed in [144] was experimentally found to be 0.247 nm. Though not included in the above figures, a grain size of 0.3nm in our simulations gives a thermal conductivity of around 0.5 W/mK at 300 K. The trend seen in Fig. 5.3(a) however for the 3nm structure is consistent with the thermal conductivity seen in [144], which is relatively constant over a large temperature range from 300K-800K.

5.4 Lattice Thermal Conductivity with Strain

5.4.1 Hydrostatic strain

To simulate hydrostatic strain (equal strains in all directions), we took the relaxed structure and applied isotropic strain to the cell parameters by ± 1, ± 2, and $\pm 3\%$. The atomic positions were then allowed to relax keeping the volume of the cell constant. Imparting confidence in this particular methodology, the lattice parameters under these hydrostatic strains are found to be consistent with theory and experimental values [132], [133].

Figure 5(a) is a plot of the thermal conductivity vs. strain for both a structure without grains (blue circles) and for one with 3 nm grains (red stars). We can see from Fig. 5(b) that the +3% strained structure without grains has a much higher scattering linewidth, with values being shifted lower in frequency, and conversely for the -3% strain, the linewidths are lower and shifted higher in frequency. We remind the reader that -3% constitutes compressive strain.
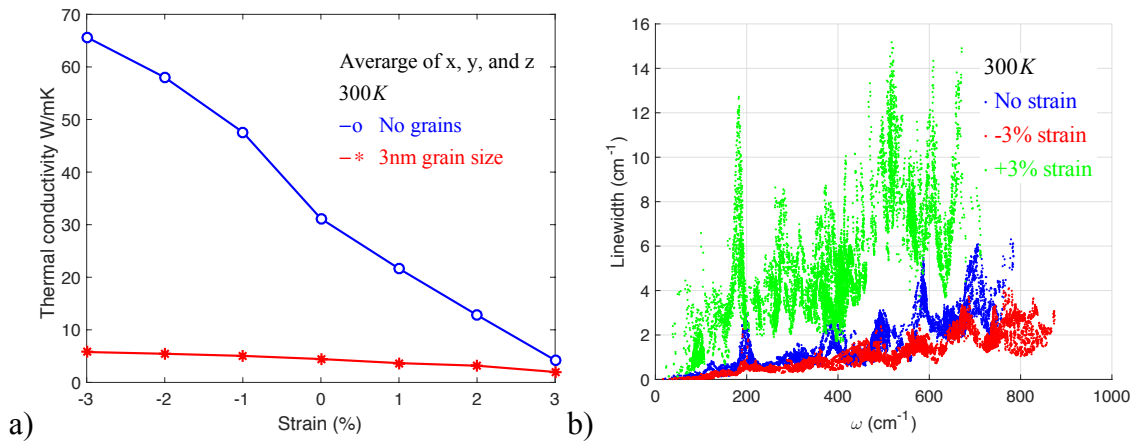
Figure 5.5 (a) Lattice thermal conductivity vs. strain for both a structure without grains (blue circles) and for one with 3 nm grains (red stars). (b) Linewidth vs. frequency for structures with no grains with the unstrained case as blue dots, -3% strain shown as red dots, and +3% shown with green dots.

Figure 5.5(b) explains Fig. 5.5(a), with the large linewidths corresponding to a shorter lifetime, yielding κ_L for a structure with no grains with +3% strain comparable to that of a structure with 3nm grains at +3% strain (4 W/mK compared to 2 W/mK). The κ_L at +3% strain without grains at 300K is about 4 W/mK compared to the unstrained case at 300 K of 32 W/mK. The reduction in lattice thermal conductivity in Fig. 5.5(a) from the -3% strained to the

unstrained case of 55% is conversely consistent with the reduction of the average linewidth in Fig. 5.5(b) of ~ 50% from the unstrained to -3% case. The same effect is seen from the unstrained to +3% strain cases, with the lattice thermal conductivity reduced by 86% in Fig. 5.5(b), with the average linewidth being reduced by around ~ 70% from the +3% to unstrained case. Even though these trends aren't exactly one to one, the connection to scattering is clear. The trend vs. strain is consistent with compressive strain shifting the phonons to higher frequencies with bands becoming more spread out in energy inducing longer scattering times, giving higher thermal conductivities. The +3% strained phonon energy dispersion bands are lower than the unstrained case and closer together, as seen in Fig. 5.2, therefore, the lower frequency induces stronger phonon-phonon scattering (predominately among high frequency optical phonons) in the strained case, as seen in Fig 5.5(b). Structures with 3nm grains are also reduced by the inclusion of strain, varying from around 6 W/mK to 2 W/mK in a similar manner.

What is more interesting is the trend observed in Figs. 5.6(a) and 5.6(b). Figure 5.6(a) is a plot of κ_L vs. strain for a wide range of temperatures. The thermal conductivity in Fig. 5.6(a) decreases from -3% to +3% just as before, as does κ_L for the temperature trend, i.e. the lowest temperature has the highest κ_L and progressively downward with values converging to less than 20 W/mK for all temperature cases. Fig. 5.6(b), which is a plot of κ_L vs. strain for a structure with 3nm grains, has the lowest thermal conductivity for the lowest temperature curve 50 K. However, the trend is not entirely flipped; the highest κ_L is not the highest temperature at -3% strain, but a mid range temperature of around 450 K. Further more at +3% strain the curves begin to cross with the highest κ_L around 2 W/mK for 300 K and the lowest still being 50 K at 0.5 W/mK, with the highest temperature of 800 K occupying the second lowest value of slightly over 1 W/mK.
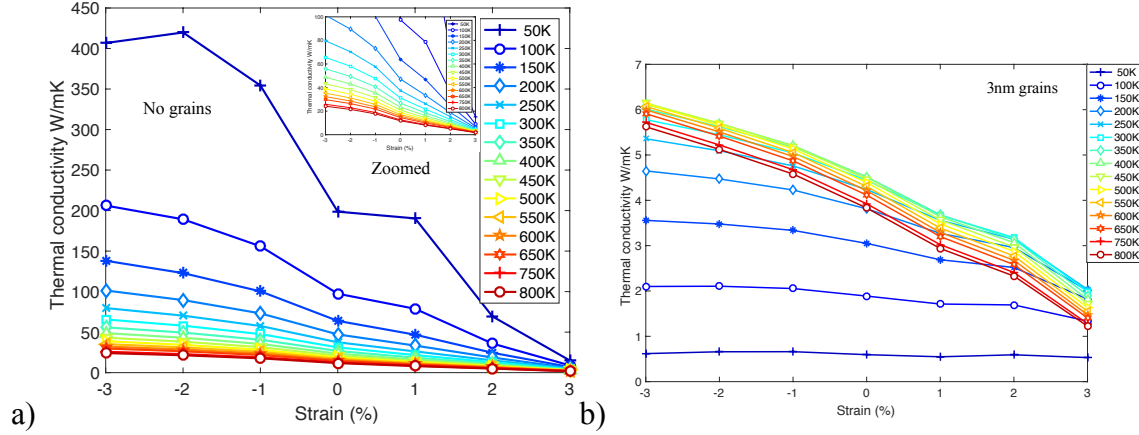
Figure 5.6 The figures above show plots of the thermal conductivity vs. hydrostatic tensile strain ranging from -3% to 3% with a variety of temperatures with symbols in the figures; (a) is without grains in the structure, and (b) has 3nm grains included. Both plots have the same symbols for each temperature case. The inset in (a) is zoomed to thermal conductivities from 0 to 100 W/mK.

As was mentioned before in the methods section, the SMRTA is generally less accurate for lower temperature ranges up to 300 K, with a general reduction in κ_L for this method compared to the conjugate-gradient solution (CGS) method [55]. Neglecting the low temperatures, we see that for temperatures from around 300 K and above, the κ_L values are grouped closer together in both figures, more noticeably in Fig. 5.6(b) ranging from around 5.5-6 W/mK for -3% strain, to around 2 W/mK for +3% strain. These trends suggest that nano-structured $CuAlO_2$ with small grain sizes of around a nanometer are temperature independent regardless of the strain applied, also seen in Fig. 5.3(a), further clarifying the constant temperature curve of the experimental data in [144] and [145].

5.4.2   Selected uni-axial strain

In part I of this study [141], it was found that +1% strain in the z direction induced the highest power factors for both n and p type transport in $2H$-$CuAlO_2$. A structure with +1% strain in the z direction was simulated for both a crystalline (no grains) as well as for a structure with 3nm grains. The crystalline structure and polycrystalline 3nm grain structure had identical temperature trends to that observed in figure 3(a) for the same cases. As far as lattice thermal conductivity is concerned, for this material it is generally unnecessary to resolve uni- or bi-axial strain, since the 3nm grains will dominate the scattering and the results are the same as above.

93

The large reduction in lattice thermal conductivity due to 1 – 3% hydrostatic strain seen in Fig. 5.5(a) above is consistent with first principles work in other materials [169]. The inclusion of only uni-directional strain has a much smaller effect of 1 – 10% on the overall lattice thermal conductivity, and many times not at all.

5.5 Conclusions

In summary, we believe that the lattice thermal conductivity and therefore the total thermal conductivity of 2H $CuAlO_2$, due to the limited electronic thermal conductivity, is not unnaturally small because of its inherent structure, but rather because of the inclusion of grain-boundary scattering. While the crystalline thermal conductivity is around 32 W/(K-m) at room temperature, it drops to between 5-15 W/(K-m) for typical experimental grain sizes from 3nm to 30nm at room temperature. A second conclusion of this study shows that when grains of 3nm or less are assumed, the thermal conductivity is generally independent of temperature for unstrained, compressive, or expansive strained structures. Due to the array of possible strain and phase transitions inherent in grain boundaries, these results confirm similar experimental studies that show limited temperature dependence for κ_L regardless of the fabrication technique used. In the particular case of +3% strain on a crystalline sample, the lattice thermal conductivity is similar to that of samples with 3nm grains. However, due to difficulties in fabrication and the omnidirectional nature of grains in most experimental samples of this material, it will be more practical to decrease the lattice thermal conductivity through the inclusion of these grains, than by straining crystalline samples.

In conjunction with previous studies of 2H $CuAlO_2$, there is a possibility for use of this low cost and non-toxic transparent conducting oxide (TCO) as a TE generator for both high and room temperature applications by fabricating polycrystalline structures with nano-scale features. Although the electrical conductivity of this material is rather low, and the overall zT efficiencies may not exceed state of the art TE materials, the $cost/kW-hr quite possibly could.

Data Availability – The pseudo-potentials used in the DFT calculations can be found at http://www.quantum-espresso.org/pseudopotentials.

6 CONCLUSIONS AND FUTURE WORK

6.1 Conclusions and Summary

In summary, this thesis contained two distinct parts, with chapters 2 and 3 setting the stage by addressing the question: What makes a good thermoelectric material from an electronic perspective? In chapter 2 we began by understanding band convergence and scattering with approximations such as the constant relaxation time (CRTA) and the constant mean-free-path approximations. We found that these assumptions are not always suitable for understanding the performance potential of a complex thermoelectric material with multiple valleys and bands. Chapter 3 analyzed a variety of electronic structures and complex thermoelectric materials, and all were shown to produce nearly the same $zT\left(\hat{E}_F\right)$ vs. $b_L\left(\hat{E}_F\right)$ characteristic as that given by a simple, parabolic band model. The results of this chapter suggest that at a given b-factor, there is an upper limit to the figure of merit, zT. However, zT increases without limit as the b-factor increases, showing that the b-factor, which is the ratio of electrical conductivity to lattice thermal conductivity, is the relevant quantity when trying to understand the TE potential of a material.

We then switched gears in chapters 4 and 5 to examine the thermoelectric potential of 2H-CuAlO$_2$. In chapter 4, we used first principles calculations to analyze the electronic TE components of 2H-CuAlO$_2$, revealing that when strain is applied, careful analysis is needed to ascertain the benefits, i.e., potential for both higher n and p type power factors than the unstrained case, and detriments, i.e. lower power factors, depending on the type of strain applied. We also showed in the SNS scattering limit (i.e. a constant MFP), the transport function is proportional to the number of channels, $M\left(E\right)$, revealing that TE transport is best understood by examining the $M\left(E\right)$ extracted from the band structure. Finally in chapter 5, to complete the picture, the strain and grain boundary effects on the lattice thermal conductivity of 2H-CuAlO$_2$ were investigated using first principles calculations. While the crystalline thermal conductivity is around 32 W/(K-m) at room temperature, it drops to between 5-15 W/(K-m) for typical experimental grain sizes from 3nm to 30nm at room temperature. A second conclusion of this study shows that when grains of 3nm or less are assumed, the thermal conductivity is generally independent of temperature for unstrained, compressive, or expansive strained structures. In the

particular case of +3% strain on a crystalline sample, the lattice thermal conductivity is similar to that of samples with 3nm grains. However, due to difficulties in fabrication and the omnidirectional nature of grains in most experimental samples of this material, it will be more practical to decrease the lattice thermal conductivity through the inclusion of these grains, rather than by straining crystalline samples.

The overall theoretical zT of 2H-CuAlO$_2$ found by combining values from chapters 4 & 5 could potentially be ~ 0.03 at 300 K and ~ 0.08 at 800 K. This small zT is predominately due to the low electrical conductivity of this material. However, the general cost of each constituent element of CuAlO$_2$ (~0.5$/kg) when compared to SiGe (~500$/kg), which is a commonly used commercial TE material, is dramatically different. Even if these material costs aren't one-to-one for the fabrication processes, the advantage of lower cost materials can potentially lead to lower $/kW-hr devices. The possibility of "breakthrough" zT values to facilitate efficient TEGs appears to be a difficult proposition. An alternative strategy to maximize the $/kW-hr for specific applications has hope to implement TEGs in practical and needed situations.

6.2 Opportunities for Thermoelectrics

6.2.1 Application-driven TE Research

Despite recent advances in TE materials research, there have been limited, if any, demonstrations of materials or devices with figure of merit values greater than one for commercial use. The best opportunity for TE materials lies in specific niche applications by co-development of new devices and systems. The first step is to analyze what are the goals and the particular TE engineering applications needed. Instead of looking for novel, expensive materials with high zTs first, one should look at what other attributes are absolutely essential to the particular application, i.e. high emissivity, low water solubility, thermal expansion, magnetic properties, ability to fabricate contacts, low cost, high/low lattice thermal conductivity, etc. Then we should ask the question, are there semiconductor materials that can be doped accordingly, that have these particular attributes? As we saw in chapter 3, any parabolic band semiconductor could potentially be used as a TEG. When potential applications are found, Bi$_2$Te$_3$ has generally been the one size fits all material for devices since the 1960s when discussing cost and feasibility. However as we've explained here, perhaps application should drive the material

search, and not the other way around, with the end goal of reducing the cost of the entire system, not just the TE device.

As we discussed in the introductory chapter, there are different metrics for understanding the benefits of thermoelectrics in different situations. In the follow sections I will discuss two potential applications that require different approaches to optimizing $/kW-hr to benefit devices and systems as well.

6.2.2   High Temperature Environments for Powering Sensors

In this first example we look at a situation where TEGs may help alleviate some incurred costs of maintenance in deep underwater sensors. Energy companies as well as civil engineering firms are in need of cheap ways to power sensors on underwater oil/gas/steam pipes that are deep enough underwater that changing the batteries to these sensors is costly and difficult. Beginning this analysis we ask ourselves a few questions: How do we keep the cold side cold? Can we engineer away a large lattice thermal conductivity for a material? What contact materials should be used? What kind of insulating materials should be used, etc? But before we ask any of these questions, it is important to understand which material figures of merit best apply to this particular situation.

In the introductory chapter two figures of merit were derived. If we maximize the efficiency of a TE material with a given fixed heat flux, we saw that zT is the relevant quantity. However, in the second optimization, one with respect to total power delivered to a load with a fixed device design or cost, you want the highest power output. It is shown in [41] that when operating between two fixed temperature reservoirs, the power output attained can be higher for higher lattice thermal conductivities. In reality, the contacts and device will have a finite thermal capacitance, however the trend of increasing power output with lattice thermal conductivity still holds [41]. The question then becomes, can the temperature gradient, or constant thermal reservoirs be maintained? The specific TEG environment with possible temperature differentials of 500-1000 Celsius for this particular application will be a deciding factor in the overall importance of whether this approach is applicable in our underwater pipe example. If an environment naturally provides an "infinite" heat sink and source, the thermal conductivity of the device will be much less relevant and can possibly increase total power output if increased.

However if a temperature gradient is difficult to establish, the importance of the efficiency, zT, and consequently the lattice thermal conductivity, of the device increases [51].

6.2.3 Concentrated Solar Power Energy Dissipation and Power Production

We now take a look at a situation that is generally not regarded as an opportunity for TEGs. Concentrated solar thermal power (CSP) farms used to generate electricity are a renewable energy source that use mirrors and absorptive collectors to focus solar radiation which drives a heat engine through the use of a steam turbine, thermochemical reaction, supercritical carbon dioxide, or molten salts. The temperature differential is then used to drive an electrical power generator [170] in a conventional power cycle, such as Rankine (stem engine), Brayton (gas turbine engine) or Stirling engine [171]. Overall system conversion efficiencies of around 35% for these large systems are currently feasible with state of the art thermal management [171]. (Other groups have proposed devices that use concentrated direct sunlight to heat one side of a TEG, but these systems are on much smaller scales for personal or individual uses, with their conversion efficiencies reaching only around 10% in theory [172] and most likely much less in practice).

Here we will look at an application for TEGs in CSP systems from a different vantage point. A variety of cooling mechanisms, water cooled, air cooled, and other non-conventional methods are suggested for the cold side heat sink that generally require electrical power to keep cool or by using radiating fins to maintain a temperature differential [28], [29], [172], [173]. Could a TEG lower the cost of a passive cooling system? The main purpose in this part of the CSP system is to remove heat from the system as quickly as possible. Here, the generation of power is secondary, with the first priority being heat dissipation. Once again we ask, which material figures of merit best apply to this particular situation? So the question is, can we design semiconductor materials that have very high thermal conductivities capable of moving and dissipating heat quickly to heat sinks, but at the same time generate power (with the type of heat sink needing to be co-optimized as well [28], [174])? If a particular design and material can be fabricated, the total cost of the design will be the total cost of materials and fabrication, minus the extra electricity generated. Current operational costs include the use of electricity. If semiconductor materials with high power factors and high thermal conductivities as well can be designed, passive cooling might be

augmented with power generation to reduce the overall LCOE for a variety of power generating systems.

6.2.4 Thermoelectrics Moving Forward

Future studies may elucidate avenues to achieve zT values that outperform simple parabolic bands, from quantum spin heat transport phenomenon [175] to heat transport in superconductors [176], but until these potential breakthroughs reveal themselves, the particular attributes of TEs; small and compact, solid state, long-lasting, have the potential to be exploited [36], [177]. Whether it be for cooling or power generation, TEs can still play important roles in a variety of practical applications, which by no means have been exhausted.

APPENDIX A

A.1 Preface

The contents of this chapter have been extracted from the following publications with permission: E. Witkoske, X. Wang, M. Lundstrom, V. Askarpour, and J. Maassen, "Thermoelectric band engineering: The role of carrier scattering," *J. Appl. Phys.*, vol. 122, no. 175102, 2017.

A.2 Derivation

This appendix presents a short derivation of the Landauer form of the transport distribution, (2.8g). Just one of the diagonal components will be derived here. Beginning with (2.8f) and assuming an energy-dependent scattering time, we find

$$\Xi_{xx}(E) \equiv \sum_{\vec{k}} \upsilon_x^2 \tau(E) \delta(E - E_k),$$
(A1)

which can be written as

$$\Xi_{xx}(E) \equiv \frac{\sum_{\vec{k}} \upsilon_x^2 \tau(E) \delta(E - E_k)}{\sum_{\vec{k}} |\upsilon_x| \delta(E - E_k)} \times \frac{\sum_{\vec{k}} |\upsilon_x| \delta(E - E_k)}{\sum_{\vec{k}} \delta(E - E_k)} \times \frac{\sum_{\vec{k}} \delta(E - E_k)}{\Omega},$$
(A2)

where Ω is a normalization volume. The third factor in (A2) is recognized as the density of states,

$$D(E) \equiv \frac{1}{\Omega} \sum_{\vec{k}} \delta(E - E_k).$$
(A3)

The second factor in (A2) can be recognized as the angle-averaged velocity in the direction of transport,

$$\langle |v_x| \rangle \equiv \frac{\sum_k |v_x| \delta(E - E_k)}{\sum_k \delta(E - E_k)} \qquad . \tag{A4}$$

The first term can be written as

$$\frac{\sum_k v_x^2 \tau(E) \delta(E - E_k)}{\sum_k |v_x| \delta(E - E_k)} = \frac{\sum_k v_x^2 \tau(E) \delta(E - E_k)}{\sum_k \delta(E - E_k)} \times \frac{\sum_k \delta(E - E_k)}{\sum_k |v_x| \delta(E - E_k)}$$

$$= \frac{\langle v_x^2 \tau_m \rangle}{\langle |v_x| \rangle} = \frac{\lambda(E)}{2} \tag{A5}$$

(see (2.9) in the text). Using (A3) – (A5) in (A2), we find

$$\Xi_{xx}(E) = \lambda(E) \frac{\langle |v_x| \rangle D(E)}{2} . \tag{A6}$$

Finally, using the definition for the number of channels per cross-sectional area [42], [44],

$$M(E) / A \equiv \frac{h}{4} \langle |v_x| \rangle D(E),$$

(A6) becomes

$$\Xi_{xx}(E) = \frac{2}{h} \lambda(E) M(E) / A . \tag{A7}$$

Equation (A1.7) expresses the transport distribution in terms of two physically clear factors, the mean-free-path for backscattering and the number of channels per cross-sectional area. The concept of channels is a seminal one in nanoscale transport, where $M(E)$ is a small countable number and leads to quantized conduction . We use it here at a larger scale where $M(E) / A$ is large. Note also that the transport function is closely related to the transmission in the Landauer approach to transport [178].

APPENDIX B

B.1 Preface

The contents of this chapter have been extracted from the following publications with permission: E. Witkoske, X. Wang, M. Lundstrom, V. Askarpour, and J. Maassen, "Thermoelectric band engineering: The role of carrier scattering," *J. Appl. Phys.*, vol. 122, no. 175102, 2017.

B.2 Derivation of the Anisotropic Velocity Ratio, Distribution of Modes, and Density of States for spherical and ellipsoidal energy surfaces.

We are looking to calculate the quantity,

$$\tilde{v}(E) = \frac{\langle v_z^2 \rangle}{\langle v_z^+ \rangle}, \tag{B1}$$

where the brackets denote an average over angle at energy, E.

For spherical energy bands, $v(E)$ is isotropic and

$$\langle |v_z| \rangle = \frac{v(E)}{2} \quad \text{(in 3D).} \tag{B2}$$

also

$$v_x^2 + v_y^2 + v_z^2 = v^2(E) = 3v_z^2$$

so

$$\langle v_z^2 \rangle = \langle v^2/3 \rangle = \frac{1}{3}v^2(E)$$

so we get:

$$\tilde{v}(E) = \frac{\langle v_z^2 \rangle}{\langle v_z^+ \rangle} = \frac{v^2/3}{v/2} = \frac{2}{3}v(E) \tag{B3}$$

What is the answer for ellipsoidal bands?

The above derivation was quick and dirty – let's do it more formally, but let's start with parabolic energy bands for which we know the correct answer.

$$\langle v_z^+ \rangle = \frac{\frac{1}{\Omega} \sum_{\vec{k}, k_z > 0} v_z^+ \delta(E - E_k)}{\frac{1}{\Omega} \sum_{\vec{k}, k_z > 0} \delta(E - E_k)} \tag{B4a}$$

$$\langle v_z^2 \rangle = \frac{\frac{1}{\Omega} \sum_{\vec{k}, k_z > 0} v_z^2 \delta(E - E_k)}{\frac{1}{\Omega} \sum_{\vec{k}, k_z > 0} \delta(E - E_k)} \tag{B4b}$$

We immediately recognize the denominators as the DOS divided by 2 – since we are only summing over positive k_z – one-half of the k-states,

$$D(E) = \frac{m^* \sqrt{2m^* E}}{2\pi^2 \hbar^3} \ . \tag{B5}$$

Let's work out the numerator of (B4).

$$NUM = \frac{1}{\Omega} \sum_{\vec{k}, k_z > 0} v_z^+ \delta(E - E_k) = \frac{1}{4\pi^3} \int_0^{2\pi} d\phi \int_0^{\pi/2} \sin\theta \, d\theta \int_0^\infty \frac{\hbar k \cos\theta}{m^*} k^2 \, dk \delta(E - E_k)$$

$$NUM = \frac{1}{4\pi^3} \times 2\pi \times \left.\frac{\sin^2\theta}{2}\right|_0^{\pi/2} \int_0^\infty \frac{\hbar k}{m^*} k^2 \, dk \delta(E - E_k)$$

$$NUM = \frac{\hbar}{4\pi^2 m^*} \int_0^\infty k^3 \, dk \delta(E - E_k) \tag{B6}$$

$$\frac{\hbar^2 k^2}{2m^*} = E \qquad k = \frac{\sqrt{2m^* E}}{\hbar} \qquad k^3 = \frac{(2m^* E)^{3/2}}{\hbar^3} \qquad\qquad dk = \frac{\sqrt{2m^*}}{2\hbar} E^{-1/2} dE$$

$$k^3 dk = \frac{2(m^*)^2}{\hbar^4} E dE$$

From (B6):

$$NUM = \frac{\hbar}{4\pi^2 m^*} \int_0^\infty k^3 \, dk \delta(E - E_k) = \frac{\hbar}{4\pi^2 m^*} \int_0^\infty \frac{2(m^*)^2}{\hbar^4} E \, dE \, \delta(E - E_k) = \frac{m^*}{2\pi^2 \hbar^3} E$$

Finally, return to (B4):

$$\langle \upsilon_z^+ \rangle = \frac{\dfrac{1}{\Omega} \sum_{\vec{k}, k_z > 0} \upsilon_z^+ \delta(E - E_k)}{\dfrac{1}{\Omega} \sum_{\vec{k}, k_z > 0} \delta(E - E_k)} = \frac{\dfrac{1}{\Omega} \sum_{\vec{k}, k_z > 0} \upsilon_z^+ \delta(E - E_k)}{D(E)/2} = \frac{\dfrac{m^*}{2\pi^2 \hbar^3} E}{\dfrac{m^* \sqrt{2m^* E}}{2\pi^2 \hbar^3}} = \sqrt{\frac{E}{2m^*}} \tag{B7}$$

For parabolic energy bands

$$\upsilon(E) = \sqrt{\frac{2E}{m^*}} \tag{B8}$$

So (B7) is

$$\left\langle v_z^+ \right\rangle = \frac{1}{2} v(E) \tag{B9}$$

This is the correct result – see [42].

Next, let's see if we can do this calculations for ellipsoidal energy bands

We know the correct answer, because Jeong [44] has worked it out. Begin with

$$M(E)/A \equiv \frac{h}{4} \left\langle v_z^+ (E) \right\rangle D(E) \tag{B10}$$

$$D(E) = \frac{m_{DOS}^* \sqrt{2 m_{DOS}^* E}}{\pi^2 \hbar^3} \tag{B11}$$

$$m_{DOS}^* = 6^{2/3} \left(m_\ell^* m_t^{*2} \right)^{1/3} \tag{B12}$$

We also know from Jeong [44]:

$$M(E) \big/ A = \frac{m_{DOM}^*}{2\pi\hbar^2} E \tag{B13}$$

$$m_{DOM}^* = 2m_t^* + 4\sqrt{m_t^* m_\ell^*} \tag{B14}$$

From (B10) we find:

$$\left\langle v_z^+ (E) \right\rangle = \frac{4}{h} \frac{M(E)/A}{D(E)} = \frac{4}{h} \frac{m_{DOM}^* E / 2\pi\hbar^2}{m_{DOS}^* \sqrt{2 m_{DOS}^* E} \big/ \pi^2 \hbar^3} = \frac{m_{DOM}^* E}{\sqrt{2 m_{DOS}^* E}} = \frac{m_{DOM}^*}{\left(m_{DOS}^* \right)^{3/2}} \sqrt{\frac{E}{2}}$$

or

$$\left\langle v_z^+ (E) \right\rangle = \sqrt{\frac{E}{2}} \left(\frac{2}{6\sqrt{m_\ell^*}} + \frac{4}{6\sqrt{m_t^*}} \right) \tag{B15}$$

This almost looks intuitive – but there seems to be a factor of 1/2. Normally angle averaging introduces a factor of ½, i.e. eq. (B9); let's see if we can verify this by directly evaluating (B4) for ellipsoidal bands.

We will first do the calculation to get the density of states for ellipsoidal bands as a check, since we know the Density of states for these types of bands is

$$D(E) = \frac{\sqrt{m_t^{*2} m_\ell^* (2E)}}{\pi^2 \hbar^3} \tag{B16}$$

$$DEN = \frac{1}{\Omega} \sum_{\vec{k}, k_z > 0} \delta(E - E_k)$$

In Spherical coordinates our Energy dispersion takes the form:

$$\frac{\hbar^2 k_x^2}{2m_t^*} + \frac{\hbar^2 k_y^2}{2m_t^*} + \frac{\hbar^2 k_z^2}{2m_\ell^*} = E \qquad \frac{\hbar^2 k^2 \cos^2\phi \sin^2\theta}{2m_t^*} + \frac{\hbar^2 k^2 \sin^2\phi \sin^2\theta}{2m_t^*} + \frac{\hbar^2 k^2 \cos^2\theta}{2m_\ell^*} = E$$

$$k^2 = \frac{2E}{\dfrac{\hbar^2 \sin^2\theta}{m_t^*} + \dfrac{\hbar^2 \cos^2\theta}{m_\ell^*}} \qquad k^2 dk = \frac{1}{\hbar^3} \sqrt{\frac{2E}{\left(\dfrac{\sin^2\theta}{m_t^*} + \dfrac{\cos^2\theta}{m_\ell^*}\right)^{3/2}}} dE$$

$$DEN = \frac{1}{\Omega} \sum_{\vec{k}, k_z > 0} \delta(E - E_k) = \frac{1}{4\pi^3} \int_0^{2\pi} \int_0^{\pi} \int_0^{\infty} \sin\theta \, k^2 \, dk \, \delta(E - E_k) d\theta d\phi \tag{B17}$$

$$DEN = \frac{1}{4\pi^3} \int_0^{2\pi} \int_0^{\pi} \int_0^{\infty} \sin\theta \, \frac{1}{\hbar^3} \sqrt{\frac{2E}{\left(\dfrac{\sin^2\theta}{m_t^*} + \dfrac{\cos^2\theta}{m_\ell^*}\right)^3}} \, dE \, \delta(E - E_k) d\theta d\phi$$

$$DEN = \frac{1}{2\pi^2\hbar^3} \int\limits_0^\infty \sqrt{2E} \, dE \delta\left(E - E_k\right) \int\limits_0^\pi \sin\theta \sqrt{\frac{1}{\left(\frac{\sin^2\theta}{m_t^*} + \frac{\cos^2\theta}{m_\ell^*}\right)^3}} \, d\theta$$

with $x = \cos\theta$

$$DEN = \frac{\sqrt{2E}}{2\pi^2\hbar^3} \int\limits_{-1}^{1} \frac{1}{\left(\frac{\left(1-x^2\right)}{m_t^*} + \frac{x^2}{m_\ell^*}\right)^{3/2}} \, dx = \frac{\sqrt{2E\left(m_t^{*2} m_\ell^*\right)}}{\pi^2\hbar^3}$$

If we multiply the above equation by 6 we get the overall Density of States.

Let us now calculate equation (B4a) and (B4b) for any ellipsoidal Energy Surface.

To be able to compute the integrals in Spherical coordinates, we must make some coordinate transformations that allow us to perform the integrations. For the density of states calculation, the integrals worked out without any transformations. For certain functions however, the integrals become very complicated and conceptually difficult to compute.

We start once again with the energy dispersion relation for a general Ellipsoidal surface.

$$\frac{\hbar^2 k_x^2}{2m_x^*} + \frac{\hbar^2 k_y^2}{2m_y^*} + \frac{\hbar^2 k_z^2}{2m_z^*} = E \tag{B19}$$

The integral we are looking for is

$$NUM = \frac{1}{\Omega} \sum_{\vec{k}, k_z > 0} \upsilon_z^+ \delta\left(E - E_k\right) = \frac{1}{4\pi^3} \int\limits_{\vec{k}, k_z > 0} \upsilon_z^+ \delta\left(E - E_k\right) d^3\vec{k} \tag{B20}$$

Let's transform equation (B19) using,

$$k_i = \sqrt{\frac{m_i}{M}} q_i \; ; \quad q^2 = q_x^2 + q_y^2 + q_z^2 \tag{B21}$$

applying this to equation (B19) yields,

$$E = \frac{\hbar^2 q^2}{2M} \tag{B22}$$

The velocity is equal to,

$$\vec{v} = \hbar \left(\frac{k_x}{m_x}, \frac{k_y}{m_y}, \frac{k_z}{m_z} \right) \tag{B23}$$

Plugging in the appropriate substitutions for k_z and d^3k into equation (B20) yields

$$\frac{1}{4\pi^3} \int\limits_{\vec{k}, k_z > 0} v_z^+ \delta\left(E - E_k\right) d^3\vec{k} = \frac{\hbar}{4\pi^3} \sqrt{\frac{m_x m_y}{M^4}} \int\limits_{k_z > 0} \int\limits_{k_y} \int\limits_{k_x} q_z \delta\left(E - E_q\right) d^3\vec{q} \tag{B24}$$

Using,

$$q\cos\theta = q_z$$

and switching to spherical coordinates gives,

$$NUM = \frac{1}{4\pi^3} \sqrt{\frac{m_x m_y}{M^4}} \int\limits_0^{2\pi} \int\limits_0^{\pi/2} \int\limits_0^{\infty} q^3 \cos\theta \sin\theta \, \delta\left(E - E_q\right) d\theta d\phi dq \tag{B25}$$

Finally, using equation (B22) with Energy substitutions for q and dq, the integral in (B25) is easily evaluated,

$$NUM = \frac{1}{2\pi^2 \hbar^3} \sqrt{\frac{m_x m_y}{1}} \frac{2E}{2} \tag{B26}$$

We see that the numerator of Equation (B4) only depends on the two transverse effective masses, not on the transport direction effective mass.

To complete the calculation of Equation (B4) we use equation (B16) for a generic ellipsoidal band, (not forgetting the factor of ½ to account for only half of the k_z states)

$$D(E) = \frac{\sqrt{m_x m_y m_z (2E)}}{2\pi^2 \hbar^3} \tag{B27}$$

then dividing equation (B26) by equation (B27) gives,

$$\frac{1}{2} \sqrt{\frac{2E}{m_z}} \; . \tag{B28}$$

To reproduce equation (B15) in silicon, we use equation (B26) along with the fact that the effective masses in x and y are equal. In silicon there are two ellipsoids with their transport direction in the z direction. There are 2 with their long axis pointed in the x direction, and 2 with their long axis pointed in the y direction.

$$NUM = 2 \times \frac{2E \sqrt{m_t m_t}}{4\pi^2 \hbar^3} + 2 \times \frac{2E \sqrt{m_t m_\ell}}{4\pi^2 \hbar^3} + 2 \times \frac{2E \sqrt{m_\ell m_t}}{4\pi^2 \hbar^3} = \left(2m_t + 4\sqrt{m_\ell m_t} \right) \frac{2E}{4\pi^2 \hbar^3} \tag{B29}$$

Dividing (B29) by (B27, with a 6 included for the total number of valleys) gives,

$$\langle v_z^+(E) \rangle = \frac{1}{2} \sqrt{\frac{2E}{1}} \left(\frac{2}{6\sqrt{m_\ell^*}} + \frac{4}{6\sqrt{m_t^*}} \right) \tag{B30}$$

This is what we would expect by looking at equation (B9). The angle averaging in three dimensions includes an additional factor of ½. Before we move on to finishing equation (B1), let's verify equation (B10) since we have all the pieces, i.e. eqns. (B10, B16, B30).

$$M(E)/A = \frac{h}{4}\frac{1}{2}\sqrt{\frac{2E}{1}}\left(\frac{2}{6\sqrt{m_\ell^*}}+\frac{4}{6\sqrt{m_t^*}}\right)\frac{6\sqrt{m_t^{*2}m_\ell^*(2E)}}{\pi^2\hbar^3} = \frac{\left(2m_t^*+4\sqrt{m_t^*m_\ell^*}\right)}{2\pi\hbar^2}E \tag{B31}$$

This final result matches the result from [44].

Our overall goal however was to calculate equation (B1). We have found the denominator of this equation, to calculate the numerator the same procedure of equations (B19) through (B26) is followed with a few small adjustments.

$$NUM = \frac{1}{\Omega}\sum_{\vec{k},k_z>0}v_z^2\delta(E-E_k) = \frac{1}{4\pi^3}\int_{\vec{k},k_z>0}v_z^2\delta(E-E_k)d^3\vec{k} \tag{B32}$$

Same procedure as above gives,

$$NUM = \frac{1}{4\pi^3}\sqrt{\frac{m_xm_ym_z}{M^3}}\int_{k_z>0}\int_{k_y}\int_{k_x}q_z^2\delta(E-E_q)d^3\vec{q}$$

$$NUM = \frac{1}{4\pi^3}\sqrt{\frac{m_xm_ym_z}{M^5}}\int_0^{2\pi}\int_0^{\pi/2}\int_0^\infty q^4\cos^2\theta\sin\theta\,\delta(E-E_q)d\theta d\phi dq$$

Converting q and dq to Energy using equation (B22) and computing the integrals, we arrive at the desired result.

$$NUM = \frac{1}{2\pi^2\hbar^3}\sqrt{\frac{m_xm_y}{m_z}}\frac{(2E)^{3/2}}{3} \tag{B33}$$

Let us now finally calculate equation (B1):

(The DOS is the denominator for both equation (B4a) and (B4b), so equation (B1) is just the numerators for both equations.)

(Sum the 6 ellipsoidal bands for equation (B33) and equation (B26) separately, THEN divide the result.)

$$\frac{\langle v_z^2 \rangle}{\langle v_z^+ \rangle}\Bigg|_{Silicon} = \frac{\dfrac{\left(2(E-E_c)\right)^{3/2}}{3}\left(\dfrac{2m_t}{\sqrt{m_\ell}}+\dfrac{4\sqrt{m_\ell}}{1}\right)}{\dfrac{2(E-E_c)}{2}\left(\dfrac{2m_t}{1}+\dfrac{4\sqrt{m_\ell m_t}}{1}\right)} = \frac{2\sqrt{2(E-E_c)}}{3}\left(\dfrac{\dfrac{2}{m_\ell}+\dfrac{4}{m_t}}{\dfrac{2}{\sqrt{m_\ell}}+\dfrac{4}{\sqrt{m_t}}}\right) \tag{B34}$$

We are left with a combination of the transverse and longitudinal effective masses, with the expected square root of two times Energy. The factor of 2/3 for angle averaging in 3-D is also expected from equation (B3).

B.3 Derivation of a Fermi Surface Complexity Factor (FSCF) for Multiple Ellipsoidal Bands

To quantify the beneficial effects of valley degeneracy we define a Fermi Surface Complexity Factor (FSCF'), similar to one that has recently been introduced [85], for a general ellipsoidal band and extend the result to a Si-like material with 6 valleys.

In [85], the authors define a FSCF as

$$FSCF^1 = \left(\frac{m_s^*}{m_c^*}\right)^{3/2}, \tag{B35}$$

where m_S^* is the so-called Seebeck effective mass (which is the density-of-states effective mass determined from the Seebeck coefficient) and m_c^* is the conventional conductivity effective mass [86],

$$m_c^* = \frac{3}{1/m_\ell + 2/m_t}, \tag{B36}$$

which is the harmonic mean of the directional effective masses.

For a single valley with an effective mass of m^*, (B35) gives $FSCF = 1$. For N_V spherical valleys with an effective mass of m^*, (B35) gives $FSCF = N_V$ (because $m_S^* \propto N_V^{2/3}$). Inserting numbers relevant for the conduction band of Si $\left(N_V = 6, m_t = 0.19m_0, m_\ell = 0.93m_0 \right)$, we find $FSCF = 8.35 > 6$, which reflects both the benefits of a valley degeneracy of 6 and the valley anisotropy (in this case, $K^* = 8.35/6 = 1.39$), which produces a light effective mass in the direction of transport.

It would be useful to have a measure of the benefits of Fermi surface complexity that does not involve effective masses, which can be problematic to define for complex band structures.

We start with the transport distribution defined in the Landauer form as,

$$\Xi(E) = \frac{2}{h} \lambda(E) M(E) / A, \tag{B37}$$

with

$$\frac{\lambda(E)}{2} = \frac{\langle v_x^2 \tau_m \rangle}{\langle |v_x| \rangle} \text{ and} \tag{B38}$$

$$M(E)/A \equiv \frac{h}{4} \langle |v_x| \rangle D(E). \tag{B39}$$

Assuming the scattering time in eq. (B38) is isotropic and inversely proportional to the total DOS (B11),

$$\frac{1}{\tau(E)} = \frac{1}{\tau_m(E)} \propto K_{el-ph} DOS(E), \tag{B40}$$

we can rewrite (B37) as,

$$\Xi(E) = \frac{\langle v_x^2(E) \rangle}{K_{el-ph}}. \tag{B41}$$

If a dimensionless numerical metric is desired, the transport function could be divided by the transport function of a corresponding spherical band with the same electron-phonon coupling parameter,

$$FSCF^2 = \frac{\Xi(E)}{\Xi_{sph}(E)} = \frac{\dfrac{\dfrac{1}{\Omega} \sum_{\vec{k},k_z>0} v_z^2 \delta(E - E_k)}{\dfrac{1}{\Omega} \sum_{\vec{k},k_z>0} \delta(E - E_k)}}{\left(\dfrac{\dfrac{1}{\Omega} \sum_{\vec{k},k_z>0} v_z^2 \delta(E - E_k)}{\dfrac{1}{\Omega} \sum_{\vec{k},k_z>0} \delta(E - E_k)} \right)_{Spherical}}. \tag{B42}$$

Using equations from section 1 with silicon ellipsoidal bands, and assuming the equivalent spherical transport distribution in (B42) has a conductivity effective mass equivalent to $m_{eq}^* = m_{DOM}^*$ which comes from the numerator of (B42), thus we get,

$$FSCF^2 = \frac{\Xi(E)}{\Xi_{sph}(E)} = \frac{\dfrac{\dfrac{1}{3} \dfrac{(2E)^{3/2}}{2\pi^2\hbar^3} \left(\dfrac{2m_t}{\sqrt{m_\ell}} + \dfrac{4\sqrt{m_\ell}}{1} \right)}{\dfrac{6\sqrt{m_t^2 m_\ell (2E)}}{2\pi^2\hbar^3}}}{\dfrac{\dfrac{1}{3} \dfrac{(2E)^{3/2}}{2\pi^2\hbar^3} \sqrt{m_{DOM}^*}}{\dfrac{\sqrt{(m_{DOM}^*)^3 (2E)}}{2\pi^2\hbar^3}}}. \tag{B43}$$

Using eqn. (14) and simplifying for this analytic case gives,

$$FSCF^2 = \frac{\Xi(E)}{\Xi_{sph}(E)} = \frac{4}{6}\frac{m_t}{m_\ell} + \frac{8}{6} + \frac{8}{6}\sqrt{\frac{m_t}{m_\ell}} + \frac{16}{6}\sqrt{\frac{m_\ell}{m_t}} \ . \qquad (B44)$$
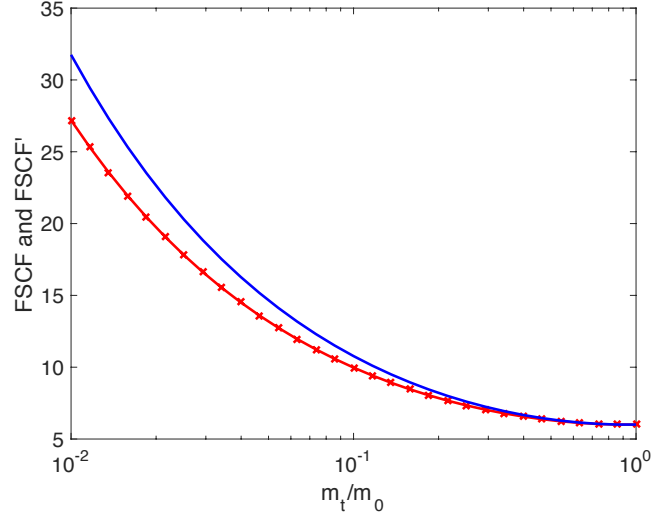
Fig. B1 Comparison of eqns. (B35) and (B44) vs. the transverse effective mass. The longitudinal effective mass is set to $m_\ell = 0.93m_0$. Equation (B44) is the line with markers, while eq. (B35) is shown as a solid line. When $m_t \rightarrow m_\ell$ both equations converge to N_V, which in the case of a Si-like material is 6.

The ratio in (B42) will be energy dependent if the material being considered does not have parabolic energy bands in numerical simulations. There are several ways to produce a single number metric; for example, (B42) could be evaluated at the energy that maximizes $n(E) = f_0(E)D(E)$ or an average over the Fermi window could be evaluated to write

$$\langle FSCF \rangle^3 = \frac{\langle \Xi(E) \rangle}{\langle \Xi_{sph}(E) \rangle} \qquad (B45)$$

where in (45), the brackets denote an average that is defined as

$$\langle \bullet \rangle \equiv \frac{\int\limits_{E_C}^{\infty}(\bullet)(-\partial f_0/\partial E)dE}{\int\limits_{E_C}^{\infty}(-\partial f_0/\partial E)dE}.$$

(B46)

Both our metric (B44, B45) and Gibbs' eq. (B35), can benefit from first principles studies of scattering. Instead of dividing by 6 to get the benefits of anisotropy in all three equations, which assumes inter and intra are equal, we can get an exact factor to divide by from the realistic scattering rates to obtain a factor that includes both the benefits due to anisotropy as well as any residual benefit from degenerative valleys after scattering is taken into account. In the silicon case, all three metrics (B35, B44, and (B45 which is numerical), give similar results because silicon can be modeled well by parabolic bands. However, in materials where the effective mass approximation is less accurate, i.e. complex TE materials, (B45) more accurately captures the effects of the complicated band structure since we are using the full band numerical calculations.

APPENDIX C

C.1 Preface

The contents of this chapter have been extracted from the following publications with permission: E. Witkoske, X. Wang, J. Maassen, and M. Lundstrom, "Universal behavior of the thermoelectric figure of merit , zT , vs . quality factor," *Mater. Today Phys.*, vol. 8, pp. 43–48, 2019.

C.2 Analytical solutions for thermoelectric parameters

C.2.1 Parabolic energy bands:

For parabolic energy bands in 1D, 2D, or 3D (d = 1, 2, or 3) and with power law scattering, we find from the results in the appendix of [42] that

$$\sigma_{1D} = \frac{2q^2}{h}\lambda_0 \Gamma(r+1)\mathcal{F}_{r-1}(\eta_F) \qquad \text{(S-m)} \qquad \text{(C1)}$$

$$\sigma_{2D} = \frac{2q^2}{h}\lambda_0 \left(\frac{\sqrt{2m^* k_B T}}{\pi\hbar}\right)\Gamma(r+3/2)\mathcal{F}_{r-1/2}(\eta_F) \qquad \text{(S)} \qquad \text{(C2)}$$

$$\sigma_{3D} = \frac{2q^2}{h}\lambda_0 \left(\frac{m^* k_B T}{2\pi\hbar^2}\right)\Gamma(r+2)\mathcal{F}_{r}(\eta_F) \qquad \text{(S/m)} \qquad \text{(C3)}$$

$$S_{d=1,2,3} = -\left(\frac{k_B}{q}\right)\left(\frac{\left(r+(d+1)/2\right)\mathcal{F}_{r+(d-1)/2}(\eta_F)}{\mathcal{F}_{r+(d-3)/2}(\eta_F)} - \eta_F\right) \qquad \text{(V/K)} \qquad \text{(C4)}$$

$$L'_{d=1,2,3} = L_{d=1,2,3}\Big/\left(k_B/q\right)^2 \qquad \text{(C5)}$$

$$L'_{d=1,2,3} = \frac{\Gamma\left(r+(d+3)/2\right)}{\Gamma\left(r+(d+1)/2\right)}\left(\begin{array}{c}\left(r+(d+3)/2\right)\dfrac{\mathcal{F}_{r+(d+1)/2}(\eta_F)}{\mathcal{F}_{r+(d-3)/2}(\eta_F)}\\[4mm] -\left(r+(d+1)/2\right)\left(\dfrac{\mathcal{F}_{r+(d-1)/2}(\eta_F)}{\mathcal{F}_{r+(d-3)/2}(\eta_F)}\right)^2\end{array}\right), \qquad \text{(C6)}$$

where

$$\eta_F = \left(E_F - E_C\right)/k_B T \tag{C7}$$

is the dimensionless Fermi energy (chemical potential) and $\mathcal{F}_j\left(\eta_F\right)$ is the Fermi-Dirac integral of order j written in the Blakemore form [73]

$$\mathcal{F}_j\left(\eta_F\right) = \frac{1}{\Gamma(j+1)} \int_0^\infty \frac{\eta^j d\eta}{1 + e^{\eta - \eta_F}} \ . \tag{C8}$$

It should be noted that the radius of the nanowire and thickness of the quantum well, do not appear in (C1) and (C2).

For ADP scattering in 3D, $r = 0$, in 2D, $r = 1/2$, and 1D, $r = 1$, so from (C4) and (C5) we find

$$S_{d=1,2,3} = -\left(\frac{k_B}{q}\right)\left(\frac{2\mathcal{F}_1\left(\eta_F\right)}{\mathcal{F}_0\left(\eta_F\right)} - \eta_F\right) \tag{C9}$$

and

$$L_{d=1,2,3} = 2\left(\frac{k_B}{q}\right)^2 \left\{3\frac{\mathcal{F}_2\left(\eta_F\right)}{\mathcal{F}_0\left(\eta_F\right)} - \frac{2\mathcal{F}_1^2\left(\eta_F\right)}{\mathcal{F}_0^2\left(\eta_F\right)}\right\}. \tag{C10}$$

For ADP scattering in parabolic bands, the Seebeck coefficient and Lorenz numbers are identical in all dimensions.

C2.2   Single energy channel

Analytical solutions are easy to obtain for the single energy channel case,

$$M\left(E\right)/A = M_0 \delta\left(E - E_C\right), \tag{C11}$$

where E_C is the energy of the channel. We find

$$\sigma_\delta = \frac{2q^2}{h}\lambda_0 M_0 \left(-\frac{\partial f_0}{\partial E}\bigg|_{E=E_C}\right) = \frac{2q^2}{h}\lambda_0 \langle M \rangle, \tag{C12}$$

$$S_\delta = \left(-\frac{k_B}{q} \right) \frac{E_C - E_F}{k_B T} \; , \tag{C13}$$

and

$$L_\delta = 0 \; . \tag{C14}$$

The figure of merit for the single energy case is readily shown to be

$$zT = \frac{S^2 \sigma T}{\kappa_L} = \left(\frac{k_B}{q} \right)^2 \left(\frac{E_C - E_F}{k_B T} \right)^2 \frac{2q^2 \lambda_0 M_0 T}{h \times \kappa_L} \left(-\frac{\partial f_0}{\partial E} \Big|_{E=E_C} \right) \tag{C15}$$

At the maximum zT, $\left| E_C - E_F \right| / k_B T = 2.4$ and $\partial f_0 / \partial E \big|_{E=E_C} = 0.076 / k_B T$, we find

$$zT \big|_{\text{max}} = 0.88 \left(\frac{k_B}{h} \right) \left(\frac{\lambda_0 M_0}{\kappa_L} \right) \tag{C16}$$

which is essentially eqn. (21) of [93] in a different notation.

Finally, we compute the peak zT vs. b-factor at the peak characteristic for a single energy channel. Because the Lorenz number for a single energy channel is zero, (C2) gives

$$zT = \left(S' \right)^2 b_L \tag{C17}$$

At the maximum zT, $\left| E_C - E_F \right| / k_B T = 2.4$, so $S' = -2.4$, and (C17) gives

$$zT = 5.76 b_L , \tag{C18}$$

which is the equation of the dotted straight line in Fig. C2.

C.3 Observation of "Double-branch" behavior in zT|max vs. b-factor for certain band structures

Some curious behaviors were observed when investigating hypothetical band structures using the effective mass approach. An example of such a peculiar band structure is shown in Figure C1

119

(left). It consists of two valence bands with energy offsets of 0.2 eV. The highest valence band (Band #1) is isotropic, and the lower band (Band #2) is anisotropic with the same Density of States (DOS) effective mass, but 5 times the Distribution of Modes (DOM) effective mass in transport direction as Band #1. In other words, Band #2 has the same amount of states but much higher velocity—this is advantageous for obtaining higher TE performance. The resulting DOS and DOM of this band structure are shown in Figure C1 (right).
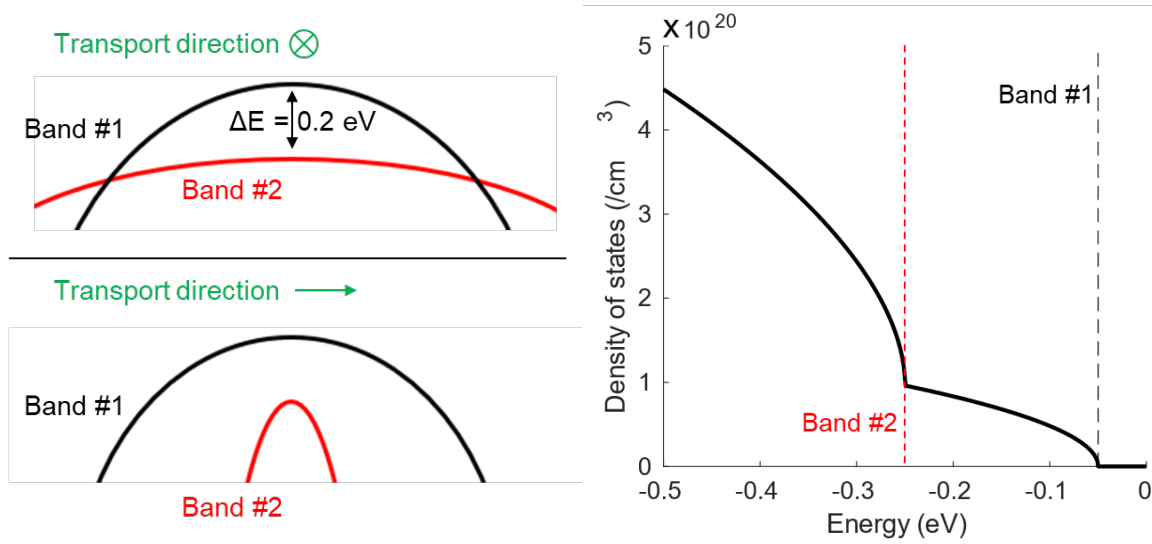
Figure C1. (Left) The two-band toy model is used. The highest valence band (black) is 0.2 eV higher than Band #2 (red). Along the transport direction, Band #2 has high velocity. Both bands have the same DOS. **(Right)** The DOS of the two-band model. The edges of Band #1 and Band #2 are marked with black and red dash lines respectively.
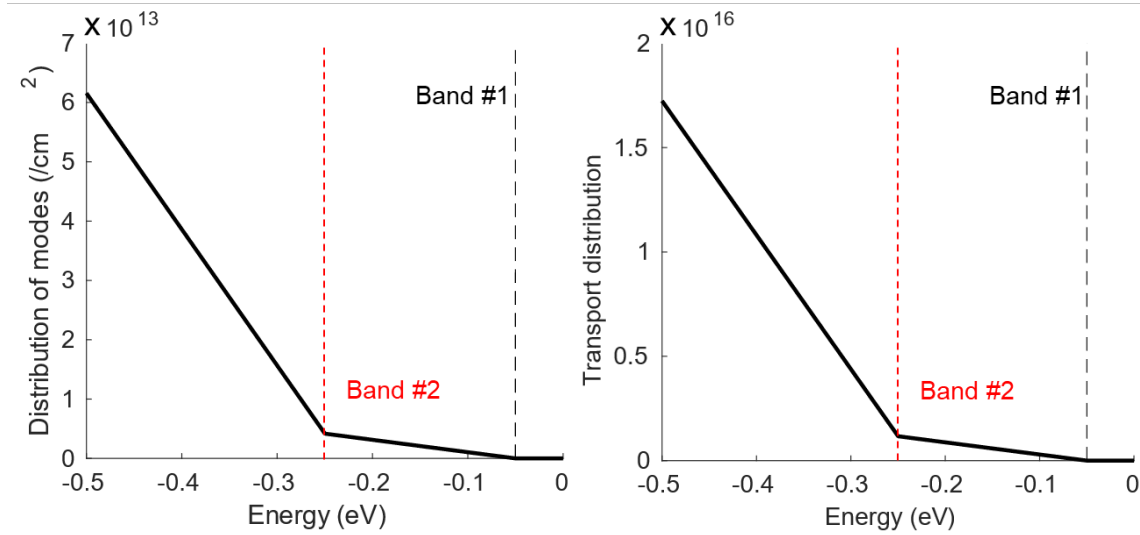
Figure C2. (Left) The DOM of the two-band model. **(Right)** The transport distribution of the two-band model. The edges of Band #1 and Band #2 are marked with black and red dash lines respectively.

The peculiarity arises from the optimal location of the Fermi level under a given lattice thermal conductivity, κ_L. The two bands are essentially in a tight competition with each other for having the maximum zT. The lower band, Band #2, has the advantage of significantly increased DOM, but it also faces the issue that, if the Fermi level is close enough to take advantage of the increased DOM, a significant amount of current will flow on both sides of the Fermi level, due to the presence of Band #1. This is essentially a bipolar effect that decreases the Seebeck coefficient and increases the electronic thermal conductivity—both are undesired and counters the increased electrical conductivity obtained from the increased DOM. This therefore results in a competition between Band #1 and Band #2 for the optimal location of the Fermi level.

This competition is illustrated in Figure C2. Figure C2 (left) shows the situation under a high κ_L. With a high κ_L, the electronic thermal conductivity is insignificant, and the optimal location of the Fermi level is decided solely by the power factor. In this case, Band #2 with its high electrical conductivity shows a higher zT than Band #1. However, if κ_L is decreased, the benefit

of having a lower electronic thermal conductivity quickly catches up for Band #1, and as shown in Figure C2 (right), the maximum zT shifts to favor Band #1.
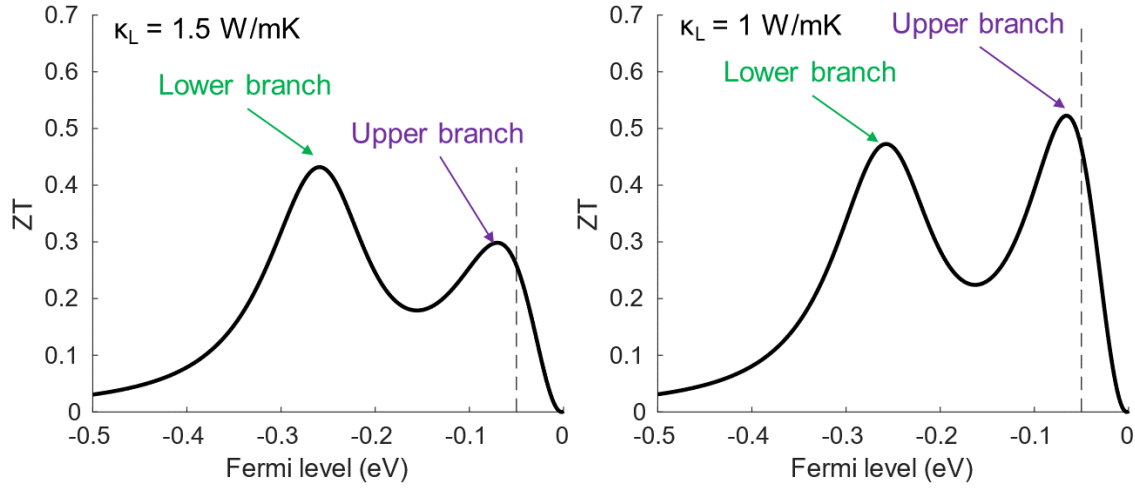
Figure C3. (Left) zT vs. Fermi level under high lattice thermal conductivity. **(Right)** zT vs. Fermi level under a moderate lattice thermal conductivity showing the optimal location of the Fermi level for maximum zT shifts. The location of the highest valence band is marked with black dash line.

Because the optimal location of the Fermi level for maximum zT "jumped" from Band #2 to Band #1, it shows up in the $zT|_{max}$ vs. b_L curve as a "snapback" as shown in Figure C4. Since b_L is a ratio between electrical conductivity and lattice thermal conductivity, when the optical location of Fermi level "jumped" from Band #2 to Band #1, the electrical conductivity decreases, causing b_L to decrease. This "snapback" feature forms two distinct branches of the $zT|_{max}$ vs. b_L curve.
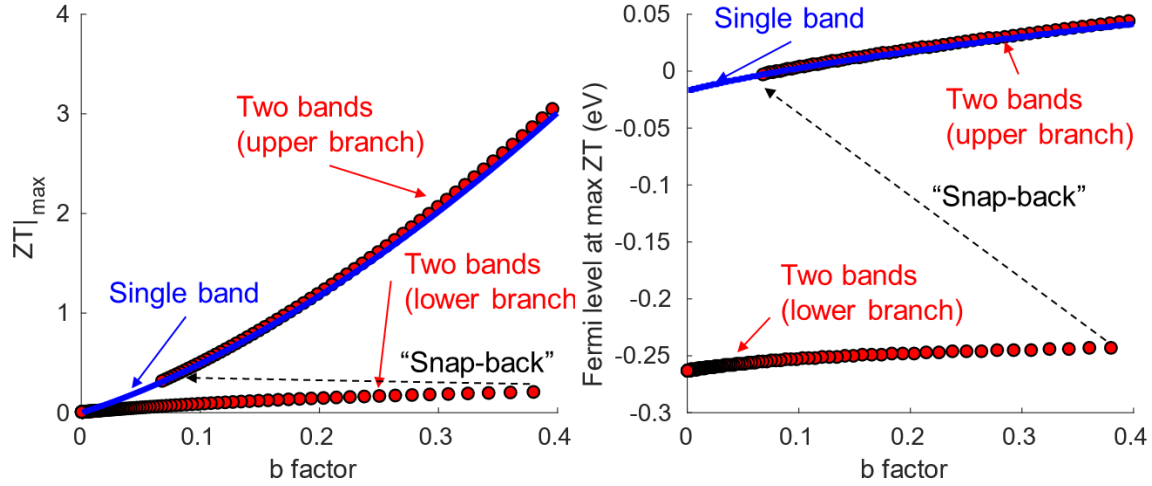
Figure C4. Comparison between the example two-band structure and a single parabolic band for **(Left)** $zT|_{max}$ vs. b_L and **(Right)** optimal location of the Fermi level vs. b_L.

The location of this "snap-back" does not depend on whether the $zT|_{max}$ vs. b_L curve is obtained via a sweep of κ_L or σ (i.e. by adjusting the electron-phonon coupling strength). Recall from earlier discussions that the thermoelectric Figure of Merit (FOM) can be defined as follows

$$zT = \frac{S^2 \sigma T}{\kappa_e + \kappa_L} = \frac{S^2 / (k_B/q)^2}{\dfrac{\kappa_e}{\sigma T (k_B/q)^2} + \dfrac{\kappa_L}{\sigma T (k_B/q)^2}} = \frac{S'^2}{L' + 1/b_L} \tag{C18}$$

with,

$$b_L = \frac{\sigma T}{\kappa_L}\left(\frac{k_B}{q}\right)^2. \tag{C19}$$

We will show that it is equivalent to vary b_L through adjusting κ_L or σ. To increase σ by a factor of N, one can scale the electron-phonon coupling parameter by a factor of 1/N. The resulting S is unaffected by this scaling, and κ_e is scaled by a factor of N. Equation (C18) becomes

$$zT = \frac{S^2 \sigma T}{\kappa_e + \kappa_L} = \frac{S^2 / (k_B/q)^2}{\dfrac{N\kappa_e}{N\sigma T (k_B/q)^2} + \dfrac{\kappa_L}{N\sigma T (k_B/q)^2}} = \frac{S'^2}{L' + 1/Nb_L}. \tag{C20}$$

Therefore, this has the same effect as scaling κ_L by a factor of 1/N.

C.4 A comparison of B, $b_L(\hat{E}_F)$, and $zT(\hat{E}_F)$

The conventional B-factor is defined for parabolic bands and does not include a Fermi level dependence. For parabolic bands, the relation between this and $b_L(E_F)$ is given by eqn. (3.9),

$$b_L(E_F) \equiv \frac{\sigma(E_F)T}{\kappa_L}(k_B/q)^2 = B\mathcal{F}_{1/2}\left[(E_F - E_C)/k_B T\right].$$

(C21)

Our motivation for using a generalized quality factor is that it allows us to deal directly with complex band structures without extracting effective masses and allows inclusion of more general scattering models (e.g. beyond power law). It is also, in principle directly measurable because it depends only on the measured electrical and lattice thermal conductivities.

The quantity b_L',

$$b_L'(E_F) \equiv \frac{\sigma(E_F)T(k_B/q)^2}{\kappa_L \mathcal{F}_{1/2}\left[(E_F - E_C)/k_B T\right]}.$$

(C22)

defined in eqn. (3.10) of the chapter is more similar to B, but it is hard to make general quantitative statements because b_L' depends on the specifics of the complex band structure.
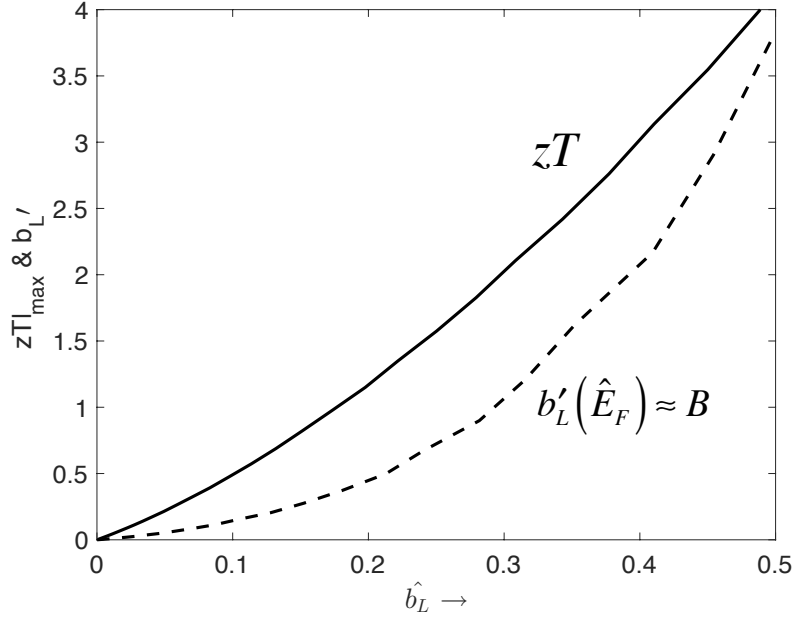
Figure C5. This plot shows two quantities $zT\left(\hat{E}_F\right)$ and $b'_L\left(\hat{E}_F\right)$, versus $b_L\left(\hat{E}_F\right)$ for visual comparison using a parabolic band with $r = 0$.

The figure above is a plot of $zT\left(\hat{E}_F\right)$ vs. $b_L\left(\hat{E}_F\right)$ for parabolic bands with $r = 0$ (the same as the solid line in Fig. 3.2 in the chapter). Shown in the same figure is a plot of B vs. $b_L\left(\hat{E}_F\right)$ with the same scattering, r = 0 assumed. For a given zT, one can read off the required B- or b_L-factor. For a given B, one can also read off the corresponding b_L for an appropriate comparison. A value of $b'_L\left(\hat{E}_F\right) \approx B = 0.4$ which is a reference value often used, corresponds to $b_L\left(\hat{E}_F\right) = 0.18$ in our work. To achieve a $zT\left(\hat{E}_F\right) \approx 2$ requires a $b'_L\left(\hat{E}_F\right) \approx B \approx 1$ and a $b_L\left(\hat{E}_F\right) \approx 0.3$.

LIST OF REFERENCES

[1] G. D. Mahan, "Introduction to thermoelectrics," *APL Mater.*, vol. 4, no. 10, 2016.

[2] H. J. Goldsmid, *The Physics of Thermoelectric Energy Conversion*. IOP Publishing, 2017.

[3] A. Ziabari, M. Zebarjadi, D. Vashaee, and A. Shakouri, "Nanoscale solid-state cooling: A review," *Reports Prog. Phys.*, vol. 79, no. 9, 2016.

[4] G. Chen, M. S. Dresselhaus, G. Dresselhaus, J.-P. Fleurial, and T. Caillat, "Recent developments in thermoelectric materials," *Int. Mater. Rev.*, vol. 48, no. 1, pp. 45–66, 2003.

[5] J. He and T. M. Tritt, "Advances in thermoelectric materials research: Looking back and moving forward," *Science (80-.).*, vol. 357, no. 6358, p. eaak9997, 2017.

[6] B. Poudel, Q. Hao, Y. Ma, Y. Lan, A. Minnich, B. Yu, X. Yan, D. Wang, A. Muto, D. Vashaee, X. Chen, J. Liu, M. S. Dresselhaus, G. Chen, and Z. Ren, "High-Thermoelectric Performance of Nanostructured Bismuth Antimony Telluride Bulk Alloys," *Science*, vol. 320, no. 5876, pp. 634–638, 2008.

[7] G. Joshi, H. Lee, Y. Lan, X. Wang, G. Zhu, D. Wang, R. W. Gould, D. C. Cuff, M. Y. Tang, M. S. Dresselhaus, G. Chen, and Z. Ren, "Enhanced thermoelectric figure-of-merit in nanostructured p-type silicon germanium bulk alloys," *Nano Lett.*, vol. 8, no. 12, pp. 4670–4674, 2008.

[8] X. W. Wang, H. Lee, Y. C. Lan, G. H. Zhu, G. Joshi, D. Z. Wang, J. Yang, a. J. Muto, M. Y. Tang, J. Klatsky, S. Song, M. S. Dresselhaus, G. Chen, and Z. F. Ren, "Enhanced thermoelectric figure of merit in nanostructured n-type silicon germanium bulk alloy," *Appl. Phys. Lett.*, vol. 93, no. 19, p. 193121, 2008.

[9] W. Kim, J. Zide, A. Gossard, D. Klenov, S. Stemmer, A. Shakouri, and A. Majumdar, "Thermal conductivity reduction and thermoelectric figure of merit increase by embedding nanoparticles in crystalline semiconductors," *Phys. Rev. Lett.*, vol. 96, no. 4, pp. 1–4, 2006.

[10] A. J. Minnich, M. S. Dresselhaus, Z. F. Ren, and G. Chen, "Bulk nanostructured thermoelectric materials: current research and future prospects," *Energy Environ. Sci.*, vol. 2, no. 5, p. 466, 2009.

[11] K. Biswas, J. He, I. D. Blum, C. I. Wu, T. P. Hogan, D. N. Seidman, V. P. Dravid, and M. G. Kanatzidis, "High-performance bulk thermoelectrics with all-scale hierarchical architectures," *Nature*, vol. 489, no. 7416, pp. 414–418, 2012.

[12] C. J. Vineis, A. Shakouri, A. Majumdar, and M. G. Kanatzidis, "Nanostructured Thermoelectrics: Big Efficiency Gains from Small Features," *Adv. Mater.*, vol. 22, no. 36, pp. 3970–3980, Sep. 2010.

[13] Q. H. Zhang, X. Y. Huang, S. Q. Bai, X. Shi, C. Uher, and L. D. Chen, "Thermoelectric Devices for Power Generation: Recent Progress and Future Challenges," *Adv. Eng. Mater.*, vol. 18, no. 2, pp. 194–213, Feb. 2016.

[14] G. L. Bennett, J. J. Lombardo, R. J. Hemler, G. Silverman, C. W. Whitmore, W. R. Amos, E. W. Johnson, R. W. Zocher, J. C. Hagan, and R. W. Englehart, "The general-purpose heat source radioisotope thermoelectric generator: A truly general-purpose space RTG," in *AIP Conference Proceedings*, 2008, vol. 969, pp. 663–671.

[15] J. A. Paradiso and T. Starner, "Energy scavenging for mobile and wireless electronics," *IEEE Pervasive Comput.*, vol. 4, no. 1, pp. 18–27, 2005.

[16] X. Zhang and L.-D. Zhao, "Thermoelectric materials: Energy conversion between heat and electricity," *J. Mater.*, vol. 1, no. 2, pp. 92–105, 2015.

[17] J. F. Li, W. S. Liu, L. D. Zhao, and M. Zhou, "High-performance nanostructured thermoelectric materials," *NPG Asia Materials*, vol. 2, no. 4. pp. 152–158, 2010.

[18] L. D. Hicks and M. S. Dresselhaus, "Effect of quantum-well structures on the thermoelectric figure of merit," *Phys. Rev. B*, vol. 47, no. 19, pp. 12727–12731, 1993.

[19] A. Shakouri, "Recent Developments in Semiconductor Thermoelectric Physics and Materials," *Annu. Rev. Mater. Res.*, 2011.

[20] D. Park, S. Park, K. Jeong, H.-S. Jeong, J. Y. Song, and M. Cho, "Thermal and Electrical Conduction of Single-crystal Bi2Te3 Nanostructures grown using a one step process," *Sci. Rep.*, vol. 6, no. 1, p. 19132, 2016.

[21] J. P. Heremans, V. Jovovic, E. S. Toberer, A. Saramat, K. Kurosaki, A. Charoenphakdee, S. Yamanaka, and G. J. Snyder, "Enhancement of Thermoelectric Efficiency in PbTe by Distortion of the Electronic Density of States," *Science*, vol. 321, no. 5888, pp. 554–557, 2008.

[22] L.-D. Zhao, S.-H. Lo, Y. Zhang, H. Sun, G. Tan, C. Uher, C. Wolverton, V. P. Dravid, and M. G. Kanatzidis, "Ultralow thermal conductivity and high thermoelectric figure of merit in SnSe crystals," *Nature*, vol. 508, no. 7496, pp. 373–377, 2014.

[23] J. Androulakis, Y. Lee, I. Todorov, D. Y. Chung, and M. Kanatzidis, "High-temperature thermoelectric properties of n-type PbSe doped with Ga, In, and Pb," *Phys. Rev. B - Condens. Matter Mater. Phys.*, vol. 83, no. 19, pp. 1–9, 2011.

[24] E. S. Toberer, P. Rauwel, S. Gariel, J. Taftø, and G. Jeffrey Snyder, "Composition and the thermoelectric performance of β-Zn4Sb3," *J. Mater. Chem.*, vol. 20, no. 44, p. 9877, 2010.

[25] W. Liu, H. S. Kim, S. Chen, Q. Jie, B. Lv, M. Yao, Z. Ren, C. P. Opeil, S. Wilson, C.-W. Chu, and Z. Ren, "n-type thermoelectric material $Mg_2 Sn_{0.75} Ge_{0.25}$ for high power generation," *Proc. Natl. Acad. Sci.*, vol. 112, no. 11, pp. 3269–3274, 2015.

[26] L. Zhao, X. Wang, F. Y. Fei, J. Wang, Z. Cheng, S. Dou, J. Wang, and G. J. Snyder, "High thermoelectric and mechanical performance in highly dense $Cu_{2-x} S$ bulks prepared by a melt-solidification technique," *J. Mater. Chem. A*, vol. 3, no. 18, pp. 9432–9437, 2015.

[27] B. Orr, A. Akbarzadeh, M. Mochizuki, and R. Singh, "A review of car waste heat recovery systems utilising thermoelectric generators and heat pipes," *Appl. Therm. Eng.*, vol. 101, pp. 490–495, 2016.

[28] K. Yazawa and A. Shakouri, "Scalable cost/performance analysis for thermoelectric waste heat recovery systems," *J. Electron. Mater.*, vol. 41, no. 6, pp. 1845–1850, 2012.

[29] K. Yazawa and A. Shakouri, "Cost-effective waste heat recovery using thermoelectric systems," *J. Mater. Res.*, vol. 27, no. 9, pp. 1211–1217, 2012.

[30] C. Yu and K. T. Chau, "Thermoelectric automotive waste heat energy recovery using maximum power point tracking," *Energy Convers. Manag.*, vol. 50, no. 6, pp. 1506–1512, 2009.

[31] D. T. Crane and G. S. Jackson, "Systems-level optimization of low-temperature thermoelectric waste heat recovery," *37th Intersoc. Energy Convers. Eng. Conf.*, no. 20076, pp. 583–588, 2002.

[32] S. LeBlanc, "Thermoelectric generators: Linking material properties and systems engineering for waste heat recovery applications," *Sustain. Mater. Technol.*, vol. 1, pp. 26–35, 2014.

[33] "COMSOL Multiphysics 5.4." COMSOL AB, Stockhold Sweden.

[34] J. F. Munro, "The Story of Electricity," *D. Appleton and Company*, 1902. Available: http://hdl.handle.net/2027/uc2.ark:/13960/t6f18tq1p.

[35] A. F. Ioffe, L. S. Stil'bans, E. K. Iordanishvili, T. S. Stavitskaya, A. Gelbtuch, and G. Vineyard, " Semiconductor Thermoelements and Thermoelectric Cooling ," *Phys. Today*, 2009.

[36] L. E. Bell, "Cooling, heating, generating power, and recovering waste heat with thermoelectric systems," *Science*. 2008.

[37] M. V. Vedernikov and E. K. Iordanishvili, "A.F. Ioffe and origin of modern semiconductor thermoelectric energy conversion," 2002.

[38] H. B. Callen, "The Application of Onsager's Reciprocal Relations to Thermoelectric, Thermomagnetic, and Galvanomagnetic Effects," *Phys. Rev.*, vol. 73, no. 11, pp. 1349–1358, Jun. 1948.

[39] C. Wood, "Materials for thermoelectric energy conversion," *Reports Prog. Phys.*, vol. 51, no. 4, pp. 459–539, 1988.

[40] G. D. Mahan, "Good Thermoelectrics," in *Solid State Physics Volume 51*, 1998, pp. 81–157.

[41] D. Narducci, "Do we really need high thermoelectric figures of merit? A critical appraisal to the power conversion efficiency of thermoelectric materials," *Appl. Phys. Lett.*, vol. 99, no. 10, 2011.

[42] M. Lundstrom and C. Jeong, *Near-equilibrium Transport, vol. 2 of Lessons from Nanoscience Lecture Note Series*. Singapore: World Scientific, 2013.

[43] S. Datta, "Lessons from Nanoelectronics: A New Perspective on Transport," in *Lessons from Nanoelectronics: A New Perspective on Transport*, 2012.

[44] C. Jeong, R. Kim, M. Luisier, S. Datta, and M. Lundstrom, "On Landauer versus Boltzmann and full band versus effective mass evaluation of thermoelectric transport coefficients," *J. Appl. Phys.*, vol. 107, no. 2, 2010.

[45] N. Lu and I. Ferguson, "III-nitrides for energy production: Photovoltaic and thermoelectric applications," *Semiconductor Science and Technology*, vol. 28, no. 7. pp. 1–11, 2013.

[46] E. N. Hurwitz, M. Asghar, A. Melton, B. Kucukgok, L. Su, M. Orocz, M. Jamil, N. Lu, and I. T. Ferguson, "Thermopower study of GaN-based materials for next-generation thermoelectric devices and applications," in *Journal of Electronic Materials*, 2011, vol. 40, no. 5, pp. 513–517.

[47] C. K. Ghosh, D. Sarkar, M. K. Mitra, and K. K. Chattopadhyay, "Electronic structure and optical properties of CuAlO2 under biaxial strain," *J. Phys. Condens. Matter*, vol. 24, no. 23, p. 235501, 2012.

[48] R. Robert, S. Romer, A. Reller, and A. Weidenkaff, "Nanostructured complex cobalt oxides as potential materials for solar thermoelectric power generators," *Adv. Eng. Mater.*, vol. 7, no. 5, pp. 303–308, 2005.

[49] H. Kawazoe, M. Yasukawa, H. Hyodo, M. Kurita, H. Yanagi, and H. Hosono, "P-type electrical conduction in transparent thin films of CuAlO2," *Nature*, vol. 389, no. 6654, pp. 939–942, 1997.

[50] K. Koumoto, H. Koduka, and W.-S. Seo, "Thermoelectric properties of single crystal CuAlO2 with a layered structure," *J. Mater. Chem.*, vol. 11, pp. 251–252, 2001.

[51] Y. Feng, X. Jiang, E. Ghafari, B. Kucukgok, C. Zhang, I. Ferguson, and N. Lu, "Metal oxides for thermoelectric power generation and beyond," *Adv. Compos. Hybrid Mater.*, pp. 114–126, 2017.

[52] P. Giannozzi *et al.*, "QUANTUM ESPRESSO: A modular and open-source software project for quantum simulations of materials," *J. Phys. Condens. Matter*, vol. 21, no. 39, 2009.

[53] K. Conrad, J. Maassen, and M. Lundstrom, "LanTraP," 2014. Available: https://nanohub.org/resources/19427.

[54] L. Paulatto, F. Mauri, and M. Lazzeri, "Anharmonic properties from a generalized third-order ab initio approach: Theory and applications to graphite and graphene," *Phys. Rev. B*, vol. 87, no. 21, p. 214303, Jun. 2013.

[55] G. Fugallo, M. Lazzeri, L. Paulatto, and F. Mauri, "Ab initio variational approach for evaluating lattice thermal conductivity," *Phys. Rev. B*, vol. 88, no. 4, p. 45430, Jul. 2013.

[56] G. Xing, J. Sun, K. P. Ong, X. Fan, W. Zheng, and D. J. Singh, "Perspective: n-type oxide thermoelectrics via visual search strategies," *APL Mater.*, vol. 4, no. 5, p. 053201, 2016.

[57] G. J. Snyder and E. S. Toberer, "Complex thermoelectric materials," *Nat. Mater.*, vol. 7, no. 2, pp. 105–114, 2008.

[58] Q. Hao, D. Xu, N. Lu, and H. Zhao, "High-throughput ZT predictions of nanoporous bulk materials as next-generation thermoelectric materials: A material genome approach," *Phys. Rev. B*, vol. 93, no. 20, pp. 1–11, 2016.

[59] T. Tong, D. Fu, a. X. Levander, W. J. Schaff, B. N. Pantha, N. Lu, B. Liu, L. Ferguson, R. Zhang, J. T. Lin, H. X. Jiang, J. Wu, and D. G. Cahill, "Suppression of thermal conductivity in In x Ga 1-x N alloys by nanometer-scale disorder," *Appl. Phys. Lett.*, vol. 102, no. 2013, p. 121906, 2013.

[60] X. Chen, D. Parker, and D. J. Singh, "Importance of non-parabolic band effects in the thermoelectric properties of semiconductors," *Sci. Rep.*, vol. 3, pp. 2–7, 2013.

[61] H. Wang, Y. Pei, A. D. LaLonde, and G. Jeffrey Snyder, "Material Design Considerations Based on Thermoelectric Quality Factor," *Thermoelectr. Nanomater.*, vol. 182, no. 1, pp. 3–32, 2013.

[62] Y. Pei, H. Wang, and G. J. Snyder, "Band engineering of thermoelectric materials," *Advanced Materials*, vol. 24, no. 46. pp. 6125–6135, 2012.

[63] Y. Pei, X. Shi, A. Lalonde, H. Wang, L. Chen, and G. J. Snyder, "Convergence of electronic bands for high performance bulk thermoelectrics," *Nature*, vol. 473, no. 7345, pp. 66–69, 2011.

[64] Y. Pei, A. D. LaLonde, H. Wang, and G. J. Snyder, "Low effective mass leading to high thermoelectric performance," *Energy Environ. Sci.*, vol. 5, no. 7, p. 7963, 2012.

[65] D. S. Parker, A. F. May, and D. J. Singh, "Benefits of Carrier-Pocket Anisotropy to Thermoelectric performance: The Case of p-type AgBiSe2," *Phys. Rev. Appl.*, vol. 3, no. 064003, 2015.

[66] J. Scheidemantel, C. Ambrosch-Draxl, T. Thonhauser, V. Badding, and O. Sofo, "Transport coefficients from first-principles calculations," *Phys. Rev. B - Condens. Matter Mater. Phys.*, 2003.

[67] G. K. H. Madsen and D. J. Singh, "BoltzTraP. A code for calculating band-structure dependent quantities," *Comput. Phys. Commun.*, vol. 175, no. 1, pp. 67–71, 2006.

[68] F. Giustino, M. Cohen, and S. Louie, "Electron-phonon interaction using Wannier functions," *Phys. Rev. B*, vol. 76, no. 16, pp. 1–19, 2007.

[69] S. Poncé, E. R. Margine, C. Verdi, and F. Giustino, "EPW: Electron–phonon coupling, transport and superconducting properties using maximally localized Wannier functions," *Comput. Phys. Commun.*, vol. 209, pp. 116–133, 2016.

[70] B. Liao, J. Zhou, B. Qiu, M. S. Dresselhaus, and G. Chen, "Ab initio study of electron-phonon interaction in phosphorene," *Phys. Rev. B*, vol. 91, no. 23, p. 235419, 2015.

[71] J. J. Zhou and M. Bernardi, "Ab initio electron mobility and polar phonon scattering in GaAs," *Phys. Rev. B*, vol. 94, no. 20, 2016.

[72] B. Qiu, Z. Tian, A. Vallabhaneni, B. Liao, J. M. Mendoza, O. D. Restrepo, X. Ruan, and G. Chen, "First-principles simulation of electron mean-free-path spectra and thermoelectric properties in silicon," *Eur. Phys. Lett.*, vol. 109, no. 5, p. 57006, 2015.

[73] J. S. Blakemore, "Approximations for Fermi-Dirac integrals, especially the function F1 2(η) used to describe electron density in a semiconductor," *Solid State Electronics*, vol. 25, no. 11. pp. 1067–1076, 1982.

[74] R. P. Chasmar and R. Stratton, "The Thermoelectric Figure of Merit and its Relation to Thermoelectric Generators," *J. Electron. Control*, vol. 7, no. 1, pp. 52–72, 1959.

[75] R. W. McKinney, P. Gorai, V. Stevanović, and E. S. Toberer, "Search for new thermoelectric materials with low Lorenz number," *J. Mater. Chem. A*, vol. 5, no. 33, pp. 17302–17311, 2017.

[76] X. Zou, X. Chen, H. Huang, Y. Xu, and W. Duan, "Enhanced thermoelectric figure of merit in thin GaAs nanowires," *Nanoscale*, vol. 7, no. 19, pp. 8776–8781, 2015.

[77] P. Norouzzadeh and D. Vashaee, "Classification of Valleytronics in Thermoelectricity," *Sci. Rep.*, vol. 6, no. 22724, 2016.

[78] R. Radtke, W. Bies, E. Runge, and H. Ehrenreich, "Thermoelectric properties of anisotropic semiconductors," *Phys. Rev. B*, vol. 65, no. 8, p. 085208, 2002.

[79] X. Wang, E. Witkoske, J. Maassen, and M. Lundstrom, "LanTraP: A code for calculating thermoelectric transport properties with Landauer formalism," *arxiv: 1806.08888v1*, 2018.

[80] M. V. Fischetti, "Monte Carlo Simulation of Transport in Technologically Significant Semiconductors of the Diamond and Zinc-Blende Structures - Part I: Homogeneous Transport," *IEEE Trans. Electron Devices*, vol. 38, no. 3, pp. 634–649, 1991.

[81] M. Lundstrom, *Fundamentals of Carrier Transport*. 2000.

[82] A. A. Mostofi, J. R. Yates, G. Pizzi, Y.-S. Lee, I. Souza, D. Vanderbilt, and N. Marzari, "An updated version of wannier90: A tool for obtaining maximally-localised Wannier functions," *Comput. Phys. Commun.*, vol. 185, no. 8, pp. 2309–2310, 2014.

[83] C. Jacoboni, C. Canali, G. Ottaviani, and A. Alberigi Quaranta, "A review of some charge transport properties of silicon," *Solid. State. Electron.*, vol. 20, no. 2, pp. 77–89, 1977.

[84] N. A. Mecholsky, L. Resca, I. L. Pegg, and M. Fornari, "Theory of band warping and its effects on thermoelectronic transport properties," *Phys. Rev. B*, vol. 89, no. 15, p. 155131, Apr. 2014.

[85] Z. M. Gibbs, F. Ricci, G. Li, H. Zhu, K. Persson, G. Ceder, G. Hautier, A. Jain, and G. J. Snyder, "Effective mass and Fermi surface complexity factor from ab initio band structure calculations," *npj Comput. Mater.*, vol. 3, no. 1, p. 8, 2017.

[86] S. M. Sze and K. K. Ng, *Physics of Semiconductor Devices (Sze - 2nd edition)*. 1981.

[87] G. K. H. Madsen, "Automated search for new thermoelectric materials: The case of LiZnSb," *J. Am. Chem. Soc.*, vol. 128, no. 37, pp. 12140–12146, 2006.

[88] S. Wang, Z. Wang, W. Setyawan, N. Mingo, and S. Curtarolo, "Assessing the Thermoelectric Properties of Sintered Compounds via High-Throughput Ab-Initio Calculations," *Phys. Rev. X*, vol. 1, no. 2, pp. 1–8, 2011.

[89] S. Curtarolo, G. L. W. Hart, M. B. Nardelli, N. Mingo, S. Sanvito, and O. Levy, "The high-throughput highway to computational materials design," *Nat. Mater.*, vol. 12, no. 3, pp. 191–201, 2013.

[90] P. Gorai, P. Parilla, E. S. Toberer, and V. Stevanović, "Computational Exploration of the Binary $A_1 B_1$ Chemical Space for Thermoelectric Performance," *Chem. Mater.*, vol. 27, no. 18, pp. 6213–6221, 2015.

[91] J. Yan, P. Gorai, B. Ortiz, S. Miller, S. A. Barnett, T. Mason, V. Stevanović, and E. S. Toberer, "Material descriptors for predicting thermoelectric performance," *Energy Environ. Sci.*, vol. 8, no. 3, pp. 983–994, 2015.

[92] H. Zhu, G. Hautier, U. Aydemir, Z. M. Gibbs, G. Li, S. Bajaj, J.-H. Pöhls, D. Broberg, W. Chen, A. Jain, M. A. White, M. Asta, G. J. Snyder, K. Persson, and G. Ceder, "Computational and experimental investigation of $TmAgTe_2$ and XYZ_2 compounds, a new group of thermoelectric materials identified by first-principles high-throughput screening," *J. Mater. Chem. C*, vol. 3, no. 40, pp. 10554–10565, 2015.

[93] G. D. Mahan and J. Sofo, "The best thermoelectric," vol. 93, no. July 1996, pp. 7436–7439, 2008.

[94] Z. H. Ge, L. D. Zhao, D. Wu, X. Liu, B. P. Zhang, J. F. Li, and J. He, "Low-cost, abundant binary sulfides as promising thermoelectric materials," *Mater. Today*, vol. 19, no. 4, pp. 227–239, 2016.

[95] G. D. Mahan, "Figure of merit for thermoelectrics," *J. Appl. Phys.*, vol. 65, no. 4, pp. 1578–1583, 1989.

[96] S. Kim, K. Ahn, D. H. Yeon, S. Hwang, H. S. Kim, S. M. Lee, and K. H. Lee, "Enhancement of seebeck coefficient in $Bi_{0.5}Sb_{1.5}Te_3$ with high-density tellurium nanoinclusions," *Appl. Phys. Express*, vol. 4, no. 9, p. 091801, 2011.

[97] J. M. O. Zide, D. Vashaee, Z. X. Bian, G. Zeng, J. E. Bowers, A. Shakouri, and A. C. Gossard, "Demonstration of electron filtering to increase the Seebeck coefficient in $In_{0.53}Ga_{0.47}As/In_{0.53}Ga_{0.28}Al_{0.19}As$ superlattices," *Phys. Rev. B*, vol. 74, no. 20, p. 205335, 2006.

[98] Q. Zhang, B. Liao, Y. Lan, K. Lukas, W. Liu, K. Esfarjani, C. Opeil, D. Broido, G. Chen, and Z. Ren, "High thermoelectric performance by resonant dopant indium in nanostructured SnTe," *Proc. Natl. Acad. Sci.*, vol. 110, no. 33, pp. 13261–13266, 2013.

[99] A. Casian, "Violation of the Wiedemann-Franz law in quasi-one-dimensional organic crystals," *Phys. Rev. B - Condens. Matter Mater. Phys.*, vol. 81, no. 15, 2010.

[100] R. Kim, S. Datta, and M. S. Lundstrom, "Influence of dimensionality on thermoelectric device performance," *J. Appl. Phys.*, vol. 105, no. 3, p. 034506, 2009.

[101] H. Usui and K. Kuroki, "Enhanced power factor and reduced Lorenz number in the Wiedemann-Franz law due to pudding mold type band structures," *J. Appl. Phys.*, vol. 121, no. 16, 2017.

[102] E. Witkoske, X. Wang, M. Lundstrom, V. Askarpour, and J. Maassen, "Thermoelectric band engineering: The role of carrier scattering," *J. Appl. Phys.*, vol. 122, no. 175102, 2017.

[103] X. Wang, V. Askarpour, J. Maassen, and M. Lundstrom, "On the calculation of Lorenz numbers for complex thermoelectric materials," *J. Appl. Phys.*, vol. 123, no. 5, p. 055104, 2018.

[104] P. Pichanusakorn and P. R. Bandaru, "The optimal Seebeck coefficient for obtaining the maximum power factor in thermoelectrics," *Appl. Phys. Lett.*, vol. 94, no. 22, pp. 2007–2010, 2009.

[105] C. Jeong, R. Kim, and M. S. Lundstrom, "On the best bandstructure for thermoelectric performance: A Landauer perspective," *J. Appl. Phys.*, vol. 111, no. 11, p. 113707, 2012.

[106] J. Zhou, R. Yang, G. Chen, and M. S. Dresselhaus, "Optimal bandwidth for high efficiency thermoelectrics," *Phys. Rev. Lett.*, vol. 107, no. 22, p. 226601, 2011.

[107] J. Maassen and M. Lundstrom, "A computational study of the thermoelectric performance of ultrathin Bi_2Te_3 films," *Appl. Phys. Lett.*, vol. 102, no. 9, pp. 1–5, 2013.

[108] G. J. Snyder, "Private Communication," 2018.

[109] G. D. Mahan and M. Bartkowiak, "Wiedemann-Franz law at boundaries," *Appl. Phys. Lett.*, vol. 74, no. 7, pp. 953–954, 1999.

[110] S. Yanagiya, N. V. Nong, M. Sonne, and N. Pryds, "Thermoelectric properties of SnO2-based ceramics doped with Nd, Hf or Bi," in *AIP Conference Proceedings*, 2012.

[111] J. Lan, Y. H. Lin, Y. Liu, S. Xu, and C. W. Nan, "High thermoelectric performance of nanostructured in2O3-based ceramics," in *Journal of the American Ceramic Society*, 2012.

[112] M. Lee, L. Viciu, L. Li, Y. Wang, M. L. Foo, S. Watauchi, R. A. Pascal Jr, R. J. Cava, and N. P. Ong, "Large enhancement of the thermopower in NaxCoO2 at high Na doping," *Nat. Mater.*, 2006.

[113] H. Ohta, K. Sugiura, and K. Koumoto, "Recent progress in oxide thermoelectric materials: P-type Ca 3Co4O9 and n-Type SrTiO3-," *Inorganic Chemistry*. 2008.

[114] Y. L. Pei, H. Wu, D. Wu, F. Zheng, and J. He, "High thermoelectric performance realized in a bicuseo system by improving carrier mobility through 3D modulation doping," *J. Am. Chem. Soc.*, vol. 136, no. 39, pp. 13902–13908, 2014.

[115] R. Funahashi, A. Kosuga, N. Miyasou, E. Takeuchi, S. Urata, K. Lee, H. Ohta, and K. Koumoto, "Thermoelectric properties of CaMnO3 system," in *International Conference on Thermoelectrics, ICT, Proceedings*, 2007.

[116] K. Koumoto, Y. Wang, R. Zhang, A. Kosuga, and R. Funahashi, "Oxide Thermoelectric Materials: A Nanostructuring Approach," *Annu. Rev. Mater. Res.*, vol. 40, no. 1, pp. 363–394, 2010.

[117] B. Kucukgok, B. Hussain, C. Zhou, I. T. Ferguson, and N. Lu, "Thermoelectric Properties of ZnO Thin Films Grown by Metal-Organic Chemical Vapor Deposition," *MRS Proc.*, 2015.

[118] A. N. Banerjee, R. Maity, P. K. Ghosh, and K. K. Chattopadhyay, "Thermoelectric properties and electrical characteristics of sputter-deposited p-CuAlO2thin films," *Thin Solid Films*, vol. 474, no. 1–2, pp. 261–266, 2005.

[119] D. J. Singh, "Band structure and thermopower of doped YCuO2," *Phys. Rev. B - Condens. Matter Mater. Phys.*, vol. 77, no. 20, pp. 1–5, 2008.

[120] J. Robertson, P. W. Peacock, M. D. Towler, and R. Needs, "Electronic structure of p-type conducting transparent oxides," *Thin Solid Films*, vol. 411, no. 1, pp. 96–100, 2002.

[121] V. Jayalakshmi, R. Murugan, and B. Palanivel, "Electronic and structural properties of $CuMO_2$ (M = Al, Ga, In)," *J. Alloys Compd.*, vol. 388, no. 1, pp. 19–22, 2005.

[122] P. Poopanya, "First-principles study of electronic structures and thermoelectric properties of 2H–CuAlO2," *Phys. Lett. A*, vol. 379, no. 9, pp. 853–856, 2015.

[123] D. J. Aston, D. J. Payne, A. J. H. Green, R. G. Egdell, D. S. L. Law, J. Guo, P. A. Glans, T. Learmonth, and K. E. Smith, "High-resolution x-ray spectroscopic study of the electronic structure of the prototypical p-type transparent conducting oxide $CuAlO_2$," *Phys. Rev. B*, vol. 72, no. 19, p. 195115, 2005.

[124] J. P. Perdew, K. Burke, and M. Ernzerhof, "Generalized gradient approximation made simple," *Phys. Rev. Lett.*, 1996.

[125] A. Buljan, P. Alemany, and E. Ruiz, "Electronic Structure and Bonding in CuMO2 (M = Al, Ga, Y) Delafossite-Type Oxides: An Ab Initio Study," *J. Phys. Chem. B*, vol. 103, no. 38, pp. 8060–8066, 1999.

[126] M. K. Y. Chan and G. Ceder, "Efficient band gap prediction for solids," *Phys. Rev. Lett.*, vol. 105, no. 19, pp. 5–8, 2010.

[127] F. Tran and P. Blaha, "Importance of the Kinetic Energy Density for Band Gap Calculations in Solids with Density Functional Theory," *J. Phys. Chem. A*, vol. 121, no. 17, pp. 3318–3325, 2017.

[128] J. P. Perdew and M. Levy, "Physical content of the exact kohn-sham orbital energies: Band gaps and derivative discontinuities," *Phys. Rev. Lett.*, vol. 51, no. 20, pp. 1884–1887, 1983.

[129] H. Yanagi, S. Inoue, K. Ueda, H. Kawazoe, H. Hosono, and N. Hamada, "Electronic Structure and Optoelectronic Properties of Transparent p-Type Conducting $CuAlO_2$," *J. Appl. Phys.*, vol. 88, no. 7, pp. 4159–4163, 2000.

[130] F. A. Benko and F. P. Koffyberg, "Opto-electronic properties of CuAlO2," *J. Phys. Chem. Solids*, vol. 45, no. 1, pp. 57–59, 1984.

[131] W. T. Liu, Y. Y. Luo, Z. T. Liu, and Z. M. Wei, "Density Functional Theory Study of P-Type Transparent Conducting 2H-CuAlO2 Oxide," *Appl. Mech. Mater.*, vol. 252, pp. 263–266, 2013.

[132] J. Pellicer-Porres, A. Segura, C. Ferrer-Roca, A. Polian, P. Munsch, and D. Kim, "XRD and XAS structural study of CuAlO2under high pressure," *J. Phys. Condens. Matter*, vol. 25, no. 11, 2013.

[133] P. Rodríguez-Hernández, A. Muñoz, J. Pellicer-Porres, D. Martínez-García, A. Segura, N. Garro, J. C. Chervin, and D. Kim, "Lattice dynamics of CuAlO2under high pressure from ab initio calculations," *Phys. Status Solidi Basic Res.*, vol. 244, no. 1, pp. 342–346, 2007.

[134] Z. Sui and I. P. Herman, "Effect of strain on phonons in Si, Ge, and Si/Ge heterostructures," *Phys. Rev. B*, vol. 48, no. 24, pp. 17938–17953, Dec. 1993.

[135] Z.-G. Chen, G. Han, L. Yang, L. Cheng, and J. Zou, "Nanostructured thermoelectric materials: Current research and future challenge," *Prog. Nat. Sci. Mater. Int.*, vol. 22, no. 6, pp. 535–549, 2012.

[136] B. J. Ingram, T. O. Mason, R. Asahi, K. T. Park, and A. J. Freeman, "Electronic structure and small polaron hole transport of copper aluminate," *Phys. Rev. B - Condens. Matter Mater. Phys.*, vol. 64, no. 15, pp. 1551141–1551147, 2001.

[137] S. Pantian, R. Sakdanuphab, and A. Sakulkalavek, "Enhancing the electrical conductivity and thermoelectric figure of merit of the p-type delafossite CuAlO2by Ag2O addition," *Curr. Appl. Phys.*, vol. 17, no. 10, pp. 1264–1270, 2017.

[138] G. Tan, S. Hao, J. Zhao, C. Wolverton, and M. G. Kanatzidis, "High Thermoelectric Performance in Electron-Doped AgBi3S5 with Ultralow Thermal Conductivity," *J. Am. Chem. Soc.*, vol. 139, no. 18, pp. 6467–6473, May 2017.

[139] B. R. Ortiz, P. Gorai, L. Krishna, R. Mow, A. Lopez, R. McKinney, V. Stevanović, and E. S. Toberer, "Potential for high thermoelectric performance in n-type Zintl compounds: a case study of Ba doped KAlSb4," *J. Mater. Chem. A*, vol. 5, no. 8, pp. 4036–4046, 2017.

[140] C. Fu, S. Bai, Y. Liu, Y. Tang, L. Chen, X. Zhao, and T. Zhu, "Realizing high figure of merit in heavy-band p-type half-Heusler thermoelectric materials," *Nat. Commun.*, vol. 6, no. 1, p. 8144, 2015.

[141] E. Witkoske, D. Guzman, Y. Feng, A. Strachan, M. Lundstrom, and N. Lu, "The use of strain to tailor electronic thermoelectric transport properties : A first principles study of 2H-phase CuAlO2," *J. Appl. Phys.*, vol. 125, no. 082531, 2019.

[142] Q.-J. Liu, Z.-T. Liu, Q.-Q. Gao, L.-P. Feng, H. Tian, F. Yan, and W. Zeng, "Density functional theory study of 3R– and 2H–CuAlO2 in tensile stress," *Phys. Lett. A*, vol. 375, no. 14, pp. 1608–1611, 2011.

[143] W. Liu, Z. Ren, and G. Chen, "Nanostructured Thermoelectric Materials BT - Thermoelectric Nanomaterials: Materials Design and Applications," K. Koumoto and T. Mori, Eds. Berlin, Heidelberg: Springer Berlin Heidelberg, 2013, pp. 255–285.

[144] Y. Feng, A. Elquist, Y. Zhang, K. Gao, I. Ferguson, A. Tzempelikos, and N. Lu, "Temperature dependent thermoelectric properties of cuprous delafossite oxides," *Compos. Part B Eng.*, vol. 156, pp. 108–112, 2019.

[145] O. J. Durá, R. Boada, A. Rivera-Calzada, C. León, E. Bauer, M. A. L. De La Torre, and J. Chaboy, "Transport, electronic, and structural properties of nanocrystalline CuAlO2delafossites," *Phys. Rev. B - Condens. Matter Mater. Phys.*, vol. 83, no. 4, pp. 1–10, 2011.

[146] L. Lindsay, "Isotope scattering and phonon thermal conductivity in light atom compounds: LiH and LiF," *Phys. Rev. B*, vol. 94, no. 17, p. 174304, Nov. 2016.

[147] G. P. Srivastava and V. Kresin, "The Physics of Phonons," *Phys. Today*, vol. 44, no. 12, pp. 75–76, Dec. 1991.

[148] T. Feng, L. Lindsay, and X. Ruan, "Four-phonon scattering significantly reduces intrinsic thermal conductivity of solids," *Phys. Rev. B*, vol. 96, no. 16, 2017.

[149] T. Feng and X. Ruan, "Four-phonon scattering reduces intrinsic thermal conductivity of graphene and the contributions from flexural phonons," *Phys. Rev. B*, vol. 97, no. 4, p. 45202, Jan. 2018.

[150] T. Feng and X. Ruan, "Quantum mechanical prediction of four-phonon scattering rates and reduced thermal conductivity of solids," *Phys. Rev. B*, vol. 93, no. 4, p. 45202, Jan. 2016.

[151] A. Ward, D. A. Broido, D. A. Stewart, and G. Deinzer, "Ab initio theory of the lattice thermal conductivity in diamond," *Phys. Rev. B*, vol. 80, no. 12, p. 125203, Sep. 2009.

[152] J. M. Ziman, "Electrons and phonons: the theory of transport phenomena in solids," *Endeavour*. 1960.

[153] T. Feng, B. Qiu, and X. Ruan, "Coupling between phonon-phonon and phonon-impurity scattering: A critical revisit of the spectral Matthiessen's rule," *Phys. Rev. B*, vol. 92, no. 23, p. 235206, Dec. 2015.

[154] M. T. Dylla, J. J. Kuo, I. Witting, and G. J. Snyder, "Grain Boundary Engineering Nanostructured SrTiO3 for Thermoelectric Applications," *Adv. Mater. Interfaces*, vol. 6, no. 15, p. 1900222, Aug. 2019.

[155] T. Hori, J. Shiomi, and C. Dames, "Effective phonon mean free path in polycrystalline nanostructures," *Appl. Phys. Lett.*, vol. 106, no. 17, p. 171901, Apr. 2015.

[156] M. Omini and A. Sparavigna, "Role of grain boundaries as phonon diffraction gratings in the theory of thermal conductivity," *Phys. Rev. B*, vol. 61, no. 10, pp. 6677–6688, Mar. 2000.

[157] R. Berman, E. L. Foster, J. M. Ziman, and F. E. Simon, "The thermal conductivity of dielectric crystals: the effect of isotopes," *Proc. R. Soc. London. Ser. A. Math. Phys. Sci.*, vol. 237, no. 1210, pp. 344–354, Nov. 1956.

[158] H. B. G. Casimir, "Note on the conduction of heat in crystals," *Physica*, vol. 5, no. 6, pp. 495–500, 1938.

[159] H.-S. Kim, S. D. Kang, Y. Tang, R. Hanus, and G. Jeffrey Snyder, "Dislocation strain as the mechanism of phonon scattering at grain boundaries," *Mater. Horizons*, vol. 3, no. 3, pp. 234–240, 2016.

[160] Z. Wang, J. E. Alaniz, W. Jang, J. E. Garay, and C. Dames, "Thermal Conductivity of Nanocrystalline Silicon: Importance of Grain Size and Frequency-Dependent Mean Free Paths," *Nano Lett.*, vol. 11, no. 6, pp. 2206–2213, Jun. 2011.

[161] P. Scherpelz, M. Govoni, I. Hamada, and G. Galli, "Implementation and Validation of Fully Relativistic GW Calculations: Spin–Orbit Coupling in Molecules, Nanocrystals, and Solids," *J. Chem. Theory Comput.*, vol. 12, no. 8, pp. 3523–3544, Aug. 2016.

[162] A. J. Cohen, P. Mori-Sánchez, and W. Yang, "Challenges for Density Functional Theory," *Chem. Rev.*, vol. 112, no. 1, pp. 289–320, Jan. 2012.

[163] J. Callaway, "Model for lattice Thermal Conductivity at Low Temperatures," *Phys. Rev.*, vol. 113, no. 4, pp. 1046–1051, 1959.

[164] B. Abeles, "Lattice thermal conductivity of disordered semiconductor alloys at high temperatures," *Phys. Rev.*, 1963.

[165] Z. Tong, S. Li, X. Ruan, and H. Bao, "Comprehensive first-principles analysis of phonon thermal conductivity and electron-phonon coupling in different metals," *Phys. Rev. B*, vol. 100, no. 14, p. 144306, Oct. 2019.

[166] Z. Tong and H. Bao, "Decompose the electron and phonon thermal transport of intermetallic compounds NiAl and Ni3Al by first-principles calculations," *Int. J. Heat Mass Transf.*, vol. 117, pp. 972–977, 2018.

[167] A. Sparavigna, "Influence of isotope scattering on the thermal conductivity of diamond," *Phys. Rev. B*, vol. 65, no. 6, p. 64305, Jan. 2002.

[168] L. Braginsky, N. Lukzen, V. Shklover, and H. Hofmann, "High-temperature phonon thermal conductivity of nanostructures," *Phys. Rev. B*, vol. 66, no. 13, p. 134203, Oct. 2002.

[169] J. A. Seijas-Bellido, R. Rurali, J. Íñiguez, L. Colombo, and C. Melis, "Strain engineering of ZnO thermal conductivity," *Phys. Rev. Mater.*, vol. 3, no. 6, p. 65401, Jun. 2019.

[170] E. W. Law, M. Kay, and R. A. Taylor, "Calculating the financial value of a concentrated solar thermal plant operated using direct normal irradiance forecasts," *Sol. Energy*, vol. 125, pp. 267–281, 2016.

[171] A. Krothapalli and B. Greska, "Concentrated solar thermal power," in *Handbook of Climate Change Mitigation and Adaptation, Second Edition*, 2016.

[172] K. McEnaney, D. Kraemer, Z. Ren, and G. Chen, "Modeling of concentrating solar thermoelectric generators," *J. Appl. Phys.*, vol. 110, no. 7, p. 74502, Oct. 2011.

[173] A. Date, A. Date, C. Dixon, and A. Akbarzadeh, "Theoretical and experimental study on heat pipe cooled thermoelectric generators with water heating using concentrated solar thermal energy," *Sol. Energy*, 2014.

[174] K. Yazawa and A. Shakouri, "System optimiztion of hot water concentrated solar thermoelectric generation," in *2010 3rd International Conference on Thermal Issues in Emerging Technologies, Theory and Applications - Proceedings, ThETA3 2010*, 2010.

[175] Y. Hama, W. J. Munro, and K. Nemoto, "Relaxation to Negative Temperatures in Double Domain Systems," *Phys. Rev. Lett.*, vol. 120, no. 6, 2018.

[176] V. L. Ginzburg, "On superconductivity and superfluidity (what I have and have not managed to do), as well as on the 'physical minimum' at the beginning of the 21st century," *ChemPhysChem*, vol. 5, no. 7. pp. 930–945, 2004.

[177] L. E. Bell, "Optimally Distributed Transport Properties Can Produce Highest Performance Thermoelectric Systems," *Phys. status solidi*, 2019.

[178] S. Datta, *Electronic Transport in Mesoscopic Systems, 5th print*. 2003.

VITA

Evan Witkoske received his BSc. in Physics, Mathematics, and Statistics from Purdue University, West Lafayette, IN, in 2011 and MSc. in Electrical Engineering from Purdue University in 2016. From 2013-2019 he has been pursuing his Ph.D. degree at Purdue University in the area of Microelectronics and Nanotechnology. His research interests include the theory, modeling, and simulation of energy and electron transport in materials and devices.